



NIKA2 research note

Draft

NIKA2 Commissioning Phase One Results

Prepared by the *NIKA2 Commissioning Tiger team*:
Laurence Perotto, Nicolas Ponthieu, Juan-F. Macías-Pérez, F.-Xavier Désert, Jean-François Lestrade,
Hervé Aussel, Frédéric Mayet and Florian Ruppin

NIKA2 collaboration
December 5, 2018

Contents

1	Total power Commissioning Introduction	1
2	Instrument, observations and methods	3
2.1	Overview of the NIKA2 instrument	3
2.2	Overview of the data reduction pipeline	7
2.3	Calibration and commissioning observations at the 30 m telescope	15
3	Opacity derivation	23
3.1	Taumeter-based method	23
3.2	Skydip-based method	25
3.3	Skydip selection	27
3.4	Skydip-based opacity measurements and tests	29
3.5	Corrected skydip method	31
3.6	Opacity monitoring	33
4	Focal Plane Reconstruction	34
4.1	Focal Plane Geometry	34
4.2	FOV grid distortion	35
4.3	Reconstruction of the focus surfaces	37
5	Beam pattern	42
5.1	Full beam pattern	42
5.2	Main beam	48
5.3	Beam efficiency	51
6	Calibration	55
6.1	Photometric System	55
6.2	Main photometric equation	55
6.3	Reference flux densities of the primary calibrators	57
6.4	Relative calibration, flat field	59
6.5	Telescope-driven beam variations	61
6.6	Baseline Calibration	66
6.7	Calibration using a photometric correction	68
6.8	Aperture Photometry Calibration	70

7 Photometry accuracy and stability assessments	77
7.1 Calibration validation criteria	77
7.2 Reference flux densities of the secondary calibrators	78
7.3 Baseline calibration results	79
7.4 Comparison with other calibration methods	82
8 Sensitivity	88
8.1 Estimating the time of integration	88
8.2 NEFD estimation methods	89
9 Performance of NIKA2 at the IRAM 30 m telescope	97
A APPENDIX	102
A.1 Synchronization with the telescope	102
A.2 Reference to technical documentation	102
A.3 Photometric system definitions	103
A.4 Focus surface stability checks	109
A.5 Calibration reference software	112

List of Figures

2.1	NIKA2 transmission	4
2.2	Atmosphere effect on system transmission	5
2.3	KID resonance circle	6
2.4	Example of Time-Ordered-Information	9
2.5	KID-to-KID correlation matrices	10
2.6	Noise RMS and power spectra	12
2.7	Distribution of the SNR per beam	14
2.8	Axial focus measure	16
2.9	Lateral X focus measures	18
2.10	Lateral Y focus measures	19
2.11	Summary plots of the reduction of pointing scan.	20
2.12	Pointing session results	20
2.13	skydip	21
3.1	IRAM taumeter to NIKA2 opacity model	24
3.2	26
3.3	N2R9 skydip scan selection.	27
3.4	28
3.5	Skydip selection impact on opacities	29
3.6	NIKA2 skydip-based vs taumeter opacities	30
3.7	NIKA2 skydip-based opacity stability against observing elevations	31
3.8	NIKA2 skydip-based opacity correcting relation	32
3.9	Zenith opacity monitoring during N2R9, N2R12 and N2R14	33
4.1	KID selection and stability of position in the FOV	36
4.2	Simulated FOV grid	38
4.3	Focus surfaces	39
5.1	Beam pattern.	43
5.2	Noticeable features of NIKA2 beam pattern.	44
5.3	Beam structure	45
5.4	Stability of the beam profile	47
5.5	Main Beam FWHM	49
5.6	Main Beam FWHM distributions	50
5.7	Main beam FWHM distribution across the array	52
6.1	Average main beam flat fields	62

6.2	Average forward efficiency flat fields	63
6.3	Dispersion of the flat field for nine <i>beammaps</i>	64
6.4	Beam size monitoring using OTF scans	64
6.5	Beam size monitoring using pointing scans	65
6.6	Beam size monitoring comparison	65
6.7	Uranus flux density stability against FWHM	73
6.8	Uranus flux density stability against atmospheric transmission	74
6.9	Uranus flux density stability against atmospheric transmission	75
6.10	Aperture photometry of Uranus	76
7.1	MWC349 spectral energy density	79
7.2	Baseline calibration bias	80
7.3	Baseline calibration rms error estimate	85
7.4	Calibration bias comparison	86
7.5	Comparison of calibration rms errors	87
8.1	Time of integration	90
8.2	NEFD vs time	92
8.3	Jackknife maps of G2 and HLS J0918+5142	93
8.4	NEFD per scan	94
8.5	Measured NEFD versus source flux for N2R9 at 1 and 2 mm	95
8.6	Measured NEFD versus observed opacity	95
A.1	Photometric correction pivot Gaussian size	107
A.2	Stability of the focus surface across the sequences	110
A.3	Stability of the focus surface across the sequences	111

List of Tables

1.1	Main characteristics defining the expected performances of NIKA2	1
1.2	Commissioning campaigns, dates and general comments	2
4.1	Number of detectors	35
4.2	Field-of-view deformations	37
5.1	Average 3-Gaussian beam profile parameters	46
5.2	51
5.3	Solid angle of true beam based on Uranus and Neptune observations	53
5.4	53
5.5	Main beam efficiency and level of error beam	54
6.1	NIKA2 reference frequencies and FWHM	55
6.2	Color correction factor for a target source $S \propto \nu^{\alpha_s}$	58
6.3	Primary calibrator flux models	58
6.4	NIKA2 Planet flux expectations	60
6.5	Flat field dispersions	61
6.6	Absolute calibration scan numbers	67
6.7	Comparison of calibration results using five methods	70
6.8	Solid angle of total beam based on Uranus and Neptune observations	71
6.9	ratio aperture photometry / fixed-width Gaussian flux densities	72
7.1	Reference flux densities of secondary calibrators	79
7.2	Baseline calibration results	81
7.3	Comparison of calibration results using five methods	82
8.1	Comparison of the NEFD estimates using three methods	96
8.2	NEFD estimates on all sub-Jy sources	96
9.1	Main performance measurements	100
9.2	Main performance requirement	101

Abstract

The commissioning in intensity of the NIKA2 camera operated at the IRAM 30 m telescope was completed in April 2017, the instrument delivery to IRAM was officialised at the 'End-of-commissioning' review that took place at the IRAM-Grenoble in September 2017, and scientific purpose operations began in October 2017. This document comes along with the instrument delivery and presents NIKA2 performance assessment in intensity, as defined in the MoU. The characterisation of the performance is based on several thousands of observation scans that were acquired at the February 2017 technical campaign, during which NIKA2 instrumental set-up was in the final configuration for the first time, and at the first science pools that took place in October 2017 and January 2018. This vast data set allows us to check the performance stability for one year and against a large range of observing elevations and atmospheric conditions. The calibration and performance assessment methods that we have developed are also thoroughly described, as well as the robustness tests that we have performed.

Chapter 1

Total power Commissioning Introduction

	Reference Wavelength [mm]	1.2	2.0
	Reference Frequency [GHz]	260	150
FOV diameter [arcmin]	5 (6.5)	5 (6.5)	
Pixel size in beam sampling unit [$F\lambda$]	0.9 (0.6)	0.9 (0.6)	
FWHM [arcsec]	12 (10)	18 (16)	
Fraction of valid detectors [%]	50 (90)	50 (90)	
NEFD ^a [$\text{mJy} \cdot \text{s}^{1/2} / \text{beam}$]	30 (15)	20 (10)	
NEFD [$\text{mJy} \cdot \text{s}^{1/2} / \text{beam}$] goal on 90% of the pixels	15	10	
NEFD [$\text{mJy} \cdot \text{s}^{1/2} / \text{beam}$] specification on 50% of the pixels	30	20	

^(a) NEFD in typical IRAM good sky opacity condition: 2 mm pwv, 60° elevation

Table 1.1: Each parameter is associated with two values: the first one indicates the *specifications*, i.e. the requirements to be met by the instrument, while the second bracketed one gives the *goals*, i.e. the values targeted by the collaboration.

This document describes the work accomplished by the NIKA2 consortium in order to validate the performances of NIKA2. More specifically, the MoU defined specifications and goals on some key parameters. They are summarized in Tab 1.1. Additional information on the instrument and ancillary parameters were also requested by IRAM, together with a document demonstrating how the performances have been assessed, both in terms of observations and data reduction. This document is the answer.

Table 1.2 summarizes the timeline of NIKA2 integration and tests since the replacement of NIKA1 by NIKA2 in Oct. 2015. Based on this overview and the observing conditions, we have focused our analysis on data from the N2R9 calibration campaign and the N2R12 and N2R14 science pools. The final results of this commissioning are given in the last section essentially via a summary table 9.1 with links to the relevant sections for detailed demonstration of the results.

In order to be self-consistent, the document is also meant to be read in chronological order. Chapter 2 summarizes the main features of the instrument and of the data reduction that

RUN	NIKA Run	Starting date	End date	General comments
N2R1	13	29-October-2015	10-November-2015	Not full instrumentation
N2R2	14	24-November-2015	02-December-2015	13 NIKEL boards working
N2R3	15	12-January-2016	01-February-2016	20 NIKEL boards
N2R4	16	1-March-2016	15-March-2016	
Dark run	17	4-May-2016	4-May-2016	Dark tests with N2R4 conditions
N2R5	18	16-September-2016	11-October-2016	New dichroic, corrugated lenses, new array 2 mm, new electronics
N2R6	19	25-October-2016	1-November-2016	
N2R7	20	6-December-2016	13-December-2016	Test external calibrator
N2R8	21	9-January-2017	13-January-2017	Replace array 1 lens by smooth one, adjust the alignment of internal optics
		24-January-2017	25-January-2017	Tests on the sky
N2R9	22	21-February-2017	28-February-2017	
N2R10	23	18-April-2017	25-April-2017	End of commissioning phase 1, Science verification
N2R11	24	8-June-2017	13-June-2017	polarization commissioning

Table 1.2: Brief summary of the NIKA2 commissioning campaigns indicating the starting and end dates as well as some general comments.

will be used in the remaining of the document for all performance derivations. It also lists and introduces the necessary inputs that are required for the full data reduction and that are discussed in details in the following sections. We start with atmospheric opacity in chapter 3, then proceed to detector positional offsets in chapter 4 and beam characterization in chapter 5. Chapter 6 addresses the overall calibration of observations. At last, chapters 7 and 8 address the final performances of the instrument in terms of photometry and sensitivity, before the final summary section 9.

Chapter 2

Instrument, observations and methods

This chapter is meant to be an introduction to the instrument and the data reduction from an astronomer point of view. It summarizes the instrument parameters that are relevant for the data processing and the different steps required to go from raw data to scientific maps. The details of each of these parameters and their derivation is the object of the following sections.

2.1 Overview of the NIKA2 instrument

NIKA2 is a millimeter camera able to simultaneously image a field-of-view of 6.5 arcmin in diameter at 150 and 260 GHz, with polarimetric capabilities at 260 GHz. The optics of the telescope receiver cabin have been modified in order to increase the telescope field-of-view compared to earlier IRAM instruments. To achieve these goals without degrading the telescope angular resolution, it employs a total of around 2,900 detectors split over three distinct arrays of Kinetic Inductance Detectors (KID). A KID is a planar superconducting resonator properly designed to absorb the incoming radiation and at the same time incarnate the multiplexing scheme. The quality factors of the KID used in NIKA2 are of the order of 15,000 **TODO: define the 'quality factor'**. The measurable quantity, proportional to the incoming power per pixel, is the shift in frequency of each resonance (pixel). This shift is a consequence of variations of the resonator (kinetic) inductance with incoming radiation.

2.1.1 Optics

The NIKA2 camera optics include two cold mirrors, and the filtering of unwanted (off-band) radiation is provided by a suitable stack of multi-mesh filters placed at all temperature stages between 150 mK and room temperature. An air-gap dichroic splits the 150 GHz (reflection) from the 260 GHz (transmission) beams. A grid polariser ensures then the separation of the two linear polarizations on the 260 GHz channel (V and H). Band-defining filters, custom-designed to optimally match the atmospheric windows, are installed in front of each array. A half-wave polarization modulator is added at room temperature when operating the instrument in polarimetric mode.

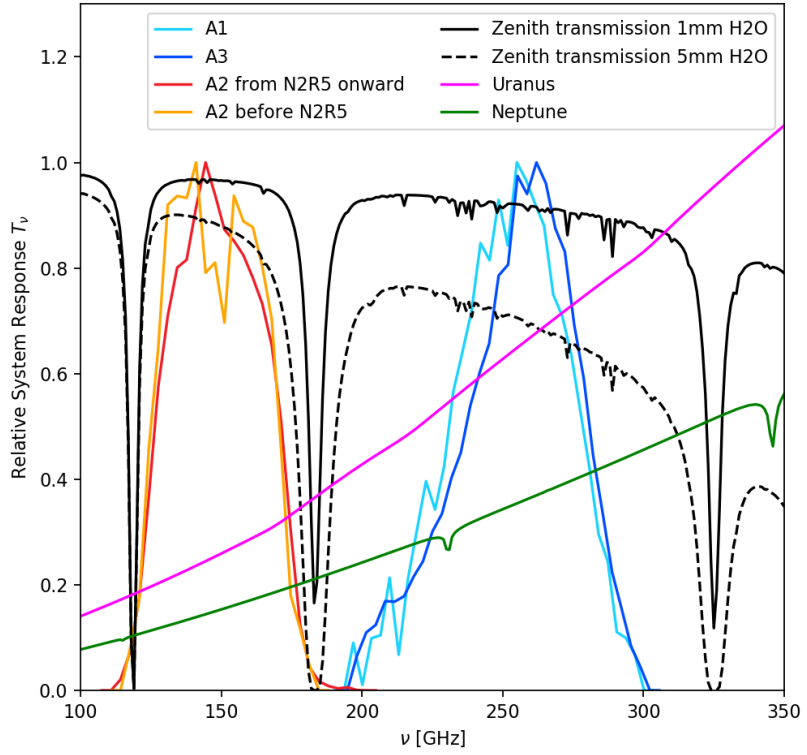


Figure 2.1: Relative system response of the three NIKA2 arrays as a function of frequency. For illustration we also plot atmospheric transmission obtained with the ATM model [2] for different values of precipitable water vapor. The spectra of ESA4 model of Uranus and ESA5 model of Neptune [13] in the frequency range are overplotted with arbitrary normalization.

2.1.2 Bandpasses

The NIKA2 spectral bands were measured in the laboratory using a Martin-Puplett interferometer built in-house [17]. Both arrays and filter bands were considered in the measurements. These were obtained from the difference of two black bodies, hence they include a ν^2 Rayleigh-Jeans (RJ) spectral term. Figure 2.1 shows the relative spectral response for the three arrays (corrected of the RJ term). Notice that array A2 was replaced by a new one in N2R5 and that the spectral transmissions are not the same (red and orange lines in the figure).

The two arrays operating at 260 GHz, mapping different polarisations, exhibit a slightly different spectral behaviour as can be seen on figure 2.1. This may be explained by a tiny difference in the silicon wafer and/or Aluminium film thicknesses. For instance, the observed shift of the peak frequency, 265 GHz for the V (A1) array versus 258 GHz for the H one (A3), can be explained by about 5 microns change in the substrate thickness.

It is clear from figure 2.1 that the atmosphere will modify the overall transmission of the system, especially at the edges of the A2 array. For each array, we define reference frequencies that are chosen as round numbers in the middle of the bands to define NIKA2 photometric system as will be discussed in Sect. 6.1. These are 260 GHz for the A1 and A3 and 150 GHz for the A2 array.

Given an array, an atmosphere, an elevation and a source, we can define an effective fre-

quency such that:

$$\nu_{\text{eff}}(\sec \delta, mm_{H_2O}) = \frac{\int_0^{+\infty} S_\nu T_\nu(\sec \delta, mm_{H_2O}) \nu d\nu}{\int_0^{+\infty} S_\nu T_\nu d\nu} \quad (2.1)$$

Where S_ν is the source spectrum, T_ν is the system transmission without atmosphere, and $T_\nu(\sec \delta, mm_{H_2O})$ is the system transmission including the atmosphere.

Similarly, we can define a bandwidth for each array, as a function of the elevation and atmosphere water content.

$$\Delta\nu(\sec \delta, mm_{H_2O}) = \int_0^{+\infty} \frac{T_\nu(\sec \delta, mm_{H_2O})}{\text{Max}(T_\nu(\sec \delta, mm_{H_2O}))} d\nu \quad (2.2)$$

Figure 2.2 shows the variation of ν_{eff} with respect to the reference frequency for NIKA2 primary calibrator Neptune and $\Delta\nu$ for the three arrays. For the atmosphere, we used GILDAS ATM 2009 model [2], computed for the IRAM 30-m telescope, with so called *midlatwinter* conditions. We select in the model grid an atmosphere with $T = 268.3$ K and a pressure of 703.5 hPa. The atmosphere introduces variations of the effective frequency at the few percent level, and large bandwidth variations for Array 2. This is the reason why great care should be put in correcting for atmospheric effect that will be addressed in Chapter 3.

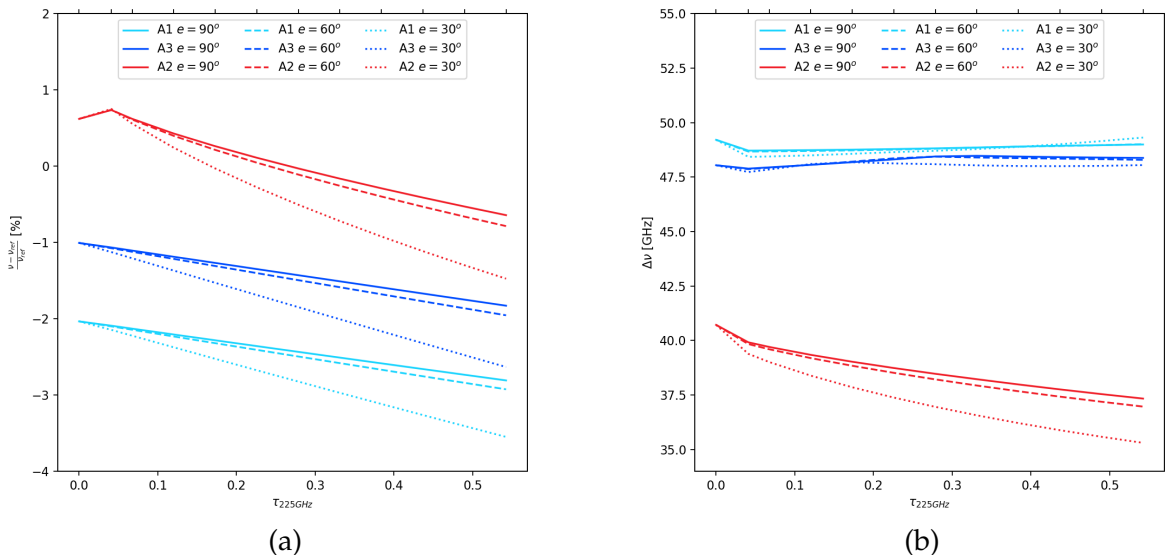


Figure 2.2: Variations of the (a) effective frequency of each bandpass for Neptune and (b) bandwidth as a function of the atmosphere opacity for different elevations e .

2.1.3 Cryogenics

The optimal operation of the detectors is achieved at a temperature of around 150 mK, well below the Aluminium superconducting transition. For this reason, NIKA2 employs a custom dilution fridge to cool down the focal plane, and the refractive portion of the optics, for a total mass around 100 kg, deeply in the sub-Kelvin regime. Despite the complexity and size of the system, the operation of NIKA2 does not require external cryogenic liquids and is fully remotely controllable.

2.1.4 KIDs and electronics

The 150 GHz channel is equipped with an array of 616 pixels, arranged to cover a 78 mm diameter circle. Each pixel has a size of $2.8 \times 2.8 \text{ mm}^2$. The array is connected over four different readout lines. In the case of the 260 GHz band detectors, the pixel size is $2 \times 2 \text{ mm}^2$, to ensure a comparable sampling of the focal plane. In order to fill the two 260 GHz arrays, a total of 1,140 pixels are needed in each of them. The focal planes are all based on thin Aluminium films deposited by e-beam evaporation under ultra-high vacuum conditions over a Silicon substrate.

The key advantage of the KID technology is the simplicity of the cold electronics and the multiplexing scheme. In NIKA2, each block of around 150 detectors is connected to single coaxial line providing the excitation and the readout at the two ends. Each of the readout lines is linked to the input of a cryogenic (4 K) low-noise amplifier. The warm electronics required to digitize and process the pixels signals is composed of twenty custom readout cards (one per feed-line).

In this document, the 2 mm array is called A2, while the two 1 mm arrays are called A1 and A3.

2.1.5 KID photometry and tuning

Kinetic Inductance Detectors are superconducting resonators whose resonance frequency shifts linearly depending on the incoming optical power. The measure of such frequency shift Δf is what allows us to use KID as mm-wave detectors.

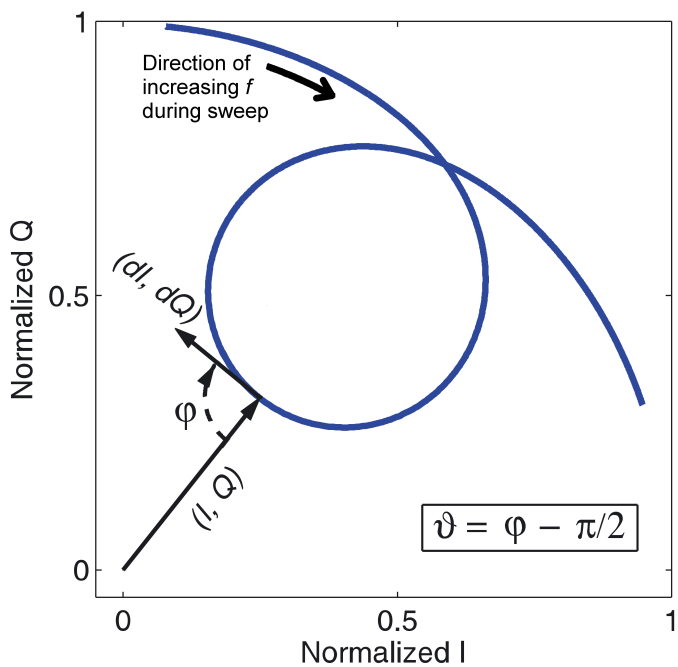


Figure 2.3: Sample resonance circle in the IQ plane. Both the tuning procedures are based on the measurement of the angle ϑ between the two vectors (I, Q) and (dI, dQ)

For the KID readout, an excitation signal is sent into the cryostat on the feedline coupled to the KID. The transmitted signal can be described by its amplitude and phase, or, as is common practice for KID, by its components that are In-phase (I) and in Quadrature Q with respect to the excitation signal. When a frequency sweep is carried around a KID resonance, the transmitted signal makes a sort of circle in the $I - Q$ plane, as shown in Fig. 2.3. The goal is now to relate the variations ($\Delta I, \Delta Q$) along this circle induced by incident light to the Δf . For this, the electronics modulates the excitation frequency at about 1 kHz with a known δf frequency variation and the read out gives the induced (dI, dQ). Projecting linearly ($\Delta I, \Delta Q$) on (dI, dQ) therefore provides Δf . This value, in Hz, is the raw input timeline to the pipeline and will be further calibrated into astronomical units (sect. 6). For historical reasons, this way of deriving KID signals has been nicknamed *RfdIdQ*. More details on this process are given in [21].

Not only incident astronomical light reaches the KIDs and contributes to Cooper pair breaking. Any change in the background optical load (due, for example, to changes in the atmospheric transmission or in the elevation) contributes as well to the shift of the resonances. In order to maximize the sensitivity of a KID, the excitation signal used to read it out must always be near its resonance frequency. We therefore have developed a tuning algorithm that takes care of this optimization. Tunings are performed during the first subscan of each observation in order to be optimally tuned at the same elevation and sky conditions as the source. It takes only a few seconds when the f_{tones} are close to the current functioning point. In order to always be in these conditions, continuous tunings are done between two scans when NIKA2 is not observing.

A specific case is when we do *skydips*. In this case, we tune all the KIDS at the beginning of each subscan/elevation step on purpose to monitor the induced variation of f_{tone} by the sky load.

2.2 Overview of the data reduction pipeline

Because each matrix of NIKA2 is a filled array with more than one detector per PSF on average, and because the atmosphere and electronic noise act as correlated low frequency parasites, the data reduction of NIKA2 does not proceed on an individual KID basis in general. This, in addition to the necessary pointing information specifies some of the data reduction process. In short, the data reduction proceeds as such:

- Low level processing (Sect. 2.2.1)
- Pointing reconstruction (Sect. 2.2.2)
- TOI calibration and opacity correction (Sect. 2.2.3)
- TOI processing (Sect. 2.2.4)
- Map projection (Sect. 2.2.5)
- Photometry (Sect. 2.2.6)

2.2.1 Low level processing

A first step of the analysis is to read the data produced by NIKA2's acquisition. The data as such comprise various quantities that describe the variations of the KID's resonance frequencies,

such as I , Q , dI , dQ . From these quantities, and throughout this work, we use our so called $RfdIdQ$ photometric estimator that combines them into a quantity that is proportionnal to the flux absorbed by a KID [21] and homogeneous to Hz.

In addition to this, we look for and remove the - rare - cosmic rays events. KIDs have such fast time constants that unlike bolometers, these events affect a sole sample that is easy to detect by a simple comparison to the rms of the TOI a few second window. These affected samples are remplaced by a simple linear interpolation of their surrounding (not to leave holes in the TOI) but are flagged in order not to project false data on the final map.

We also have a series of tests that read flags from the acquisition overall. These flags monitor potential jumps in the cryostat or acquisition monitoring. Most important are the flags related to the tuning. Because the acquisition file boundaries are not strictly linked to the beginning and the end of a scan, we must discard everything that happens before the last tuning of the beginning, and everything after the first automatic tuning that happens when the scan is done.

Because the tuning of KIDs might fail from time to time depending on the weather conditions for instance, we systematically check each KID and see if its noise is far from the average noise of all other KIDs in the same array, with a typical 3σ threshold. This criterion may seem a bit tight, but in any case, KIDs are inverse noise variance weighted in the final map projection, so they would be given relatively low weight anyway (see Sect. 2.2.5).

At this stage of the processing, we have isolated the relevant fraction of the data for scientific processing and flagged out potentially misbehaving KIDs or timeline accidents (glitches).

2.2.2 Pointing reconstruction

This step consists in addressing each sample of each KID to the correct sky coordinates and their associated map pixel. The pointing data are passed to the NIKA2 raw data via ELVIN **XXX TBC XXX**. They describe the absolute pointing of a reference point in the focal plane in various quantities, the absolute azimuth and elevation (α, δ) of the source, together with offsets $(\Delta\alpha_t, \Delta\delta_t)$ w. r. t. these. Because our final maps will be centered on a fixed position (typically the center of the source that is aimed by the focal plane reference position), we are especially interested in pointing offsets w. r. t. this position. We therefore detail here the derivation of these offsets.

We store KID pointing offsets w. r. t. the reference position in Nasmyth (x, y) coordinates (independent of time) once and for all in our KID database (a. k. a. *kidpar*). Sect. 4 details how these offsets are derived. To go from Nasmyth offsets to (α, δ) offsets, we apply the following rotation by the elevation angle:

$$\begin{aligned}\Delta\alpha_t^k &= \cos\delta_t\Delta x^k + \sin\delta_t\Delta y^k, \\ \Delta\delta_t^k &= -\sin\delta_t\Delta x^k + \cos\delta_t\Delta y^k,\end{aligned}$$

where k is a KID index. Adding these offsets to the reference $(\Delta\alpha_t, \Delta\delta_t)$ gives the absolute pointing of each KID in these coordinates. An extra rotation by the parallactic angle η_t is required to obtain KID's coordinates in *R. A., Dec* coordinates:

$$\Delta R. A.^k_t = \cos\eta_t\Delta\alpha_t^k + \sin\eta_t\Delta\delta_t^k, \quad (2.3)$$

$$\Delta Dec^k_t = -\sin\eta_t\Delta\alpha_t^k + \cos\eta_t\Delta\delta_t^k. \quad (2.4)$$

We now have the pointing of each KID at each time relative to the source that we usually center on our final map. It then trivial to assign the map pixel corresponding to this pointing on a Nearest Grid Point basis.

This pointing reconstruction is done early in the data reduction process because we'll need to know when a KID is close or far from the source for the timeline processing (Sect. 2.2.4).

2.2.3 TOI calibration

We now focus on the absolute calibration of each TOI. As stated in Sect. 2.2.1, at this stage of the reduction each KID $RfdIdQ$ timeline is in Hz. The conversion process to go from these Hz into Jy/beam proceeds in two steps: a standard absolute calibration and a correction for the current opacity and elevation.

The standard conversion from Hz to Jy/beam is stored in the *kidpar* database. The derivation of these gains $g(k)$ is detailed in Sect. 4. Suffice is to say here that simply multiplying the TOI's by these gains converts them into Jy/beam. Of course, this individual absolute calibration also acts as a relative calibration. This calibration is meant to work at zero opacity and 90° elevation. We thus need to correct for the current opacity τ and elevation. In short, the absolute calibration reads

$$TOI^k(t)[\text{Jy}/\text{beam}] = RfdIdQ^k(t)[\text{Hz}] \times g(k) \times e^{\tau_t / \sin \delta_t} \quad (2.5)$$

The derivation of opacity is presented in Sect. 3.

2.2.4 TOI processing

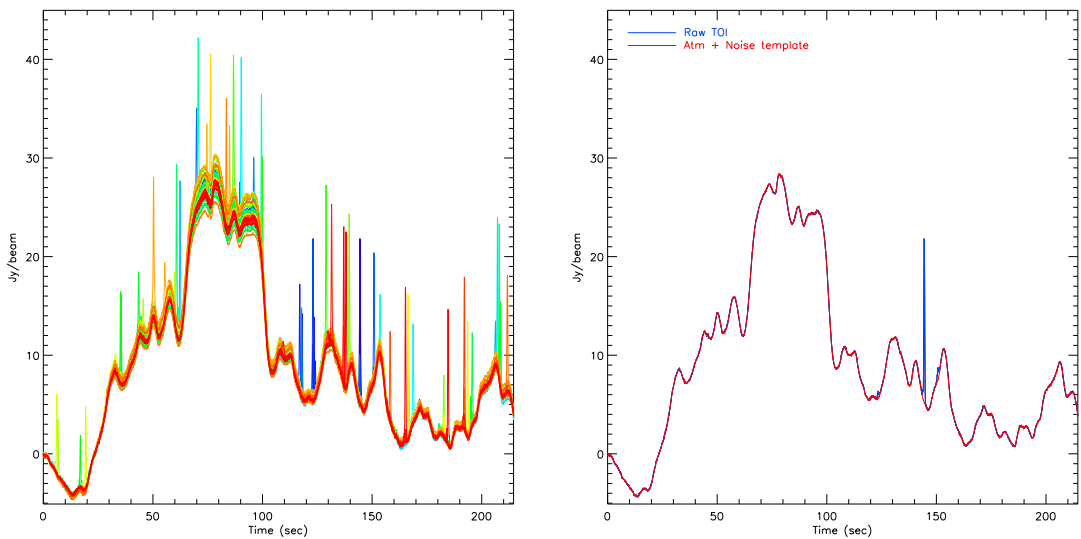


Figure 2.4: *Left:* Example of 40 KID raw timelines during an observation of Uranus. The low frequency correlated component (atmosphere and electronic noise) is clearly seen. *Right:* One of these TOIs and the scaled *common mode* that is subtracted from it.

Draft

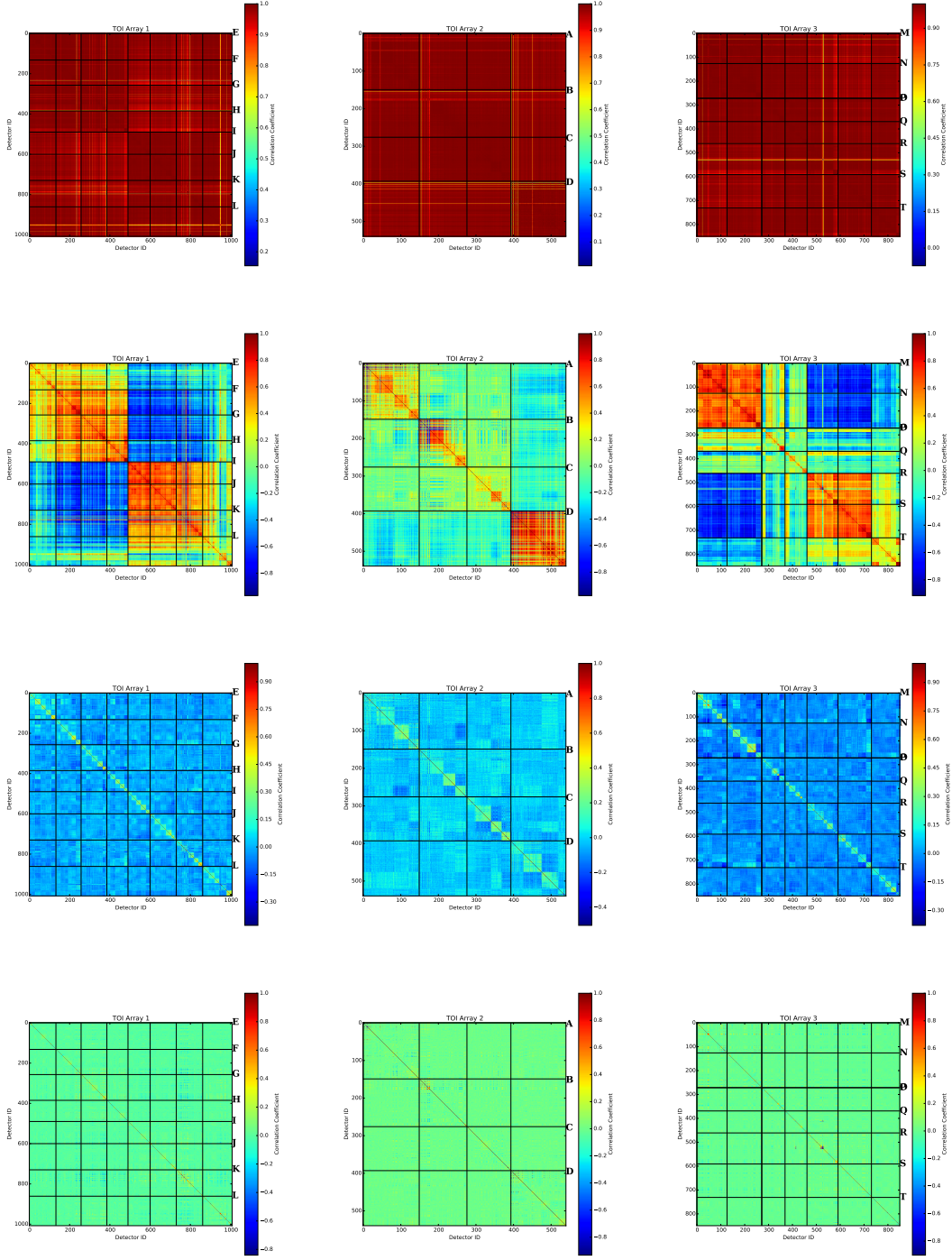


Figure 2.5: From left to right: TOI correlation matrices for the three NIKA2 arrays (A1, A2, and A3) for scan 20170228s150. From top to bottom we present the correlation of the raw data, after CM, PCA and MCP decorrelation methods.

As presented on Fig. 2.4, the atmosphere and the electronic noise combine into a large low frequency component that we want to eliminate as much as possible. Most of the atmospheric component is common to all KIDs, which is expected because the telescope is a 30 m dish and therefore has a **Carsten comments: XXXX near field of XXXXX m – > effective collecting area of 170 m² at 1.2 mm ?**

On Fig. 2.4, the planet is visible in the TOIs and serves as guide to both the noise relative amplitude and the discussion about TOI processing in the following. On Fig. 2.5, we take a scan on Pluto where the signal is negligible compared to noise on the timescale of a scan to focus on the noise properties. We present the KID to KID timeline correlation matrices for the three arrays, either before any data reduction or with different estimates of the low frequency component:

- **Common mode decorrelation (CM).** We use all detectors of the same array to build an average low frequency component nicknamed *common mode*. This mode is then linearly regressed and subtracted from each KID timeline. In this method, the *common mode* at time t is the median of all KIDs at this time t .
- **Principal Component Analysis (PCA).** For each NIKA2 array independently we decompose the covariance matrix in principal components. From those we derive up to 10 independent templates corresponding to the largest eigenvalues **that we subtract from the TOIs XXX TBC XXXX.**
- **Most correlated pixels (*common mode one block*).** For each detector in a given array we identify the detectors that are most correlated to it (a minimum of 15). Using those detectors we compute a common mode like in method CM but with more refinements to be valid even on bright sources (see below).

As expected the raw data noise correlation is dominated by atmospheric noise and we observe full correlation between detectors but for badly behaving detectors which are removed from the analysis. Significant residual correlation and anti-correlation is observed after CM decorrelation. This is both due to spatial changes in the atmospheric emission (overall residuals) and to instrumental and electronic noise characteristics (correlation blocks that can be associated to electronic boxes). The PCA decorrelation leads to approximately block-diagonal correlation matrices. These observed blocks in the correlation matrix can be associated to first order to the different sub-bands in each of the electronic boxes. In the case of the MCP decorrelation, for which only those pixels highly correlated to the pixel of interest are used, we observe that the correlation matrix is more diagonal as in the two other derivations of the common mode.

In Fig. 2.6 we present the rms noise per kid and the power spectra of a typical raw data-stream, and the CM, PCA and MCP decorrelated data. We observe that after decorrelation we reduce significantly the rms of the noise. Equivalently, in $1/f$ -like noise in the power spectra (principally due to atmospheric emission) is significantly reduced leading to nearly flat spectra down to 0.05 Hz, with larger $1/f$ -like residual noise for the CM decorrelation method at lower frequencies. This is translated into a larger rms noise for this method with respect to the others. For the three arrays we find increasing noise with increasing resonant frequency within each electronic box. This is probably related to the difference of gains between subbands in the read-out electronics. We also find for the three arrays some noise bursts that are not fully consistent from one decorrelation method to another.

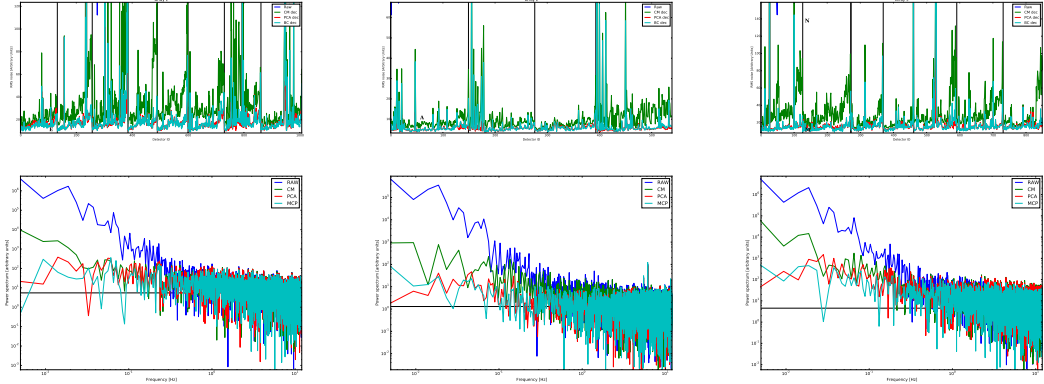


Figure 2.6: From top to bottom and from left to right, we show the data rms and power spectra for the three NIKA2 arrays (A1, A2, and A3) for scan 20170228s150. The rms and power spectra are given for the raw data (blue), and for the CM (green), PCA (red) and MCP (cyan) decorrelated data. The vertical lines in the rms noise figures separate detectors from different readout electronic boxes. Within each electronic box the pixels are ordered with increasing resonant frequency across the electronic band.

We have investigated several ways of using this information to remove this component from the TOIs. Our preferred choice so far, that is the reference method for this document, is the *common mode one block* method, that we describe into further details below:

- From the pointing information (Sect. 2.2.2), we derive a mask per TOI and for each time t that is 0 if the KID is closer to the source than 60 arcsec, 1 otherwise.
- Only samples for which two KIDs are further than 60 arcsec from the source are selected and the KID-to-KID correlation is computed.
- For a KID k_0 , we store the KID identifiers that are most correlated to it. We first select the 15 most correlated KIDs, then the average and the dispersion σ of these correlations are computed. **Then we add to the selection all the KIDs that are as correlated to k_0 as the 15 first, up to 2σ .**
- A median common mode (far from the source) for this block of 15 or more KIDs is derived.
- A cross-calibration to each of these KIDs is computed using the median common mode. Then an inverse noise weighted average mode is build. At each time, we use only KIDs that are further from the source than 60 arcsec. At this stage it is important to verify to have enough KIDs to produce a continuous mode and to do not leave samples without any estimation.
- We linearly regress this average mode against k_0 's TOI (far from the source) and subtract on the entire k_0 timeline.

This process is repeated for each KID. Fig. 2.4 shows an example of this low frequency mode derivation, together with the resulting TOI cross-correlation matrix after its subtraction. We have tested on simulations that this method does not alter the flux of the source. **Alessia's comment: Do we have a plot to show this ?**

If the observed field contains something else than a single point source at its center, then several options are available to generalize this method. In particular, the mask can be designed to adjust to several point sources. If the source is diffuse and extended, then we may go through an iterative procedure that subtracts an improved derivation of the signal at each step. For this work about the commissioning of the instrument and the assessment of its performances on point sources, we do not need to go into further details about this.

2.2.5 Map projection

At this stage, data have been calibrated and cleaned and we have the pointing information for each sample. If the noise was white and uncorrelated from KID to KID, we would be able to produce an optimal map S_p using an inverse variance noise weighting of all of the measurements m_t^k that fall into a map pixel p with a simple Nearest Grid Point procedure. In this scheme, data samples are coadded with inverse variance noise weighting: for each KID, we compute the standard deviation σ_k of its TOI far from the source (see Sect. 2.2.4). Each sample of this KID therefore has a weight of $1/\sigma_k^2$ and

$$S_p = \frac{1}{\sum_{k,t} 1/\sigma_k^2} \sum_{k,t} \frac{m_t^k}{\sigma_k^2}, \quad (2.6)$$

$$\sigma_p^2 = \sum_{k,t} 1/\sigma_k^2, \quad (2.7)$$

where σ_p^2 is the variance associated to pixel p . The pipeline automatically projects one map per array and a combined 1 mm map and takes a small enough resolution to respect the Nyquist criterion on the beam sampling. To keep margin and for the sake of simplicity, we usually take 2 arcsec resolution pixels.

In practice, and although the data cleaning procedure described in Sect. 2.2.4 significantly reduces the low frequency component of TOIs, the residual noise is still not completely white nor KID independent. The correlation matrix is not strictly zero to begin with (Fig. 2.4) and when looking at the distribution of the SNR on maps and variance maps obtained with Eqs (2.6,2.7), the distribution is Gaussian, but not normalized to unity (see Fig. 2.7). This is due to the remaining correlations between TOIs before projection. At this stage, rather than putting more effort in TOI processing, we renormalize the width of the Gaussian noise, which actually increases the map variance by the required factor so that the SNR distribution becomes normalized. This normalization factor varies from scan to scan but it is usually between 1.2 and 1.5. It is estimated on the background of the map, i. e. far from the source.

When several scans of the same source are averaged, we apply an inverse variance weighting as well. Weights are taken from the variance maps of each scan, corrected for the excess variance mentioned in the previous paragraph. The final variance map of the sum of scans is also corrected for such a factor if necessary.

2.2.6 Photometry

Throughout this document, we adopt the following convention. Assuming the beam is a perfect Gaussian of known $FWHM = \sigma\sqrt{8\ln 2}$, the instantaneous signal measured by a KID is

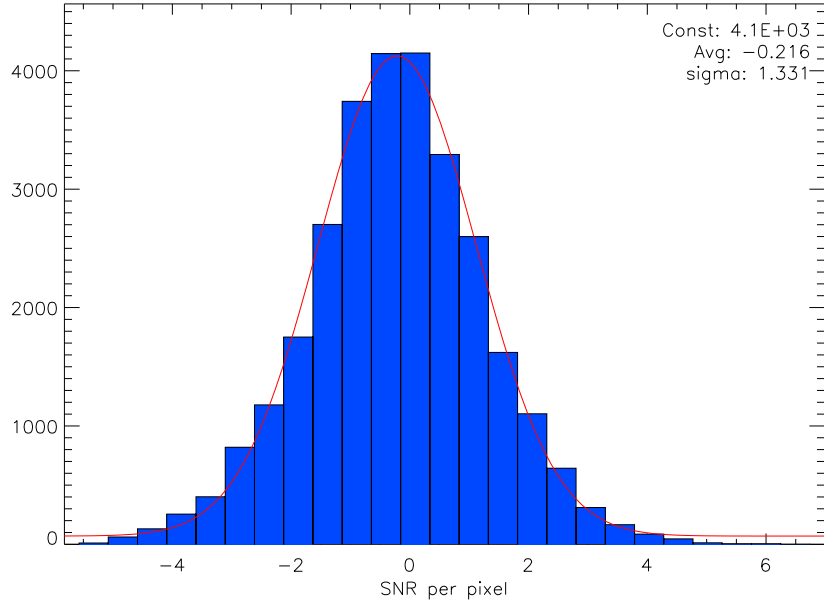


Figure 2.7: Histogram of the SNR per beam on a scan of weak source (G2, see Sect. 8.2). While the histogram is Gaussian, its width is not normalized to 1 due to residual correlated noise between the TOIs. This factor is accounted for before delivering the final variance map and associated flux estimates.

$$m^k(x, y) = \phi e^{-(x^2+y^2)/2\sigma^2} = \phi G(x, y) \quad (2.8)$$

with ϕ the flux of the source. In practice, the beam is not a perfect Gaussian and significant side lobes must be accounted for (Sect. 5). If the beam was perfectly known and stable, we could in principle replace the Gaussian form in Eq. 2.8 by the beam pattern and fit for the amplitude ϕ . In practice, we have found that it was enough as a first approximation to take an equivalent effective Gaussian width and use it to derive the beam template. We take 12.5 and 18.5 arcsec FWHM at 1 and 2 mm respectively and compute all our fluxes with these values. We do this for both analyzed point sources and for absolute calibrators to be consistent. Our photometric system is further detailed in Sects. (6.1, 6.2).

Let's call s_p the measured signal at pixel p and denote by g_p the Gaussian weight given to pixel p as a function of its distance to the source, as defined in Eq. 2.8. The amplitude fit is performed with an usual maximum likelihood approach. We assume that the renormalization of the variance map described in the previous section is enough to account for the residual noise correlations from pixel to pixel and therefore take the pixels to be independent in this estimator:

$$\hat{\phi} = \frac{1}{\sum_p g_p^2 / \sigma_p^2} \sum_p s_p \frac{g_p}{\sigma_p^2} \quad (2.9)$$

$$\sigma^2(\hat{\phi}) = \frac{1}{\sum_p g_p^2 / \sigma_p^2} \quad (2.10)$$

In the case of Gaussian white noise, this maximum likelihood estimator coincides with the classical minimum variance estimator and thus provides the best SNR estimate of the source flux.

2.3 Calibration and commissioning observations at the 30 m telescope

This section presents the different observation modes that have been used with NIKA2 for both commissioning and scientific purposes. Some of them are common to usual IRAM observing modes (e.g. "on the fly" raster scans), some of them have been designed specifically for NIKA2 (e.g. the focus sequence). We start by a short overview of a typical set up sequence at the beginning of a run. This will put each observation mode in perspective. Then we go into more details about the performances of the system.

2.3.1 Overview of different types of scans

Once the KIDs are tuned and NIKA2 is ready for observations, before actually observing a scientific target, one needs to adjust the focus and pointing of the telescope. On EMIR typically, these two parameters are adjusted iteratively by alternating a "pointing" (a. k. a. "cross") and "focus" scans to optimize the centering of a bright point source on a reference detector and maximize the incoming flux on it. With NIKA2, mostly due to absence of horns, this procedure is not optimal. Indeed, it was noticed that the position of the source moved by several arcsec with the displacement of M2 and this would alter the flux measurement on a fixed reference position too much to enable focus optimization.

To solve this issue we have designed a specific focus procedure that takes advantage of the dense sampling of the FOV that allows to map a source with only a few subscans. We perform a series of five successive short raster scans of a bright point source at five M2 position offsets, typically $\{-0.8, -0.4, 0, 0.4, 0.8\}$ mm w.r.t. the current z -focus. We then analyse each map to optimize the z position of M2. More details are given in Sect. 2.3.2. Once the focus is correctly determined, the pointing corrections are derived from an EMIR like pointing calibration scan (Sect. 2.3.4). The instrument is then ready to observe scientific targets.

2.3.2 Focus

The best axial focus in the central region of the arrays is estimated using the so-called *focus_OTF* PAKO script, which produces a series of five $1' \times 5'$ OTF scans at various values of the focus in 0.4 mm steps around an *a priori* value z_0 , namely $z \in \{-0.8, -0.4, 0, 0.4, 0.8\} + z_0$. Elliptical Gaussian fits on the reconstructed maps provide estimates of the flux and FWHM along minor - and major - axes for each focus. Parabolic fits are then used to determine the best focus. We consider three estimates: i) \hat{z}_{peak} the focus that maximizes the estimated flux, which is the amplitude of the 2D Gaussian, ii) \hat{z}_{fwhm} the focus that minimizes the geometrical FWHM, defined as the quadratic mean of $\text{FWHM}_{\text{major}}$ and $\text{FWHM}_{\text{minor}}$, and iii) \hat{z}_{ellipt} the focus that minimizes the beam ellipticity, defined as $\text{FWHM}_{\text{major}}/\text{FWHM}_{\text{minor}}$. Fig. 2.8 shows an example of such a sequence. When deciding on the focus to apply, we give priority to the optimal flux, taking an average between values on A1 and A3: there is little difference between the two and the 2 mm channel is less sensitive to the focus change than the 1 mm.

Draft

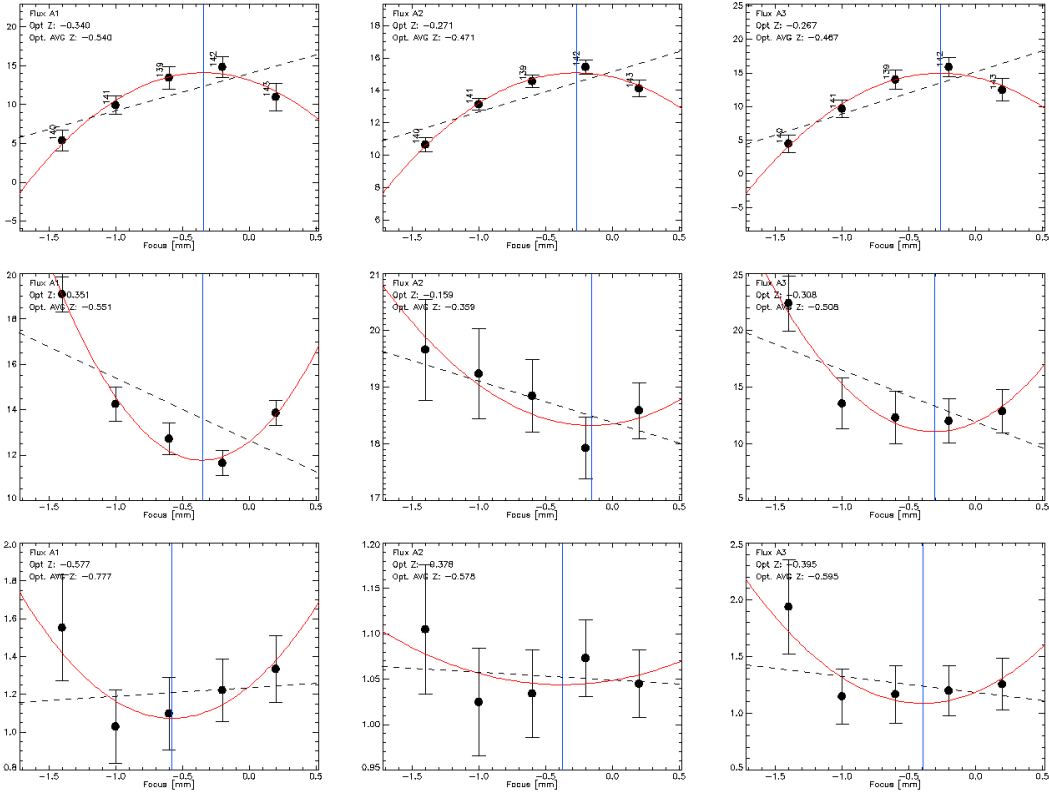


Figure 2.8: Example of axial focus measurement using a *focus_OTF* observation of Neptune during N2R10. The blue vertical line locates the optimal value of each fit. The optimal values derived from flux maximization and FWHM minimization agree to better than 0.1 mm in these conditions of observation. While ellipticity may be regarded as a confirmation more than a decisive criterion (due to larger uncertainty on its measure), the associated minimum is also in good agreement with the values derived from flux and FWHM measurements.

As presented in more details in Sect. 4.3, the focus surface is not strictly flat across the FOV. The way sources are scanned in this *focus_OTF* sequence is designed to save time but it gives more weight to the central KIDs. Hence, the optimal focus derived from the fits is biased. To account for the curvature of the focus surfaces and optimize the average focus across the FOV, we add -0.2 mm to the focus value as derived in the previous paragraph. **This focus offset is derived using ZEMAX simulation and it is verified on data as discussed in Sect. 4.3.**

2.3.3 Lateral focus

Like in the z (optical axis) direction, it is possible to control the position of M2 along the x and y directions. We have tried to determine if there was an optimal position in the (x, y) plane that would improve further measures with NIKA2. We have applied the same procedure as the one described in Sect 2.3.2, this time varying the position of M2 along x or y rather than along z . Examples of such observations are presented on Figs. 2.9 and 2.10. While the forced parabola fit guides the eye towards optimization, one should note the size of the error bars and the relatively low variations compared to M2 displacements along the z axis. This is expected from optical

simulations and experience on EMIR. Figs. 2.9 and 2.10 also show as complement, images of the residuals of the intensity maps at each M2 position after the subtraction of an elliptical gaussian fitted only on a disk of 6 and 15 arcsec (1 and 2 mm resp.) around the maximum location and outside a ring of 100 arcsec away from the maximum (to fix the background while not being affected by the side lobes). These maps of residuals are meant to help decide on a minimization criterion and x or y -focus value.

While we have performed “many” such observations and explored the entire parameter space of the (x, y, z) triplet position in a reasonable range of several millimeters around a fixed position, it has not been possible to demonstrated that any (x, y) positions would improve significantly the focalization of the whole system compared to the nominal $(0, 0)$ reference position. **This confirms the experience of the IRAM staff with EMIR and HERA who only act on this (x, y) position about once a year after specific, dedicated and delicate measures. This effort is necessary to find an optimum lateral focus position which is stable with elevation. For NIKA2 the adopted strategy has been not to change the lateral focus parameters and only rely on z-focus optimization for observations. However, lateral focus measurements with NIKA2 have to be scheduled in the future.**

2.3.4 Pointing

Once the instrument is correctly focused, we can estimate pointing corrections before scientific observations. **Even though EMIR only has a single pixel on the sky, the pointing procedure used for NIKA2 is very similar and is described in the next subsections.**

Pointing monitoring Based on general operating experience at the 30 m telescope, we use the so-called *pointing* or *cross* scans to monitor the pointing during observations. The telescope executes a back and forth scan in azimuth and a back and forth scan in elevation, centered on the observed source. Looking at the timeline profiles of the reference detector, we fit gaussian profiles and derive the current pointing offsets of the system in azimuth and elevation. These offsets can then be passed to PAKO to recenter the next scan (Fig. 2.11).

Pointing session Such scans and their analyses are also used to improve the pointing model of NIKA2. A pointing session consists in observing about 30 sources on a wide range of elevations **and azimuth angles** while monitoring the pointing offsets that are measured for each observation. These offsets are then passed to the IRAM staff who finds the pointing model parameters that minimize and symetrize the scattering of these offsets. Bases on these results Nasmyth offsets are then modified. Fig. 2.12 shows the pointing corrections that had to be applied during Run9, before and after the modification of the Nasmyth offsets. The dispersion of the offsets is the figure of merit of the pointing corrections. Their distribution after the corrections (in yellow to red) is clearly more symmetric and narrower than before. During N2R9 run, the pointing accuracy was 1.62 arcsec rms in azimuth and 1.37 arcsec rms in elevation.

2.3.5 Skydip

A skydip scan consists in a step-by-step span of a large range of elevations. This is used in order to calibrate the KIDs response to the atmosphere for opacity derivation, as discussed in Sect. 3. Namely, a skydip comprises eleven steps in the elevation range from 19 to 65 degrees, regularly

Draft

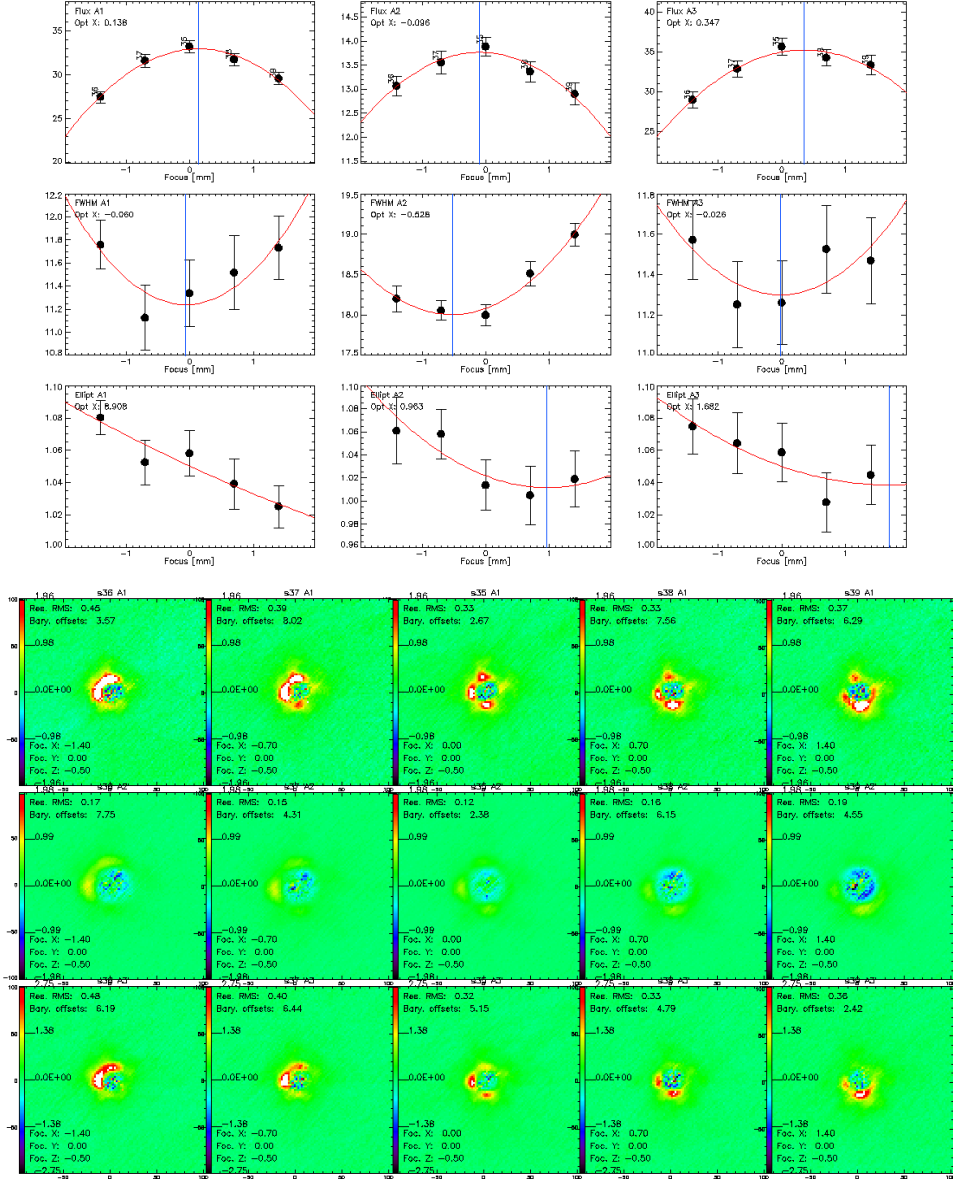


Figure 2.9: Left: X-focus measurement using a parabolic fit of the flux, beam fwhm and ellipticity on a sequence of five OTF scans on Uranus (20170223s39-43) **Right:** Beam residuals after subtracting a model of the main beam for each OTF-scan of the X-focus session. (N2R9)

spaced in airmass. For each step, we acquire about twenty seconds of time traces to ensure a precise monitoring of each KIDs. KIDs are tuned at the beginning of each subscan (hence once per airmass). The variation of their resonance frequency reads

$$f_{\text{tone}}^k = C_0^k - C_1^k T_{\text{atm}} [1 - e^{-\tau / \sin \delta}] \quad (2.11)$$

An illustration is presented on Fig. 2.13. More details on the analysis of these skydip scans are given in Sect. 3.

Draft

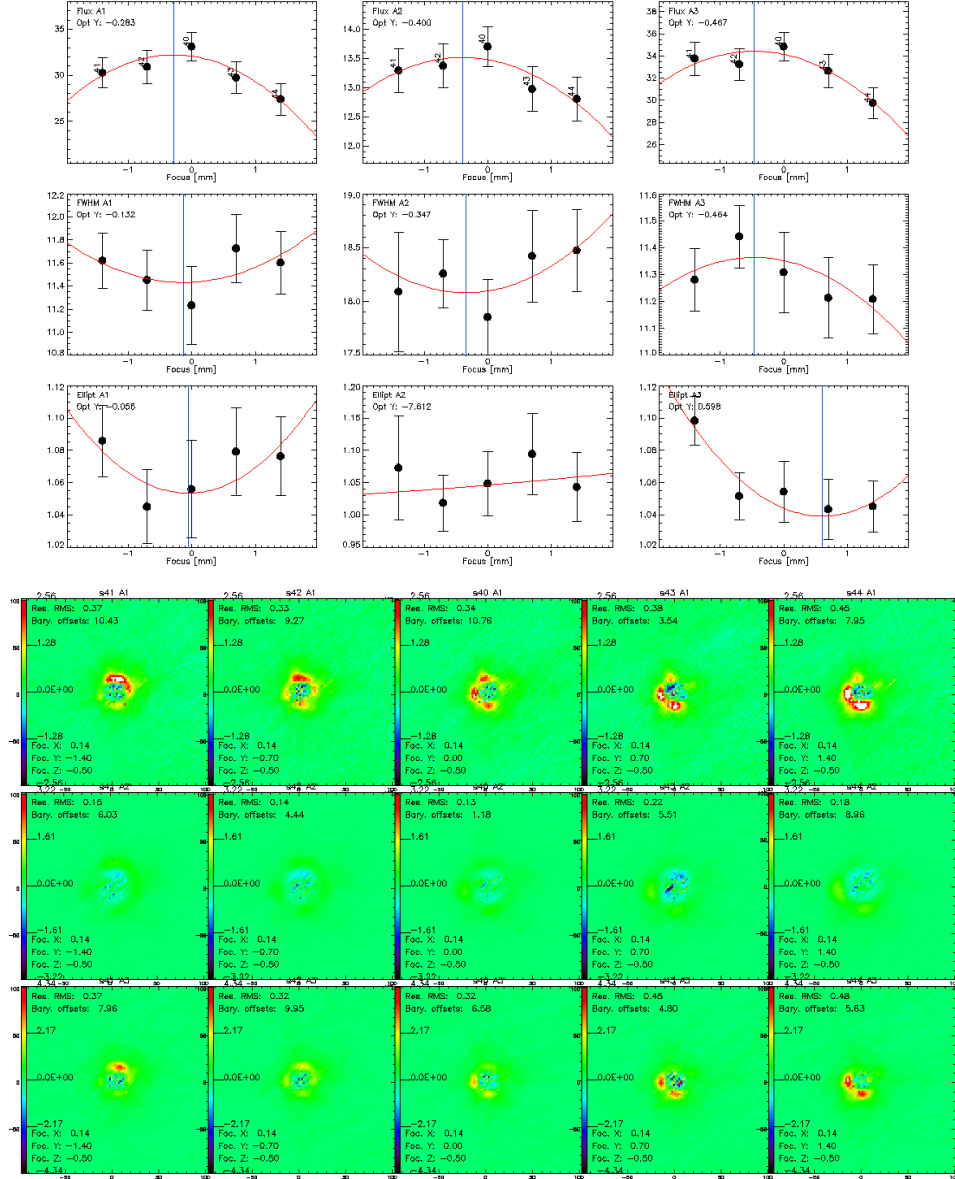


Figure 2.10: **Left:** Y-focus measurement using a parabolic fit of the flux, beam fwhm and ellipticity on a sequence of OTF scans on Uranus (20170223s44-48). **Right:** Beam residuals after subtracting a model of the main beam for each OTF-scan of the Y-focus session. (N2R9)

2.3.6 beammaps

A *beammap* is a map of a bright and compact source, most of the time a planet, with an elevation step small enough to meet Nyquist sampling of the 1 mm beam, namely 4.8 arcsec. We observe this planet with a raster scan in (az,el) coordinates of 13×7.8 arcmin 2 , either with fixed elevation subscans or fixed azimuth subscans. The former has the advantage of low air mass variation across a subscan, the latter offers an orthogonal scan direction to the former: the combination of both gives a more accurate determination of the far side lobes. The scan size ensures that the entire FOV is observed with good margins for beam mapping even on the edges and good

Draft

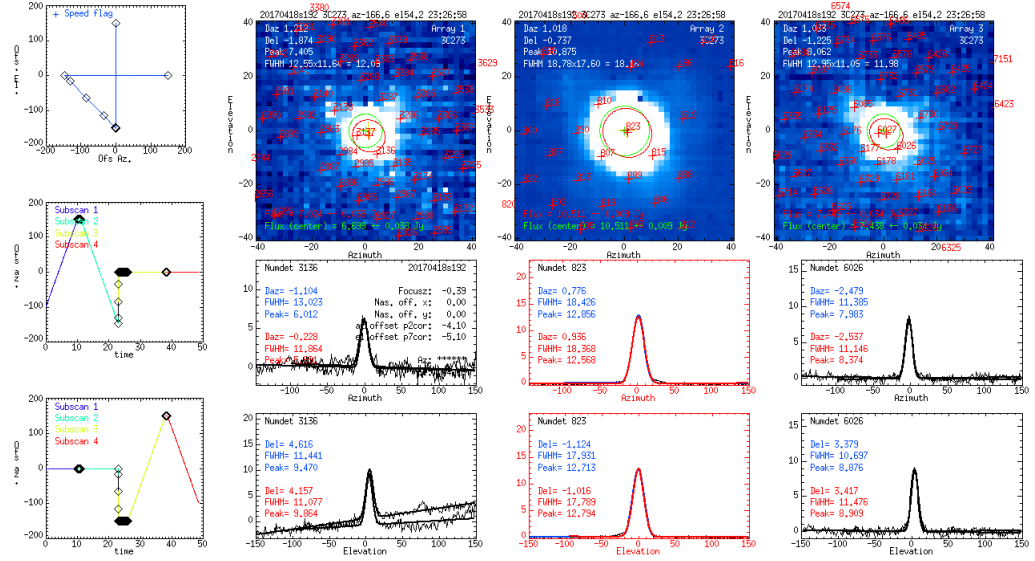


Figure 2.11: There is one combined map per array to check the overall quality of the scan, and a set of azimuth and elevation profiles for one reference detector per array. The 2 mm reference detector, highlighted in red, is the pointing reference detector of NIKA2. The location of the peak in azimuth and elevation, as observed by the reference detector gives the pointing offsets of the current scan.

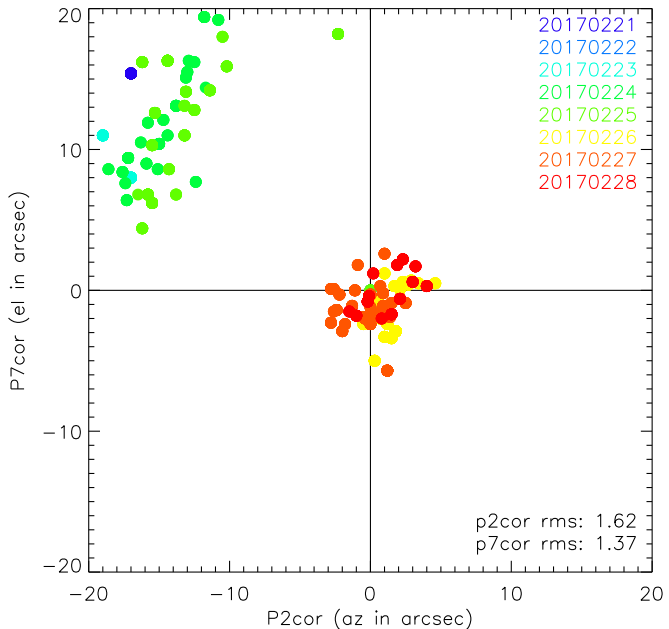


Figure 2.12: Pointing offsets during Run9 observations, before (blue to green) and after (yellow to red) the derivation of Nasmyth offsets with a pointing session on Feb. 26th, 2017.

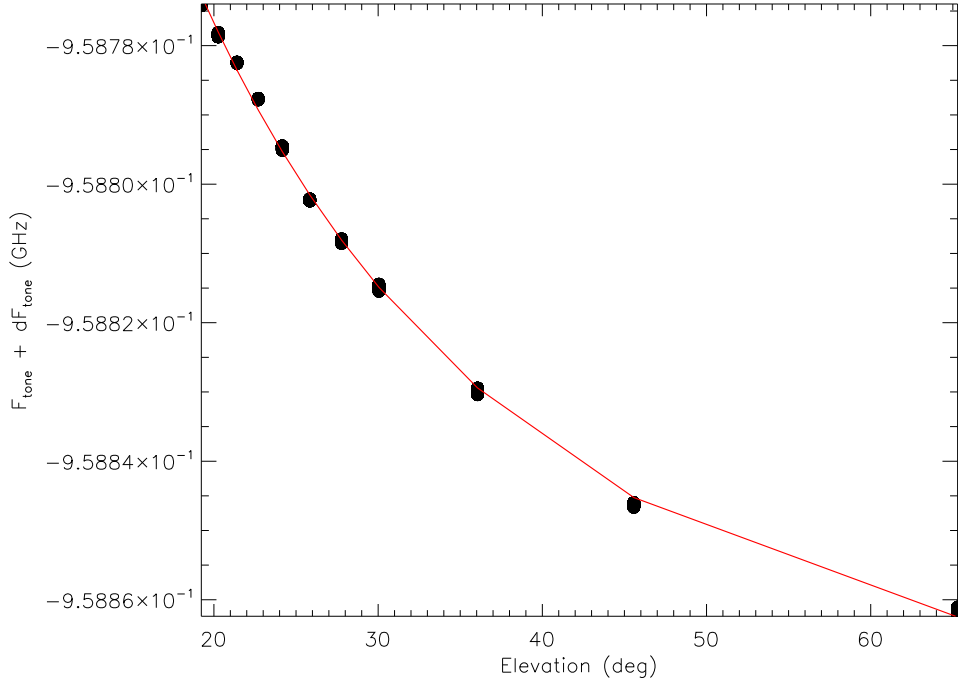


Figure 2.13: Variation of the resonance frequency of kid as a function of the elevation during a skydip scan.

margins for baseline derivation and subtraction in the scanning direction. During subscans, the telescope travels at 65 arcsec/s. This value results of a tradeoff between the need to scan as fast as possible to minimize atmospheric contamination and the necessity to keep subscans no shorter than 10 s (telescope constraint). The need to have Nyquist sampling of the beams along the scan direction translates into a maximum speed of 110 arcsec/s for our nominal acquisition rate of 23.8 Hz and is thus largely met. Subscans last 12 s, the entire scan lasts about 25 min, which is short enough to prevent too much variation of KID tuning under stable weather conditions on this timescale.

More details on these observations are given in Sect. 4 where we describe how to actually exploit them to derive individual KID properties.

2.3.7 Data selection

For calibration and performance assessment, we select scans in average observing conditions by performing mild selection cuts. These scan cuts rely on zenith opacity estimates in NIKA2 bands τ , as described in Sect. 3, and on the observation date:

- i) $\tau_3 < 0.5$, where τ_3 is τ estimate for Array 3, corresponding to a decrease of the signal by a factor of two at 45° of elevation;
- ii) $x \tau_3 < 0.7$ and $\delta > 20^\circ$, where δ is the elevation of the telescope and x the air mass, which depends on the elevation as $x = \sec \delta$. This threshold corresponds to a decrease of the signal by a factor of two;

- iii) observation date from 22:00 to 9:00 UT and from 10:00 to 15:00, that is excluding the sunrise period and the late afternoon.

As discussed in Sect. 6.5, the late afternoon observation are impacted by telescope-driven beam broadening. Around sunrise, the focus shifts continuously due to the ambient temperature change until the temperature stabilizes, so that the scans taken from 9:00 to 10:00 UT are likely not to be optimally focused. After the focus stabilisation, morning period from 10:00 to 15:00 UT offers stable observing conditions if the telescope is not heated due to observations in a direction close to the Sun. Otherwise, further scan selection based on the observation exact historic might be needed before using these observations for performance assessment.

In addition to the above scan selection cuts, we use a Gaussian beam size criterion for the absolute calibration on Planets (e.g. Uranus). Namely, the FWHM estimated from the Planet observation map is asked to be lower than $12.5''$ at 1 mm and lower than $18''$ at 2 mm. In further mitigating the flux scatter due to beam broadening, we ensure better accuracy of the absolute calibration.

Chapter 3

Opacity derivation

Only a fraction of the signal is transmitted by the atmosphere and reaches NIKA2 detectors. The relation between uncorrected observed flux densities \tilde{S}_ν and top-of-the-atmosphere flux densities S_ν is parametrized by the zenith opacity τ_ν and the line-of-sight airmass $x = (\sin \delta)^{-1}$ (δ is the elevation), such as

$$\tilde{S}_\nu = S_\nu e^{-\tau_\nu x}. \quad (3.1)$$

An accurate derivation of the opacity condition for each scan is required in order to retrieve the source signal at the top of the atmosphere. Opacity correction uncertainties even prevail in the final calibration error budget.

We developed three opacity derivation methods, which are discussed in the sections below, and we extensively tested their robustness against observing conditions. The ‘taumeter’ method discussed in Sect 3.1 relies on measurements provided by the resident IRAM tau-meter operated at 225 GHz and a fit of the opacity estimates in NIKA2 frequency bands by imposing the flux density stability against atmospheric conditions. The ‘skydip’ method described in Sect 3.2 consists in using NIKA2 as a taumeter (assuming the resonance frequencies are linearly related to the total power) by resorting to a series of skydip scans, the selection of which is addressed in Sect. 3.3. Finally, the ‘corrected skydip’ method presented in Sect. 3.5 is a modified version of the ‘skydip’ method that minimizes the dependence of the measured flux density on the opacity.

3.1 Taumeter-based method

The IRAM 30-m telescope facility is equipped with a resident taumeter, which performs elevation scans at a fixed azimuth and is operated at 225 GHz, to monitor the atmospheric opacity. Time-stamped zenith opacities at 225 GHz $\hat{\tau}_{225}$ are derived from the taumeter measures by Dr. Dave L. John. Two different $\hat{\tau}_{225}$ estimates are fitted, one relying on a linear model and the other on an exponential fitting model. The $\hat{\tau}_{225}$ estimates are then filtered using the cuts $0 < \hat{\tau}_{225} < 1.2$ and $R^2 > 0.99$, where R is the correlation coefficient between the two flavours of $\hat{\tau}_{225}$ estimates. Redundant samples and outliers are removed.

For the NIKA2 analysis we use the linear filtered $\hat{\tau}_{225}$ data. The time-stamped $\hat{\tau}_{225}$ estimates, which are sampled about every 4 minutes, are interpolated to the time of the NIKA2 scans (we consider the time of the middle of the scan). For crosscheck we also produce a smooth

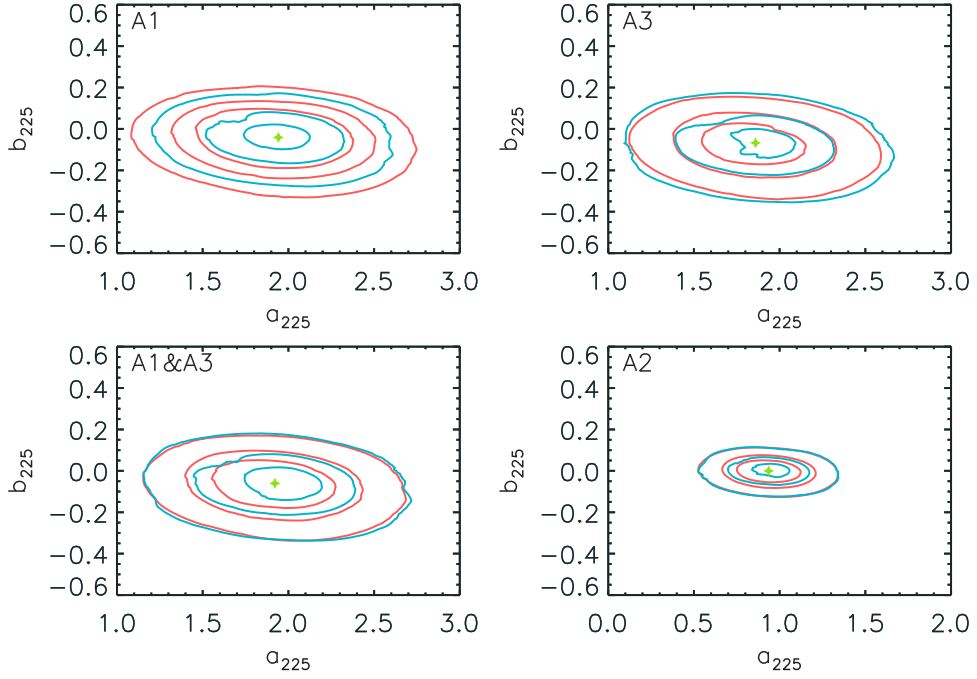


Figure 3.1: IRAM 225GHz taumeter to NIKA2 opacity relation fit. The a_v^{225} and b_v^{225} parameter space is explored for Array 1 (upper left), Array 3 (upper right), the combination of 1mm arrays (lower left) and Array 2 (lower right). The red contours correspond to rms errors of the measured-to-median flux density ratio of 9%, 10% and 12% at 1mm and 4.5%, 5% and 6% at 2mm. The blue contours are the 68, 95 and 99% confidence level contours of the parameters estimated using the χ^2 minimization. The best fit values are shown as green stars

We fit the relations between the IRAM 225 GHz taumeter opacities and NIKA2 band pass opacities using observation of calibration sources which spans a large range of air masses. We use a series of 64 scans of MWC349, which consists of the baseline selected subset of scans from the 68 available scans for this source during N2R9. It constitutes an homogeneous data set in flux density but heterogeneous in atmospheric conditions: zenith opacities at 225 GHz range from 0.08 to 0.32 and elevations from 23 to 73 degrees, spanning a large range of air mass as required. NIKA2 opacities τ_ν , for ν corresponding to Array 1, 2, 3 and the combination of Arrays 1 and 3, are estimated from the 225 GHz taumeter median-filtered exponential-based opacity estimates τ_{225} as

$$\tau_\nu = a_\nu^{225} \tau_{225} + b_\nu^{225}, \quad (3.2)$$

where the parameters a_ν^{225} and b_ν^{225} are fitted to ensure that the non-corrected flux densities \tilde{S}_ν are stable against τ_{225} after correction of the atmospheric attenuation by inversion of Eq. 3.1 using

$$S_\nu = \tilde{S}_\nu e^{(a_\nu^{225} \tau_{225} + b_\nu^{225}) \cdot x}. \quad (3.3)$$

We tested two estimators of the flux stability. The first one relies on minimising the standard deviation of the measured-to-median flux densities ratio after correction of the opacity using

Eq. 3.3. The second one consists in rewriting the rms minimisation as an unweighted χ^2 minimisation using:

$$\chi^2 = \sum_{i=1}^N \frac{1}{\sigma^2} \left(\frac{S_\nu}{Med(S_\nu)} - 1 \right)^2, \quad (3.4)$$

where σ is the rms error of the flux density estimates. Note that these estimators do not depend on the absolute scale of the flux density of the source.

Figure 3.1 show the two flux-stability estimate contours in the parameter plane $(a_\nu^{225}, b_\nu^{225})$, as well as the best-fitting parameter values. We find $a^{225} = [1.94, 1.86, 1.92]$ and $b^{225} = [-0.04, -0.07, -0.06]$ for A1, A3, and the 1 mm array combination, while $a^{225} = 0.94$ and $b^{225} = 0$ for A2. Uncertainties are of about 0.1 for the a^{225} parameter and about 0.05 on b^{225} .

Because the IRAM tau-meter observes at a fixed azimuth, the taumeter-based opacities are not exactly the line-of-sight opacities for the observation scans. As discussed in Sect. 7.4, this induces larger rms errors of the top-of-the-atmosphere flux density estimates with respect to opacity correction methods that relies on skydip-based measurements using NIKA2 instrument itself. The taumeter-based method will thus be used as an alternative method in case of failure of the NIKA2 skydip-based methods and ii) to perform consistency checks.

3.2 Skydip-based method

In NIKA2, the opacity is measured via a total-power technique, which was successfully tested with NIKA [23]. The underlying idea is to replace the opacity, usually delivered by the resident IRAM tau-meter by a measurement that uses the NIKA2 instrument itself as a tau-meter. Using this procedure we can directly derive an opacity integrated in the NIKA2 bandpasses and in the same line-of-sight of the source in the considered map. For that purpose, we assume that the resonance frequency of each KID varies linearly with the total power. First, we have to calibrate the relationship between total power and opacity. Then we can use that calibration to measure the opacity during a given scan.

For each KID k , the absolute value of the resonance frequency f_{reso}^k moves with the atmospheric load according to

$$f_{reso}^k = c_0^k - c_1^k T_{atm} [1 - e^{-\tau x}] \quad (3.5)$$

where c_0^k is a constant equal to the resonance frequency at zero opacity, c_1^k is the calibration conversion factor in Hz/K, T_{atm} is the temperature of the atmosphere (taken as a constant at 270 K, we therefore neglect the atmospheric temperature variations), τ the zenith opacity and δ the elevation of the telescope. By assuming a homogeneous plane-parallel atmosphere, the airmass x is defined from the elevation as $x = (\sin \delta)^{-1}$ (we neglect the Earth sphericity).

The coefficients c_0^k and c_1^k are expected to be constant in time within at least a cooldown cycle (because the coupling of NIKA2 to the telescope does not change), and are determined using a skydip procedure. This consists in moving the telescope in elevation step by step, that is, performing a skydip scan, as defined in Sect. 2.3.5, and monitoring, for each KID, the evolution of f_{reso}^k versus the airmass and to fit the zenith opacity τ and c_0^k and c_1^k . The acquisition time spent on each elevation step, which is of about twenty seconds, is chosen to reduce the error in the determination of f_{reso}^k .

All skydips, obtained under various opacity conditions, are analysed together to break the degeneracy between the opacity and the responsivity (c_1^k). The degeneracy occurs mostly for

low opacity conditions for which we can only determine the combination $c_1^k \tau x$. The procedure has two steps. First, all the skydips are analysed individually to simply extract f_{reso}^k for each stable elevation and each KID. Secondly, a simultaneous fit is done for all parameters (one τ per skydip, and a set of c_0^k and c_1^k for all KIDs). Fig 3.2 illustrates the fitting procedure. Error bars on τ are estimated by doing this procedure on blocks of 40 KIDs only and getting a dispersion on the resulting τ from the different blocks (the Mpfit routine does not allow more KIDs anyway). Usually the dispersion comes out as 4×10^{-3} at 1 mm and 1×10^{-3} at 2 mm. Once the τ values are estimated for each skydip (as the average over the blocks), we compute (while fixing the τ) the c_0 and c_1 final values for each KID with a simple linear fit. We thus retrieve the coefficients of all the KIDs even though some of them could not contribute to the τ determination (flagged in the first step).

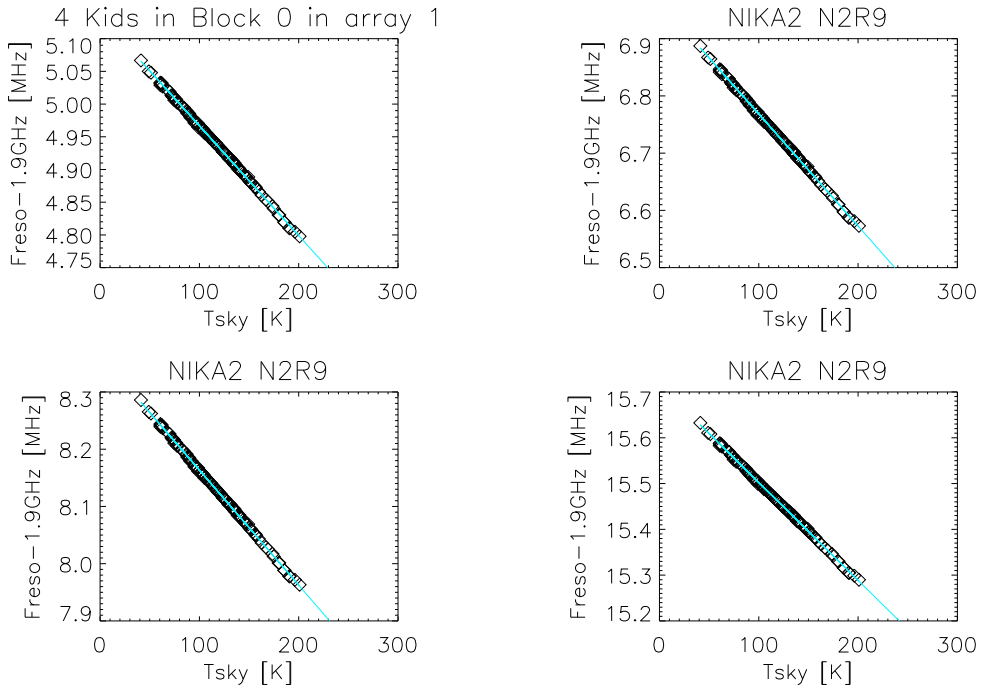


Figure 3.2: Example of the global skydip fit for four KIDs (one per plot). Each square point represents one step in a skydip (made of eleven elevation steps). 12 skydips are used together spanning zenith opacities from 0.15 to 0.50. The horizontal axis gives the sky effective temperature $T_{atm}[1 - e^{-\tau x}]$ where τ is the skydip zenith opacity found in the fit. The vertical axis shows the resonance frequency of the KID. The blue line is the expected linear fit implied by the found c_0^k and c_1^k coefficients (see Eq. 3.5).

We find that the skydip-fitted τ values are, as expected, common between different detectors of the same array. By comparing the results of different skydips, we have verified that the coefficients c_0, c_1 are stable, within the fit errors, on very long time scales within a cooldown cycle. The coefficients can thus be applied to the whole observing campaign in order to recover the opacity of each scan. Fig. 3.4 illustrates the stability of c_0 converted to equivalent temperature of the background. There is no apparent change of that background by more than 0.5 K.

The skydip-based procedure consists in fitting a couple of parameters (c_0, c_1) for each of the

several thousand valid KIDs. This requires to have on hands a sizable amount of skydip scans – typically ten to twenty – that i) span the whole opacity range and ii) avoid highly perturbated atmosphere to meet the plane-parallel atmosphere assumption. To that aim, we recommend to perform a skydip scan twice a day during a scientific campaign. Then the (c_0, c_1) determination process relies on a selection of the skydip scans.

3.3 Skydip selection

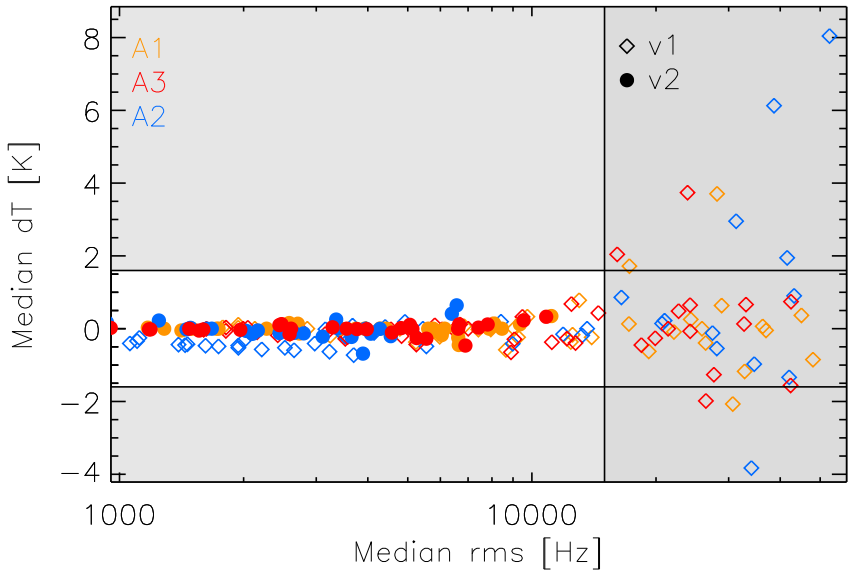


Figure 3.3: Median dT quality-fit criterion is plotted as a function of the median rms criterion for each skydip scan of the N2R9 campaign and for the three arrays. Both criteria are nicely correlated. Empty diamonds show the results of the first iteration of the skydip coefficient estimation, whereas filled circled show the second iteration, for which only the skydips that met both fit-quality criteria are included. After the second iteration, all the remaining skydips met the criteria.

For each skydip scan and for each bunch of 40 KIDs, we compute the difference between the measured KID resonance frequency and the model given in Eq. 3.5 taken at the best-fit values of the (c_0, c_1) parameters. Then we determine two indicators of the fit quality per skydip. First, the standard deviation of the measure-to-model difference is calculated over all the KIDs in a bunch. For each skydip, we evaluate the median rms, which is the median over the KID bunches of the standard deviation per bunch, given in Hz. Secondly, for each scan, we compute the average measure-to-model difference of each KID k , labelled dT_k , which is then converted from Hertz to Kelvin using the c_1 parameter of the KID k . Median dT is the median of dT_k over all the KID of an array. With these two indicators in hands, we discard the skydip scans that are noisy or that yield a poor fit by applying the selection criteria

- Median rms $< 1.5 \times 10^4$ Hz

- Median $dT < 1.6$ K

The threshold values have been determined using the set of 44 skydip scans of N2R9. The Median rms cut corresponds to twice the median of this quantity per skydip scan, whereas the Median dT cut is twice the standard deviation of Median dT over the skydips. N2R9 skydip scan selection is illustrated in Fig. 3.3, in which the agreement between the two fit-quality criteria is clearly seen. The (c_0, c_1) estimation proceeds in two steps: first the parameters are estimated using all the available skydip scans for a given campaign, then the estimation is re-iterated using the only skydip scans that met the fit-quality criteria. After the second iteration, we check that no extra skydip outlier are left, as shown by the 'v2' label data points in Fig. 3.3. After selection of the skydip scans acquired during the N2R9 campaign, 15 skydips are kept for the final step of the (c_0, c_1) fit.

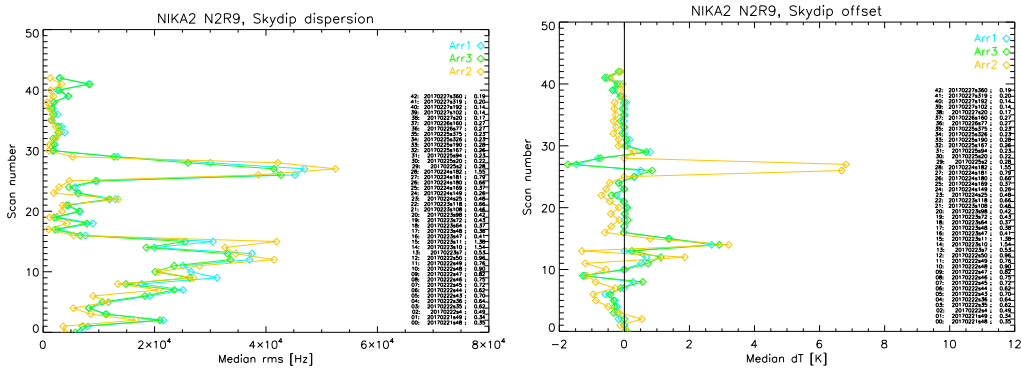


Figure 3.4: (left) rms dispersion of the skydip fit to the KIDs resonance frequency for almost all N2R9 skydips. The rms gives the quality of the plane-parallel hypothesis. (right) evolution of the background as observed by NIKA2 during the N2R9 run. During the whole run, there is no particular trend of that background with time (except for anomalous skydips).

We test the stability of the (c_0, c_1) parameters against the exact choice of the selection criteria. We derive (c_0, c_1) parameter sets for the N2R9 campaign using six skydip selections: the baseline selection (labeled 'base') consists in the fit-quality based selection described above, which comprises 15 skydips, the selection labeled 'incl' consists of an inclusive selection of 38 skydips in which only the noisier ones were discarded, the 'night' selection consists of 11 skydips acquired during between 21:00 and 09:00 UT, 'high 1' and 'high 2' are two different selections, which comprise 23 and 13 skydips and are based on fit quality criteria that are respectively relaxed or tightened with respect to the baseline criteria, and 'low' corresponds to a selection of 20 skydips acquired while $\tau_{1mm} < 0.44$. Each (c_0, c_1) sets are used to derive zenith opacity of the N2R9 calibration scans of MWC349. Figure 3.5 shows the relative difference between each τ estimates and the baseline τ estimates as a function of the baseline τ . The relative differences are basically constant for the whole opacity range: the main effect of the skydip selection is a normalisation factor on the τ estimates at both wavelengths. At both wavelengths, this factor is below 10% of the baseline τ for most of the skydip selections. However, this is of about 10% for the 'low' selection, which highlight the necessity of including good skydips acquired in high ($\tau_{1mm} > 0.44$) opacity conditions in the final selection. The 'incl' (inclusive 38-skydip based) selection results in the larger difference w.r.t. the baseline τ , which are up to 20% at 1mm and

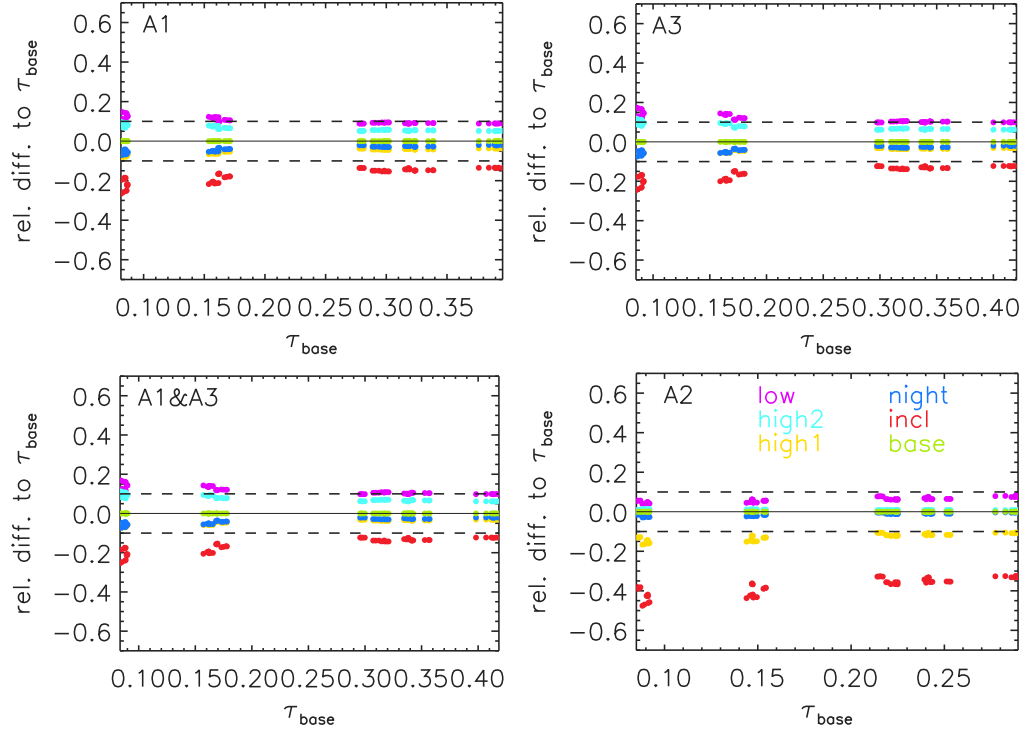


Figure 3.5: Skydip-selection impact on the opacity estimates. For a series of calibration scans of MWC349 acquired during N2R9, the relative difference w.r.t. the baseline opacities τ_{base} (labeled ‘base’) are shown as a function of τ_{base} for five skydip selections. The most inclusive one (labeled ‘incl’) includes 38 skydips of the 44 available. ‘night’ includes 11 skydips acquired during nighttime. ‘low’ consists of 20 skydips acquired in low opacity conditions. ‘high 1’ and ‘high 2’ are fit-quality based selections relying of relaxed (‘high1’) or tightened (‘high 2’) criteria w.r.t. the baseline criteria given in Sect. 3.3. The dashed lines figure a 10% opacity difference w.r.t. τ_{base} .

up to 40% at 2mm, whereas the ‘high 1’ (mild quality-fit) selection suffices to reduce the relative difference below 10% at 1mm and below 15% at 2mm. As a summary, the τ estimates are robust against the exact skydip selection as long as the selection includes good skydips in high opacity condition ($\tau_{1\text{mm}} > 0.44$) and as the poor fitting skydips are excluded. When these conditions are met, the skydip selection induced uncertainties are below 10% at 1mm and below 15% at 2mm.

We conclude that opacities at both wavelengths can be reliably estimated from a series of skydip scans using the (c_0, c_1) model.

3.4 Skydip-based opacity measurements and tests

We perform basic sanity tests of the zenith opacity measurements using the skydip-based method discussed in Sect. 3.2, and that are referred to as ‘skydip’ opacities hereafter.

First, we test the stability of the ‘skydip’ opacities from one observation campaign to another. Figure 3.6 shows the correlation between the ‘skydip’ τ estimates τ_{skydip} and the IRAM 225 GHz taumeter zenith opacities τ_{225} , which are described in Sect. 3.1, for a series of scans of Uranus

and MWC349 acquired during three campaigns. As guidelines, we also show the predicted correlations using an ATM model integrated in NIKA2 wavebands. At 1 mm, the τ_{skydip} to τ_{225} correlation relations are consistent for the three campaigns. They are also in agreement with the ATM model expectations. At 2 mm, more dispersion is observed between each correlation relations although they are compatible with each others within statistical errors. We note that the ATM model underestimates the measured τ_{skydip} . This mild discrepancy with the ATM model predictions is yet to be understood, but has no impact on our opacity measurements, which do not rely on any ATM model nor on the precision with which the observing bandpasses are known.

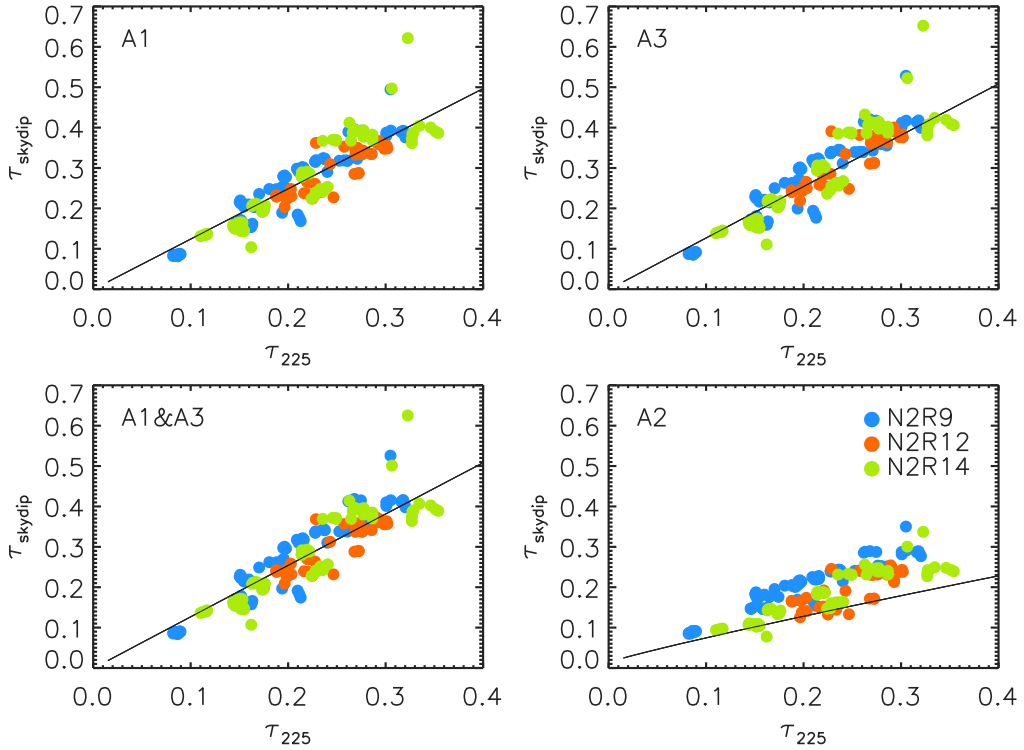


Figure 3.6: NIKA2 skydip-based opacities vs IRAM 225GHz tau-meter opacities. The modeled correlations relying on an ATM model integrated in NIKA2 bands are shown in black.

We check the robustness of the ‘skydip’ τ against the observing elevation. Figure 3.7 shows the ratio of NIKA2 ‘skydip’ opacities to the 225 GHz tau-meter opacities as a function of the average scan elevation. The ‘skydip’ opacity measurements have no sizable dependency on the elevation. Moreover, the ‘skydip’-to-tau-meter opacity ratios derived for Uranus scans and for the scans of the secondary calibrator MWC39 are in good agreement.

As a summary, the ‘skydip’ opacity estimates i) have reproducible correlation coefficients with the 225 GHz tau-meter opacities from a campaign to another, ii) are robust against the observing conditions, and iii) are stable for various sources.

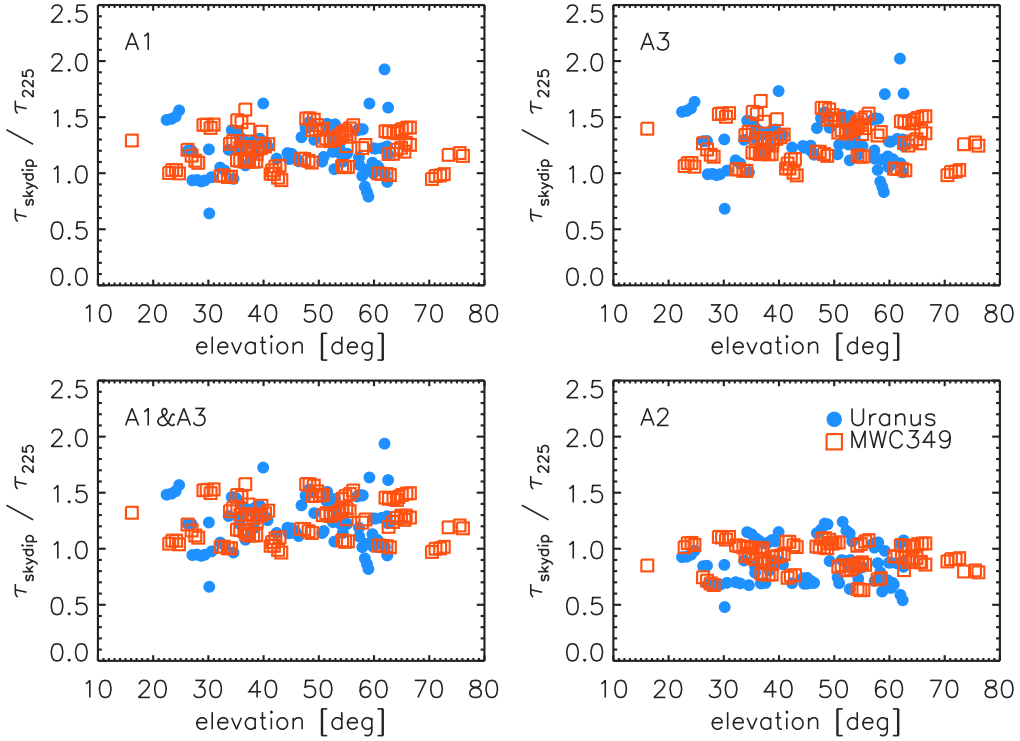


Figure 3.7: NIKA2 skydip-based opacities stability against the observing elevation. The ratio between the skydip-based opacities and the tau-meter-derived opacities is shown as a function of the observing elevation as blue points for Uranus scans and empty red square for MWC349 scans.

3.5 Corrected skydip method

The consistency checks presented in Sect. 3.4 constitute first robustness tests of the ‘skydip’ opacities. However, the opacity estimates are ultimately tested by assessing the stability of the top-of-the-atmosphere flux densities of bright sources for a large range of atmospheric conditions, as will be addressed in Chapter 7. After opacity correction using the skydip method, the calibration flux density measurements show a residual dependency on the atmospheric transmission, as discussed in Sect. 7.4. This motivates the development of a corrected version of the ‘skydip’ method, which is described in this section, that ensures the robustness of the flux densities against atmospheric conditions.

We use the flux stability estimators described in Sect. 3.1 to fit a correction to the skydip opacities τ_{skydip} as

$$\tau_\nu = a_\nu^{\text{skydip}} \tau_{\text{skydip}}. \quad (3.6)$$

We find a_ν^{skydip} of 1.36 ± 0.04 , 1.23 ± 0.02 , 1.27 ± 0.03 and 1.03 ± 0.03 for A1, A3, A1&A3 and A2 respectively.

Moreover, we test for an offset $b_\nu^{\text{skydip}'}$ in the correcting relation of the skydip opacities as

$$\tau_\nu = a_\nu^{\text{skydip}'} \tau_{\text{skydip}} + b_\nu^{\text{skydip}'} . \quad (3.7)$$

Draft

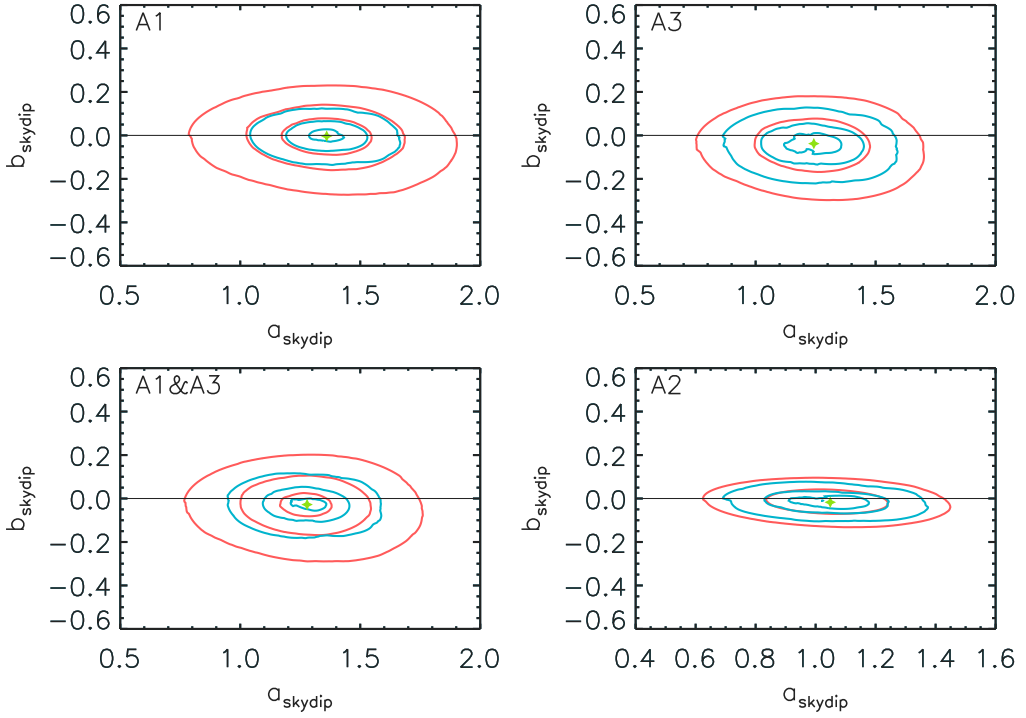


Figure 3.8: Fit of the skydip-based opacity correcting relation parameters. The flux-stability estimator contours are shown in the plan $a_{\text{skydip}} \equiv a_v^{\text{skydip}'} \text{ and } b_{\text{skydip}} \equiv b_v^{\text{skydip}'}$ for A1, A3, A1&A3 and A2. The red contours enclose rms errors of the measured-to-median flux density ratio of 5.5, 7 and 10% at 1mm and 2.7, 3.5 and 5% at 2mm. The blue contours correspond roughly to the 68%, 95% and 99% confidence levels drawn from the χ^2 estimates. The best fit values are shown as green stars. Offset $b_v^{\text{skydip}'}$ are compatible with zero within the 68% CL contours.

We repeat the estimation of the parameters of the correcting relation. Confidence level contours in the parameter plan using the two stability estimators are shown in Fig. 3.8, as well as the best-fitting parameter values. We find the best-fit $a_v^{\text{skydip}'}$ estimates of 1.36 ± 0.04 , 1.25 ± 0.07 , 1.28 ± 0.04 and 1.05 ± 0.05 for A1, A3, A1&A3 and A2 respectively, which are in agreement with the best-fit values estimated using the single-parameter correcting relation, whereas the best-fit values of the offsets $b_v^{\text{skydip}'}$ are compatible with zero at both wavelengths.

We conclude that correcting the skydip-based opacity estimates for a normalisation as given in Eq. 3.6 suffices for ensuring flux density robustness against atmospheric conditions. NIKA2 baseline results rely on zenith opacity estimates obtained with the corrected skydip method for the atmospheric attenuation correction. Assessment of the photometric capabilities using the data from three observation campaigns will be addressed in Sect. 7.3. **For the time being, we do not know the origin for the discrepancy of the empirical factor $a_v^{\text{skydip}'}$ from the expected unity value.**

3.6 Opacity monitoring

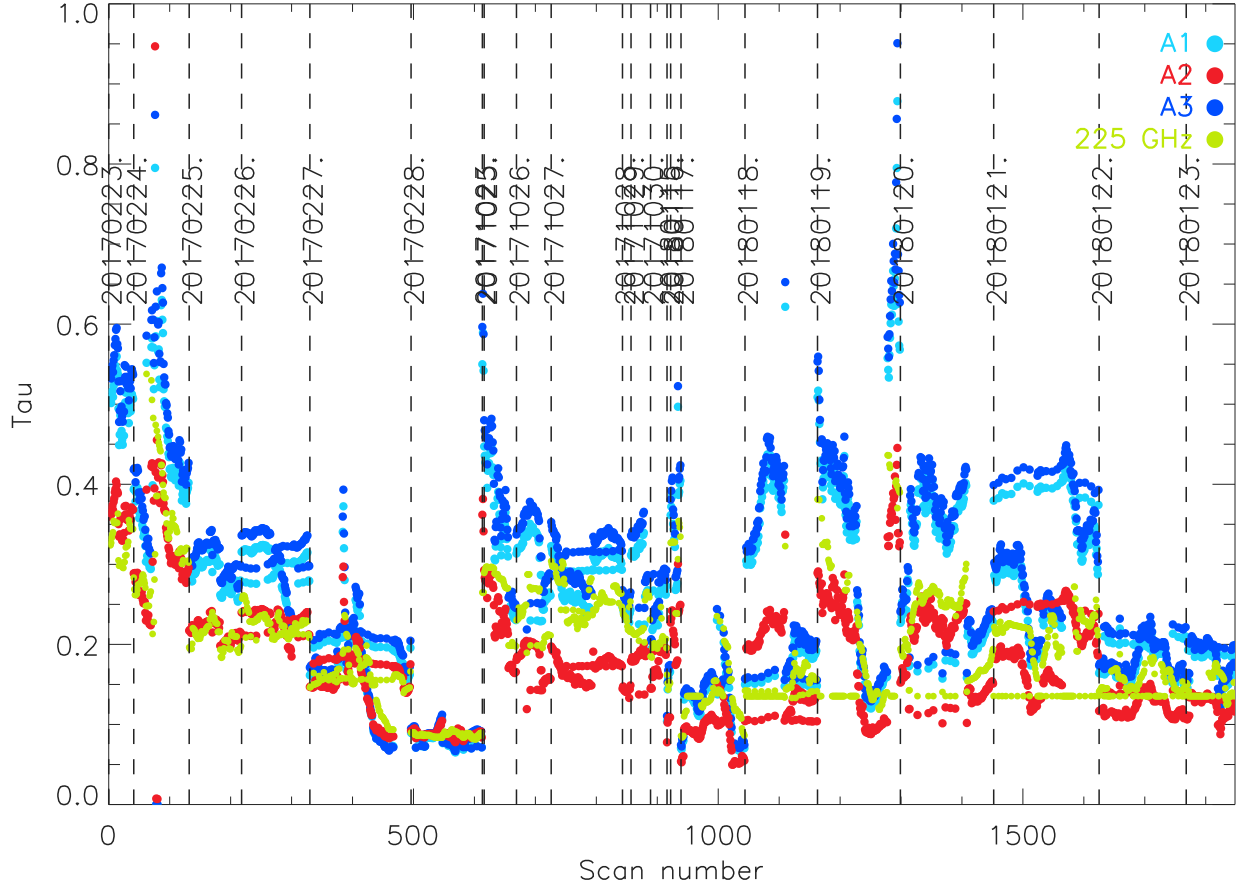


Figure 3.9: Atmospheric opacity as measured from the IRAM 225 GHz tau-meter (yellow green), and from the NIKA2 data at 150 (red) and 260 GHz (blue) during N2R9 commissioning campaign (Feb. 2017) and N2R12 (Oct. 2017) and N2R14 (Jan. 2018) scientific pools. We stress the fact that the IRAM 225 GHz tau-meter data is not used for the atmospheric correction and is plotted here for comparison only.

In Fig. 3.9 we present the evolution of the NIKA2 in-band opacities for all the ‘OTF’ scans (about 1300 scans per runs) of the N2R9 commissioning campaign (Feb. 2017) and N2R12 (Oct. 2017) and N2R14 (Jan. 2018) scientific pools. These are compared to the IRAM tau-meter values. For both opacity estimates, plateaux correspond to the repeated propagation of the last valid value in case of failure of the opacity measurement. We observe an agreement on the global trend between the IRAM tau-meter opacity (225 GHz) and the NIKA2 values. These latter show, however, a smaller dispersion (less than one percent).

Chapter 4

Focal Plane Reconstruction

4.1 Focal Plane Geometry

In order to be able to produce a map, one needs to associate a pointing direction to any data sample of the system. The telescope provides us with various pointing information for a reference position in the focal plane. We then need to know the relative pointing offsets of each detector. We use *beammaps* for this purpose (see Sect. 2.3.6). The determination of the KID offsets in the focal plane proceeds in two steps.

Step 1. We apply a median filter per KID timeline whose width is equivalent to 4 FWHM and we project one map per KID in Nasmyth coordinates. This median filter removes efficiently most of the atmospheric and low frequency electronic noise, albeit with a slight ringing and flux loss on the source. However, at this stage, we are only interested in the location of the observed planet. To derive the Nasmyth coordinates from the provided (α_t, δ_t) and $(\Delta\alpha_t, \Delta\delta_t)$ coordinates, we build the following quantities at time t :

$$\begin{aligned}\Delta x_t &= \cos \delta_t \Delta \alpha_t - \sin \delta_t \Delta \delta_t \\ \Delta y_t &= \sin \delta_t \Delta \alpha_t + \cos \delta_t \Delta \delta_t\end{aligned}$$

Note that $\Delta\alpha_t$ is already corrected by the $\cos \delta_t$ factor to have orthonormal coordinates in the tangent plane of the sky and be immune to the geodesic convergence at the poles. We then fit a 2D elliptical Gaussian on each kid map. The centroid of this Gaussian is a first estimate of the KID offsets, FWHM's, ellipticity and sensitivity. We apply a first KID selection by removing outliers to the statistics on these parameters. We also discard manually KIDs that show a cross-talk counterpart on their map.

Step 2. With these offsets, it is already possible to produce maps from the combination of all detectors. However, in order to go up to the calibration stage, we must correct for the flux loss induced by the median filter and ensure that each timeline is treated in the same way as the final observation will. For this, we apply the pointing reconstruction presented in Sect. 2.2.2 and the data reduction presented in Sect. 2.2.4. We still do not have absolute calibration for each KID (no opacity correction yet) but the amplitude of the fitted centroid on the same planet provides the required cross-calibration between KIDs. The final absolute calibration will be presented in

Sect. 6.

This analysis is repeated on all *beammaps* to obtain statistics and precision on each KID parameter, together with estimates on KID performance stability, as discussed in the next sections.

In order to identify the most stable pixels, we compare the KID parameters obtained with several *beammaps*. In the following, we show results as obtained using seven *beammaps* from Run10, two from Run9 and one from Run8. For each pixel we compute the average position on the focal plane and the average FWHM, counting the times that it has been considered as valid and at the same position. Indeed, a few KIDs have close resonances and can be tuned and switched on some scans. A few others must also be discarded because they appear identical numerically due to a remaining artefact in the acquisition. These KIDs are flagged out (less than 1% of the designed KIDs). In Fig. 4.1 we show the average focal plane reconstruction, from green to red depending on the number of times that the pixel has been considered as valid. For A1, A3 and A2, respectively, we have 952, 961, and 553 pixels that have been considered as valid at least twice (840, 508, 868 valid at least five times). Using this criterion, we deduce the fraction of valid detectors over the designed ones, as given in Table 4.1.

Array	Designed detectors	Valid detectors	Fraction
A1	1140	952	84%
A3	1140	961	84%
A2	616	553	90%

Table 4.1: Summary of the number of valid detectors per array.

4.2 FOV grid distortion

We studied the matching of the KID position on the sky to the design position. The global result is scaling, rotation, and shift parameters for each array. They are described in Table 4.2.

It shows that on average the position of each detector is known to better than an arcsecond. The 1 mm arrays have almost the same center but this center differs by 7 and 2 arcsec from the 2 mm array center. The sampling is above λ/D at 1 mm, assuming a 30 m diameter aperture. Note that the plate rotation angle was designed as 76.2 degrees, less than 2 degrees from what is observed. We find that array 1 has some of the most deviant detectors (above 4 arcsec from their expected position). These detectors should be excluded from further analysis. We call distortion (in the table) the x,y term in the polynomial fitting between the design grid and the observed position (the fitting is done with the x and y linear terms and the x,y term).

This has been compared to expectations obtained using ZEMAX simulation. The grid diagram generated using ZEMAX provides us with the maximum dispersion in the field defined by

$$P = \frac{\sqrt{(x_p - x_r)^2 + (y_p - y_r)^2}}{\sqrt{x_p^2 + y_p^2}}, \quad (4.1)$$

Draft

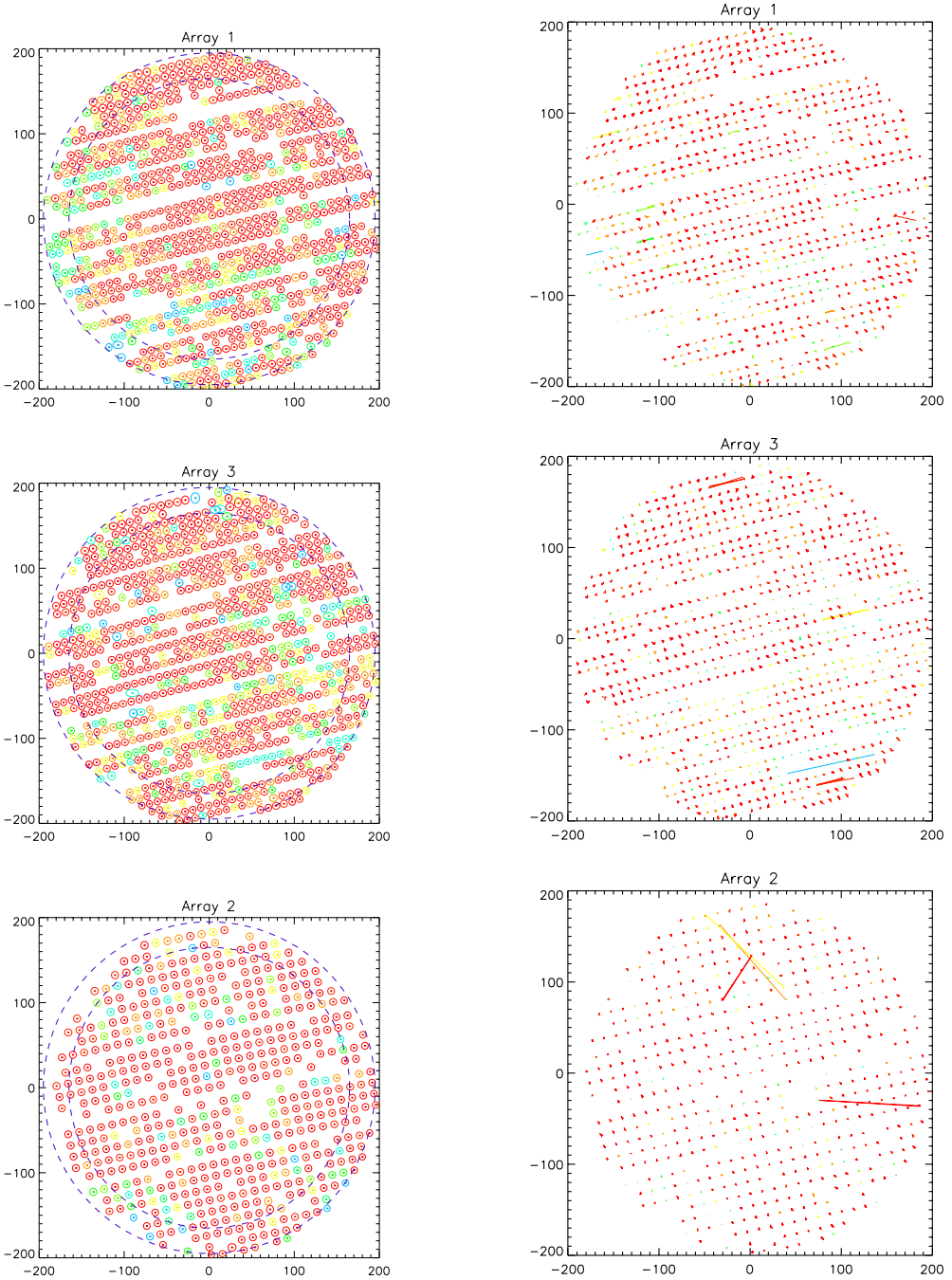


Figure 4.1: On each of these plots, the color indicates, from green to red, how many times a KID was identified as valid on a *beammap*. *Left column:* Average detector positions for arrays A1, A3, and A2. The three plots show the detectors that have seen the sky and passed the quality criteria for at least two *beammaps* during Run10, 9 and 8: 952, 961, and 553 for A1, A3 and A2, respectively. The inner and outer dash-line circles correspond to a FOV of 5.5 arcmin and 6.5 arcmin, respectively. Units are arcseconds. *Right column:* For valid detectors, we show the positions of each pixel, as obtained from each *beammap*. Some of them are not found at the same position for all the *beammaps* and are discarded. Units are arcseconds.

Array 1	Array 3	Array 2	Comment
1.25	1.25	2.05	λ in mm
1140	1140	616	Total of designed Kids (TDK)
673/736	734/758	437/444	Well-placed Kids (WPK)/Found Kids (FK)
91/59	96/64	98/71	Ratio [%] of WPK/FK and WPK/TDK
0.87	0.84	0.66	Median deviation (arcsec) for detectors deviating by less than 5 arcsec.
0.52	0.69	0.68	Mean distortion across the FoV in arcsec
2.3 -4.5	2.0 -5.8	9.3 -7.5	Array center in Nasmyth coordinates (arcsec)
4.90	4.88	4.88	Plate scaling (arcsec/mm) in the Design x and y (averaged)
77.3	76.4	78.2	Plate rotation angle (degree) from the Design to Nasmyth coordinates
6.6	6.6	6.6	FOV [arcmin] (Total kids)
9.8/2.00	9.7/2.00	13.3/2.75	Distance between near detectors [arcsec, mm]
1.11	1.10	0.87	Measured Distance between near detectors with 27 m effective diameter
1.09	1.09	0.93	Modeled Distance with Zemax

Table 4.2: Linear 2D fit of the observed position of the detectors in the sky against their mechanically designed position for N2R9. The initial table of Found Kids is given by the focal plane geometry procedure, as described in Sect. 4.1, applied to N2R9 *beammap* scans. More than 90% of the detectors (WPK/FK) are within less than 5 arcseconds of their expected position.

where (x_p, y_p) and (x_r, y_r) are respectively the predicted and real coordinates on the image surface relative to the reference field position image location (see page 170 of the ZEMAX manual, 2007). The predicted coordinates for the whole field are obtained using a linear interpolation of a small area in the field central part, whereas the real coordinates are calculated by ray tracing through the optical system.

Figure 4.2 show the ZEMAX grid diagram for NIKA2 simulated optic system. The maximum grid distortion is expected to be of 2.7% in NIKA2 6.5' FOV. The distortion is the most noticeable in the upper right corner of the Nasmyth plan, which is also the area of the largest defocus w.r.t. to the center.

An expected distortion of 2.7% is at most a 5 arcsecond shift from the center to the outside of the array. The quoted measured distortions are not too dissimilar once the different fitting methods have been taken into account. Auxillary information on this work can be found in this wiki post¹.

4.3 Reconstruction of the focus surfaces

Owing to the NIKA2 6.5 arcmin FOV, the focus is expected to slightly changes across the FOV, defining curved focal surfaces at the location of the three arrays. Therefore, beam patterns are expected to show some scatter across the FOV accordingly to the focal surfaces. Although all the detectors cannot be individually focalised, an optimal axial focus of the telescope can be found to maximize the number of detectors at the best focus and hence, maximize the resolution of the NIKA2 maps. This optimal z-focus setting is obtained by measuring the focus at the center of the arrays as described Sect. 2.3.2 and apply a focus shift, which is primary predicted using

¹http://www.iram.fr/wiki/nika2/index.php/April_19,_2017,_FXD,_KID_position_mapping_and_Field_distortion_for_Run9

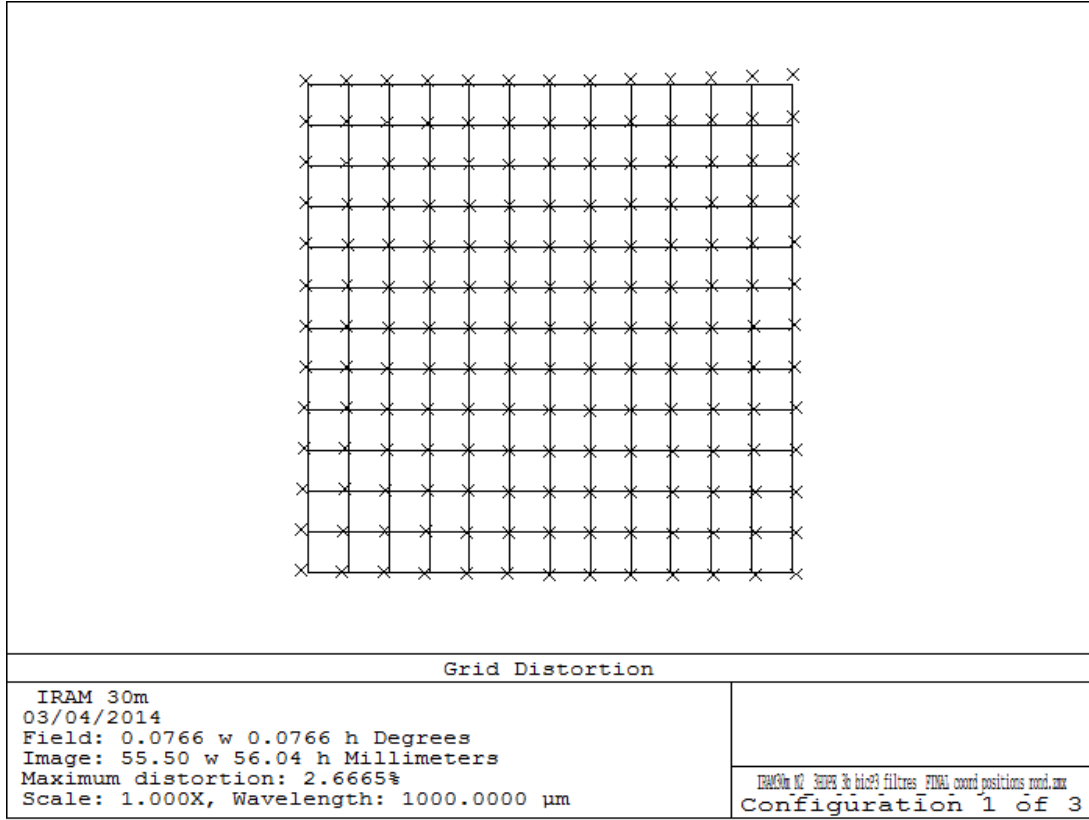


Figure 4.2: NIKA2 grid diagram simulated using ZEMAX. Crosses indicate the real coordinates on the Nasmyth image plan. **question à Samuel: pourquoi les dimensions indiquées sont environ 4.5 arcmin de côté (et pas 6.5)?**

Zemax simulation, and ultimately verified by measuring the focus surfaces as decribed here.

4.3.1 Method

We measure NIKA2 focal surfaces by means of a sequence of five defocused *beammaps* of bright point-like sources, typically Planets or bright quasars, for various settings of the telescope axial focus around the optimal focus z_{opt} . The z-focus is changed in step of 0.6 mm to probe a large focus range for measuring even the extreme variation of the focus surfaces, namely $z \in \{-1.2, -0.6, 0, 0.6, 1.2\} + z_{\text{opt}}$. Each *beammap* are analysed using the data reduction pipeline, as described in Sect. 2.2, and 4''-resolution individual maps per kid are projected. Therefore, a series of five cleaned maps at various focus is available for each detector, from which the best focus is estimated as described in Sect. 2.3.2. The ensemble of the relative focus estimate per KIDs with respect to the best focus at the center of the array constitutes the focus surface. An accurate estimate of the center focus is obtained as the weighted average focus estimate of the KIDs lying in a 30'' radius around the geometrical center of the array. This average does not induce any sizeable bias thanks to the flatness of the focus surface in the innermost regions. For robustness test, we consider three focus estimates: the two first ones are the same as discussed in Sect. 2.3.2 – namely i) \hat{z}_{fwhm} the focus that minimizes the geometrical FWHM and ii) \hat{z}_{peak}

Draft

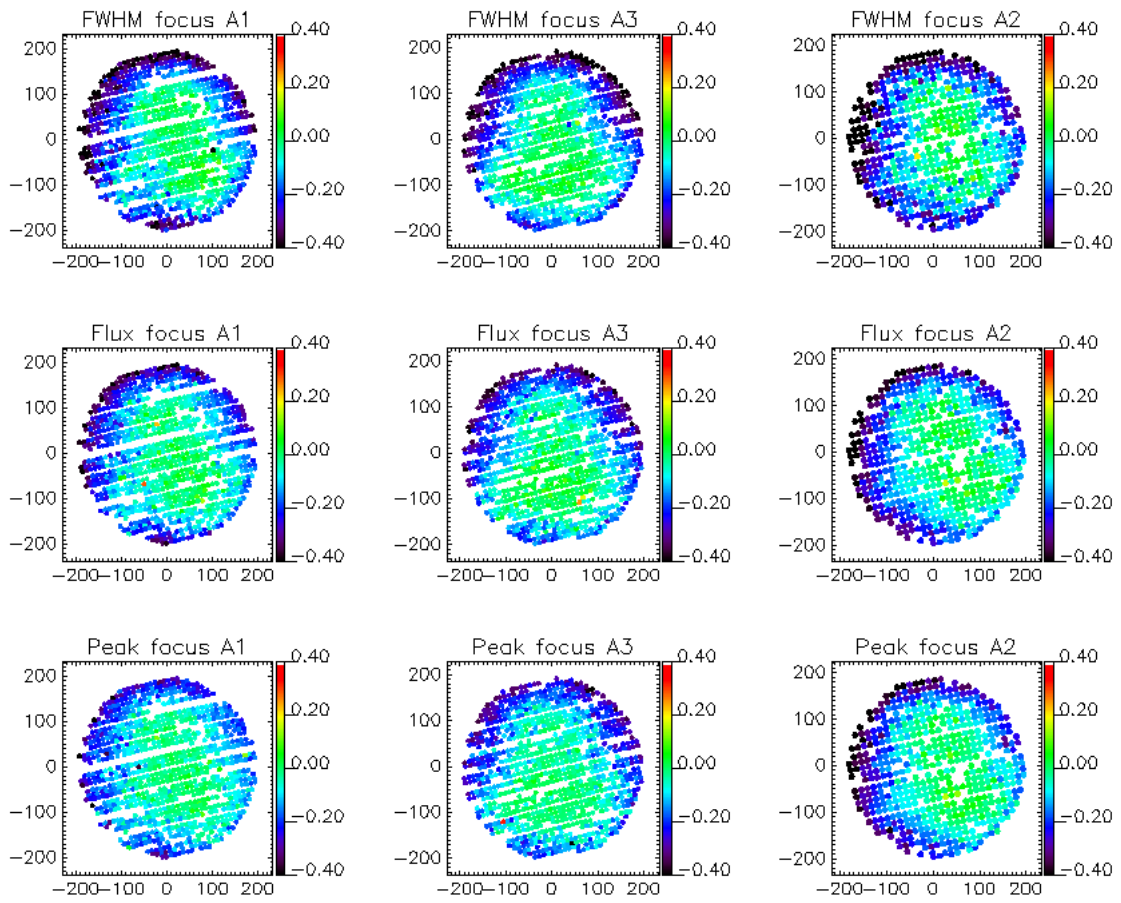


Figure 4.3: Focus surface of A1, A3 and A2 arrays from left to right. From top to bottom, the focus estimates rely on FWHM-minimization, amplitude-maximization of an elliptical Gaussian of fixed FWHMs and amplitude-maximization of an elliptical Gaussian.

the focus that maximizes the amplitude of the best-fitting elliptical Gaussian – whereas the third one is \hat{z}_{flux} the focus that maximizes the amplitude of the best-fitting elliptical Gaussian of fixed FWHM (at $12.5''$ at 260 GHz and $18.5''$ at 150 GHz). The comparison between the two amplitude-based estimators (\hat{z}_{peak} and \hat{z}_{flux}), will test the stability of the focus results against the exact choice of the beam fitting function. Since the ellipticity-based estimator \hat{z}_{ellip} is less sensitive to focus changes and yields larger uncertainties than the others, we do not use it for the focus surface reconstruction.

4.3.2 Data set

After the change of A1 lens and the improvement of internal optics alignment (hence in the final NIKA2 optical configuration) that is during the N2R8 two-day run, N2R9 and N2R10, nine defocused *beammap* sequences have been acquired, including incomplete sequences and sequences hindered by poor atmospheric conditions. We select sequences that i) comprises at least four scans, ii) have been observed at zenith opacity at 225 GHz (as indicated by the IRAM taumeter) below 0.5 and iii) have a maximal central focus drift between the starting time and the end of the sequence of 0.5 mm. These criteria preserve five sequences from which focus surfaces can be reconstructed. Namely, we consider the sequences 20170226s415–419, 20170419s133–137, 20170420s113–117, 20170421s160–164 and 20170424s123–127, which consist of observations of the bright quasar 3C84 and Neptune.

4.3.3 Results

For each detector k and each *beammap* sequence s , we obtain for the array a , a focus measurement $z_k^{a,s} \pm \sigma_k^{a,s}$, where $\sigma_k^{a,s}$ is the $1-\sigma$ error of the least-square polynomial fit. The focus surface measurements per array obtained from the five *beammap* sequences are combined using an inverse-variance weighting scheme to obtain the focus surface estimates

$$z_k^{(a)} = \left(\sigma_k^{(a)} \right)^2 \sum_s \frac{z_k^{a,s}}{\left(\sigma_k^{a,s} \right)^2}, \quad (4.2)$$

with uncertainties

$$\sigma_k^{(a)} = \left[\sum_s \frac{1}{\left(\sigma_k^{a,s} \right)^2} \right]^{-1/2}. \quad (4.3)$$

We present NIKA2 focus surfaces per array obtained as in Eq. 4.2 in Fig. 4.3. The three flavours of focus-estimators provide us with focus surfaces per array that are in good agreement with each others and that have a non-axisymmetrical flatten bowl shape consistent with expectations from optical simulation. The median defocus (that is the relative focus w.r.t. the center) across the detectors is about -0.1 mm for the three arrays. Maximal defocus values of about -0.6 mm are found for detectors located in the outer top and left regions of the FOV. Finally, a fraction comprised between 20 and 30% of the KIDs has a relative $z \leq -0.2$ mm.

In Sect. A.4, we further test the stability of the focus surfaces by comparing results from a series of *beammap* sequences acquired at various date and under various atmospheric conditions. We found the focus surfaces to be stable against observation dates and atmospheric conditions.

We primarily estimate the uncertainty of the focus surface measurements using the standard deviation between the three estimators $z_k^{(a)}|_{\text{fwhm}}$, $z_k^{(a)}|_{\text{peak}}$ and $z_k^{(a)}|_{\text{flux}}$. We found approximately homogeneous standard deviation surfaces per array, which have median values across the

FOV of about 0.03 mm. However, we cross-check this error estimate by forming the quadratic mean of the three inverse-variance error surfaces per array, which are defined in Eq. 4.3 and quoted $\sigma_k^{(a)}|_{\text{fwhm}}$, $\sigma_k^{(a)}|_{\text{peak}}$ and $\sigma_k^{(a)}|_{\text{flux}}$. This provides us with more optimistic error surfaces per array, which do not show any clear pattern across the FOV and which have a median value across the detectors of about 0.015 mm.

Draft

Chapter 5

Beam pattern

The NIKA2 beam pattern mainly depends on the IRAM 30 m telescope and NIKA2 full (external and internal) optical system characteristics, whereas the detectors themselves might have an impact at sub-dominant level (through e.g. time constants or correlated noises).

In this section, we characterize both the main beam, which is modeled as an elliptical Gaussian, and the full beam pattern including error beams up to angular scales of 10 arcmin.

5.1 Full beam pattern

5.1.1 Data sets

The characterization of the IRAM 30 m beam pattern observed through NIKA2 detectors is mainly based on observations of strong compact sources, such as planets including Uranus, Neptune and Mars, and bright quasars. We generally use *beammap* scans, which are described in Sect. 2.3.6. Most of our beam-related analysis are based on a set of 18 *beammap* scans acquired during the N2R8 and N2R9 commissioning campaigns and the N2R12 and N2R14 science pools. Namely, the set consists of the N2R8 '20170125s243' scan, the N2R9 '20170224s177', '20170226s415', '20170226s425' and '20170227s84' scans, the N2R12 '20171022s158', '20171023s101', '20171024s105', '20171024s106', '20171025s41', '20171025s42', '20171027s49', '20171028s310', '20171029s266', '20171030s268' and '20180117s92' and the N2R14 '20180117s92', '20180122s82' and '20180122s309' scans.

This set of *beammap* have been selected from all the available *beammap* at optimal focus using the baseline selection criteria, as given in Sect. 2.3.7.

5.1.2 Deep beam maps

We present the two-dimensional distribution of the beam in Fig. 5.1. We primarily use a map obtained from a combination of deep observations of strong point sources collected during NIKA2-*run8* and *run9*. Namely, we use 'beammap' OTF scans of Uranus (scan id '20170125s223' and '20170125s243'), Neptune ('20170224s177') and the bright quasar 3C84 ('20170226s415'). However, we checked the stability of our results on single scan maps, combinations of scans for a single source, and combinations of shallower scans but spanning a large range of scanning direction. The data processing includes a mitigation of the correlated noise, which mainly originates from the atmosphere. We primarily use a subtraction of a common mode estimated

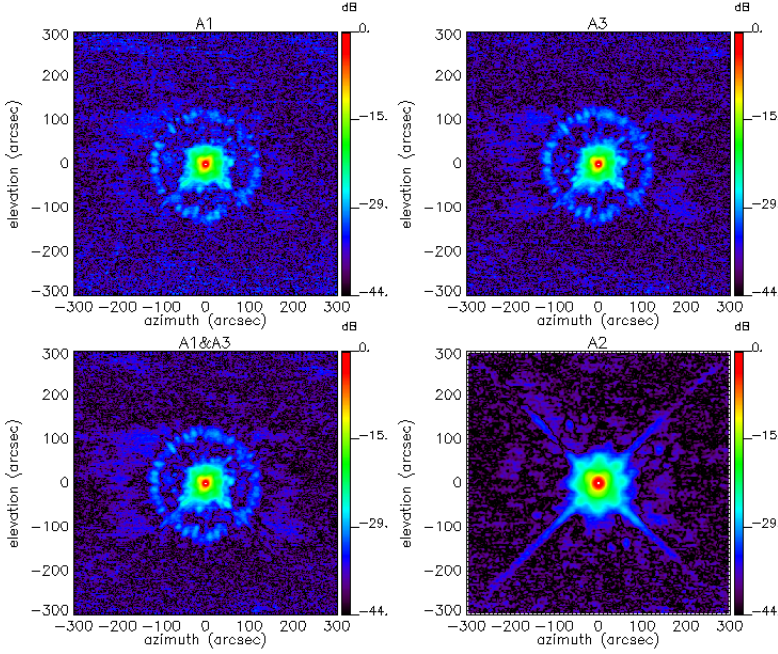


Figure 5.1: From upper left to lower right, beam maps of array 1 (labeled 'A1'), array 3 ('A3'), the combination of the 1.15mm arrays ('A1&A3') and the 2mm array ('A2') are shown in decibel. These maps, which consist of normalized combination of four long OTF scans of bright point sources, are in celestial coordinates and cover a sky area which extend over 10 arcmin.

The deep NIKA2 beam maps reveal some noticeable features, which are shown in Fig. 5.2 and which include:

- (1) four symmetrical spokes of the error beam as shown by yellow arrows in the A2 panel, which are expected from *Zemax* simulations;
- (2) shallow spikes of unknown origin, which are circled by pink ellipses. The multiple images on the combined deep beam map indicate a rotation of these spikes with the observing elevation, which in turn point to diffraction related issue or a ghost image that are formed inside the cryostat;
- (3) other spikes of unknown origin, as pointed with the yellow arrows in the A3 panel. The ones that are close to the vertical and horizontal radii are reproduced by '*Zemax*' simulation but with a shallower, whereas the ones in the diagonal directions may be due to external calibrator installed close to the secondary mirror.

To gain a first impression of the structure of the Iram 30-m beam as seen with NIKA2, we use radial cuts to evidence the relative level of the main beam, the first error beam and other features seen in the 2D beam pattern using radial cuts. NIKA2 full beam is shown in the left panels of Fig. 5.3 by means of two orthogonal cuts through Uranus from a high quality map

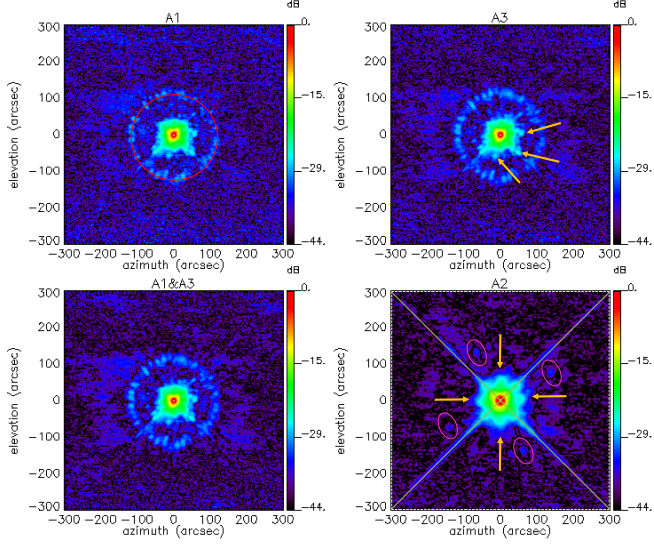


Figure 5.2: Red circle: diffraction ring seen in 1-mm maps (the spokes are presumably caused by radial and azimuthal panel buckling (cf. Fig.4 in Greve et al. 2010)); Perpendicular green lines: diffraction pattern caused by quadrupod secondary support structure (prominently seen in 2mm maps); Yellow arrows in the upper right pannel: pattern of 3 spikes seen in 1mm maps of unknown origin; Yellow arrows in the lower right pannel: four symmetrical spokes of the first errorbeam; Pink ellipses: 4 spikes seen in 2mm maps.

obtained on 2017 January 25th in excellent observing conditions (low opacity $\tau_{225} = 0.08$ and elevation 46°).

A model made of three Gaussians centered on the source peak was best fit *by hand* to these cuts. We observe that the main beam starts to depart from the first Gaussian at the level of about -12dB for the three arrays. We note that for the instrument EMIR on the radiotelescope, this departure is about -20dB (Kramer, Penalver and Greve 2013). However, this discrepancy between a feedhorn-based experiment and a bare pixels one is expected since the main effect of the feedhorns is to lower the side lobes of the Airy diffraction pattern. The precise characterization of the full beam structure is discussed in Sect. 5.1.3.

5.1.3 Beam profile

The beam profile $B(r)$ is the radial brightness profile normalized so that $B(0) = 1$, where r is the radius from the beam center. Although the profile cannot represent the sub-dominant non-axisymmetrical extended features, which are seen in the beam pattern and discussed in Sect. 5.1.2 (telescope arms, spikes), it provides us with a useful representation of the internal and central parts of the beam (about up to $100''$). We determine a beam profile from a beam map in centering to the fitted value of the main beam center and in forming the weighted average of the pixels equidistant to the center.

We model the beam profile $B(r)$ as a three-Gaussian function defined as:

$$B(r) = \sum_i \mathcal{A}_i G_i(r) + \mathcal{B}_0, \quad (5.1)$$

Draft

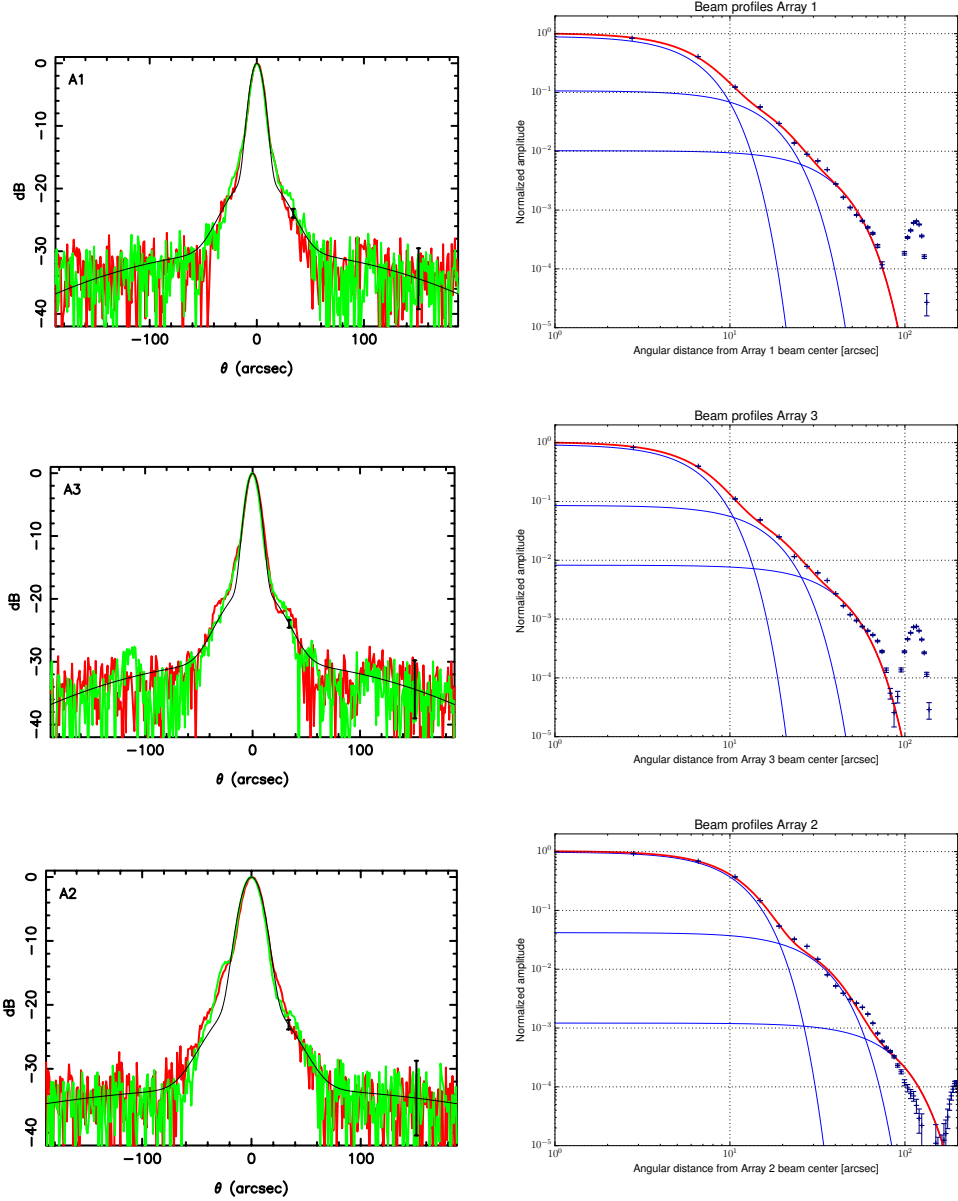


Figure 5.3: *Left column:* Two orthogonal cuts through the beam are shown in red and green and a best fit model made of three Gaussians is superimposed in black. These cuts were obtained from the high quality map of Uranus on 2017 January 25th. The main beam starts to depart from the first Gaussian at -12dB. *Right column:* Example of beam radial profile estimated on the same map of Uranus. The Best-fitting curve is show in red using a three Gaussian model.

where \mathcal{A}_i the amplitude of the Gaussian i for $i \in 1, 2, 3$ and \mathcal{B}_0 a pedestal level accounting for the residual noise level in the map. An example of the beam profile from a beam map acquired during N2R8 (scan ID: 20170125s223), as well as the best-fit 3-Gaussian model, is shown in the right panels of Fig. 5.3.

We checked the stability of the beam against various observing conditions (source intensity,

weather condition, focus optimisation) by comparing the beam profiles of the *beammap* set, as described in Sect. 5.1.1. The 18 beam profiles and their difference w.r.t. the median beam profile are shown in Fig. 5.4. The variations of the normalised radial profiles are below 5% at both wavelengths.

We further fit the three-Gaussian model of Eq. 5.1 to each profile and gather the average best-fitting amplitudes with respect to the peak amplitude and FWHM in Table 5.1. The errors are evaluated as the standard deviation of the best-fitting parameter values of the 18 *beammap* scans, and thus do not account for the correlation between parameters. These values are given to gain insight of the axisymmetrical pattern of the beam, but are not further used for the calibration.

Arrays	3-Gaussian profile parameters					
	Amp 1	Amp 2	Amp 3	FWHM 1	FWHM 2	FWHM 3
A1	0.89 ± 0.01	0.08 ± 0.02	$5 \times 10^{-3} \pm 2 \times 10^{-3}$	11.0 ± 0.2	29 ± 2	65 ± 15
A3	0.90 ± 0.01	0.07 ± 0.01	$4 \times 10^{-3} \pm 2 \times 10^{-3}$	11.0 ± 0.2	30 ± 3	72 ± 23
1mm	0.90 ± 0.01	0.07 ± 0.01	$4 \times 10^{-3} \pm 2 \times 10^{-3}$	11.0 ± 0.2	29 ± 2	70 ± 15
2mm	0.96 ± 0.01	0.3 ± 0.3	$1 \times 10^{-3} \pm 0.3$	17.5 ± 0.1	63 ± 10	65 ± 12

Table 5.1: Average 3-Gaussian beam profile parameters

Draft

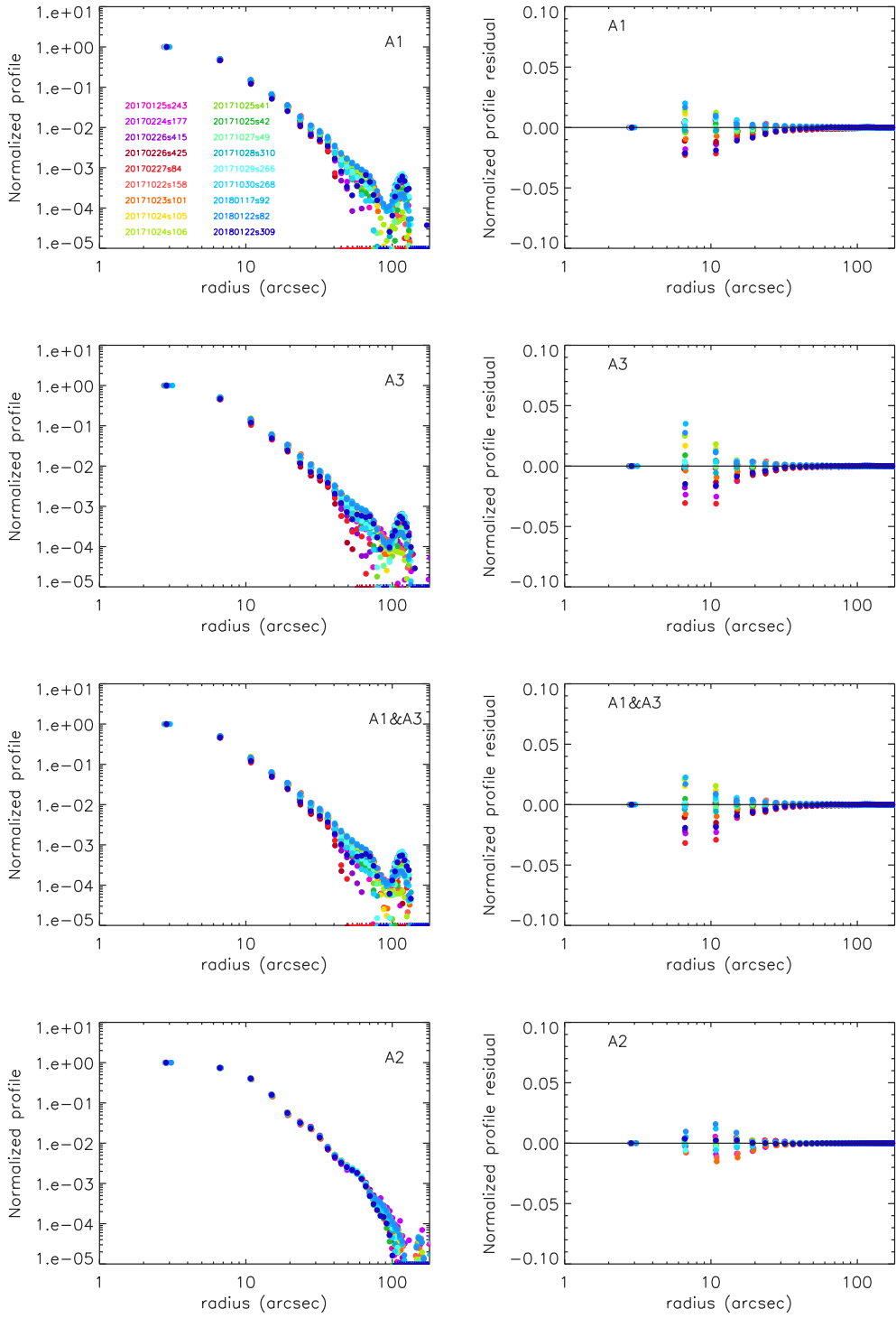


Figure 5.4: Beam radial profiles as a function of the radius from the peak for a series of 18 *beammap* scans acquired during the N2R8 and N2R9 calibration campaigns and during the N2R12 and N2R14 science pools. Left column plots: beam profiles normalised to the maximum value; Right column plots: difference w.r.t. the median normalised profile. The radial profile shapes are stable at better than 5% against observing conditions.

5.2 Main beam

We define NIKA2 main beam as the principal Gaussian (of the smaller FWHM) that encloses most of the measured source flux. The best-fitting value of the first Gaussian function of the three-Gaussian model, as discussed in Sect. 5.1.3, provides us with a first estimate of the main beam. However, this estimate could be biased toward the lower FWHM values due to degeneracies between the three-Gaussian model parameters. To ensure obtaining robust main beam FWHM estimates, we devise two alternative dedicated methods, which both resort to masking the side lobes: i) Gaussian fits of the beam profile to benefit from the signal-to-noise ratio increase after azimuthally averaging the signal, ii) Elliptical Gaussian fits of the beam map for a better 2D modeling. Cross-checking the outputs from these complementary methods is an important robustness test of our results.

We also consider different data sets acquired during the N2R9 commissioning campaign and the N2R12 and N2R14 science pools: i) a series of $8' \times 5'$ OTF scans of primary and secondary calibrators, as described in Sect. 5.2.2, ii) *beammap* scans of bright sources, as discussed in Sect. 5.2.2.

5.2.1 Sidelobe-masked 1D method

The brightness radial profiles of a primary calibrator (Uranus or Neptune) are first computed from their maps with a fine resolution ($1''$ pixel). Then a single Gaussian is fit to each profile after masking data points at radial distances comprised between $0.65 \times \text{FWHM}$ and $80''$, so that the error beam (side lobes) does not bias the fit. In this approach, the data points at radial distance beyond $80''$ provide the base level of the Gaussian fit. In practice, maps $600'' \times 600''$ in size were made but only the inner part within a radius of $180''$ with uniform rms was used to compute the profile. The best-fitting FWHM of the Gaussian model yields the main beam FWHM for each array, as reported in Table 5.2.

All *beammap* and shallower OTF scans of Uranus and Neptune in the N2R9, N2R12 and N2R14 observation campaigns were used to determine the means and standard deviations of the main beam fwhms for the three arrays in Table 5.2.

5.2.2 Sidelobe-masked 2D method

Method description

NIKA2 main beam two-dimensionnal distribution is modeled using an elliptical Gaussian. We characterize NIKA2 resolution by forming the *FWHM*, defined as

$$\text{FWHM} = 2\sqrt{2 \ln 2} \sqrt{\sigma_x \sigma_y}, \quad (5.2)$$

where σ_x and σ_y are the Gaussian standard deviation along minor and major axis. To avoid the side lobes contamination, we use masked versions of the beam map. The sidelobe mask consists in cutting an annulus of inner radius r_{in} and outer radius r_{out} centered on the beam maximum. Whereas r_{out} is conservatively set to be $100''$, r_{in} is let free to vary around a central value about $8''$ for A1 and A3 and about $12''$ for A2 to provide the best 2D Gaussian fit.

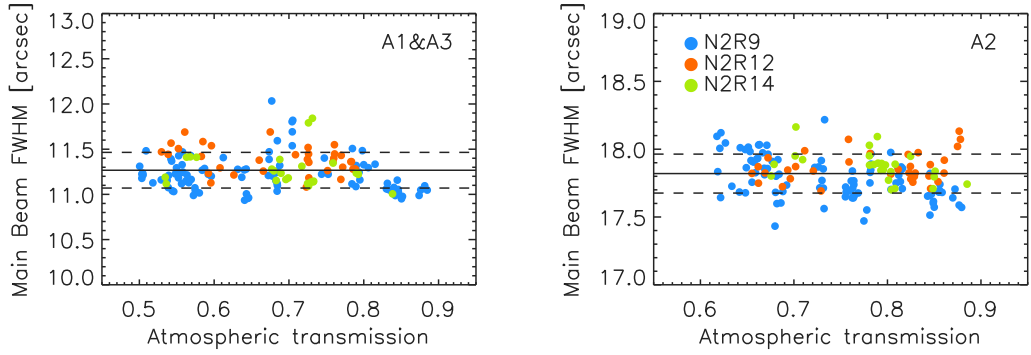


Figure 5.5: Main beam FWHM estimates for the 1 mm (left) and 2 mm (right) channels are shown as a function of the atmospheric transmission using bright source scans acquired during N2R9, N2R12 and N2R14.

OTF scan based results

We select scans of moderately bright to very bright point sources by thresholding the flux density estimates at 1 Jy at both wavelengths. Slightly extended sources, such as Mars, NGC7027 and CRL2688 are discarded. After the baseline selection cuts, as described in Sect. 2.3.7, the data set comprises 163 scans towards the giant planets Uranus and Neptune, the secondary calibrator MWC349 and the quasars 3C84, 3C273, 3C345 and 3C454 (aka 2251+158). The data are reduced using the pipeline described in Sect. 2.2 and projected onto 2'' resolution maps. The FWHM of the main beam is estimated following the sidelobe-masked 2D method, as described in Sect. 5.2.2. For Uranus, the FWHM estimates are further corrected for the beam broadening due to the extension of the apparent disc. At the IRAM 30 m latitude, Uranus disc diameter varies from 3.3'' to 3.7''. This induces a broadening of the Gaussian main beam of 0.19 ± 0.03 arcsec at 1-mm and 0.12 ± 0.02 arcsec at 2-mm. Uranus FWHM estimates are corrected for the average beam widening values.

Figure 5.5 shows the main beam FWHM estimates as a function of the atmospheric transmission, which is modeled as $\exp(-\tau \cdot x)$, where τ is the zenith opacity estimate and x the airmass, which is evaluated as the cosecant of the observing elevation. The FWHM estimates using data of the three campaigns are in agreement within rms errors. Moreover, the main beam FWHM is stable against the atmospheric condition at both wavelengths. Slightly lower values than average (about 11'') are observed in the best atmospheric conditions at 1 mm providing us with a lower limit in the absence of correlated atmospheric noise residuals. We note three scans acquired during N2R12 with larger FWHM than average at 2 mm although the atmospheric transmission was excellent: this is likely an effect of the anomalous refraction, which impacted a lot of scans during the N2R12 campaign.

The distributions of the best-fitting FWHM values of array 1, 3, the combination of arrays 1&3 and array 2 using the OTF scans from the three observation campaigns are shown in Fig. 5.6. Nine scans with outlier r_{in} values have been discarded. We checked a posteriori that r_{in} distributes as 10 ± 1 arcsec at 1 mm and 11 ± 1 arcsec at 2 mm. The average FWHM estimates and the rms errors are reported in Table 5.2.

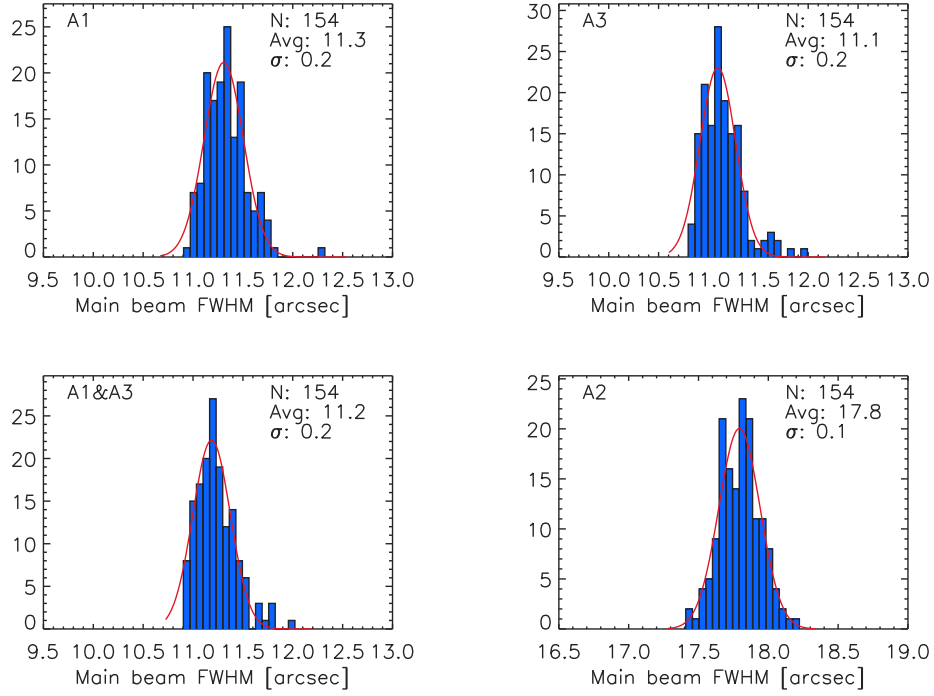


Figure 5.6: Distribution of the FWHM estimates for Array 1, 3, the combination of Array 1&3 and Array 2, including bright source scans from the three campaigns.

Beammap scan based results

We select a sub-set of the *beammap* scan selection described in Sect. 5.1.1 by discarding scans of Mars. The 12 remaining *beammap* scans are analysed using the data reduction pipeline of Sect. 2.2 and projected onto maps with a resolution of $1''$ and an angular size of $10'$. The main beam FWHM is estimated using the sidelobe-masked 2D method, as described in Sect. 5.2.2. Sidelobe masks are defined by a fixed external radius r_{out} of $100''$ and a fixed internal radius r_{in} of $8.5''$ at 1 mm and $13.5''$ at 2 mm. We checked that we obtain compatible results when r_{in} is let to freely varies from $8'$ to $10'$ at 1 mm and from $10'$ to $14'$ at 2 mm. The fixed r_{in} values correspond to the average best-fitting r_{in} of the free- r_{in} analysis. The main beam FWHM estimates using the sidelobe-masked 2D method on the *beammap* scans are gathered in Table 5.2.

5.2.3 Comparison of the main beam FWHM estimates

We have derived the main beam FWHM for the three arrays and the 1 mm array combination using three methods and three data sets. Namely, our main beam FWHM estimates consist of i) the median FWHM of the first (lowest-FWHM) Gaussian function within the three-Gaussian model fitted from the 12 *beammap* scan sub-set described in Sect. 5.2.2, ii) the average FWHM using the sidelobe-masked 1D method on a series of *beammap* and $5' \times 8'$ OTF scans of Uranus and Neptune, the sidelobe-masked 2D method average FWHM from iii) a series of $5' \times 8'$ OTF scans of bright point sources and iv) from the 12 *beammap* scan sub-set. The results of this analysis are gathered in Table 5.2, including error bars evaluated as the rms dispersion of single-scan based

FWHM estimates.

All the tests based on sidelobe-masked methods yield FWHM estimates in agreement within error bars, whereas the test resorting to the three-Gaussian model yields slightly smaller FWHM for all arrays. The latter provides us with lower limits for the main beam FWHM. The error bars are the most robustly derived from the dispersion of the best-fitting FWHM over the set of 154 OTF scans, whereas rms errors that are estimated from smaller scan sets are likely to be underestimated. The combined results are obtained from an error-weighted average of the four FWHM estimates for each array. The 12 *beammap* scan based rms errors were replaced by the 154 OTF scan based rms errors beforehand. The combined FWHM estimates are given in Table 5.2.

Table 5.2: FWHM of the NIKA2 main beam in arcsec.

Method	Dataset	Array or array combination			
		A1	A3	A1 & A3	A2
Three-Gaussian model G1 ^a	<i>beammap</i>	10.8 ± 0.1	10.8 ± 0.1	10.8 ± 0.1	17.4 ± 0.1
Sidelobe-masked 1D method	mixed	11.3 ± 0.4	11.2 ± 0.4	11.2 ± 0.3	17.4 ± 0.2
Sidelobe-masked 2D method	5x8 OTF	11.3 ± 0.2	11.1 ± 0.2	11.2 ± 0.2	17.8 ± 0.1
	<i>beammap</i>	11.2 ± 0.1	11.1 ± 0.1	11.2 ± 0.1	17.6 ± 0.1
Combined		11.1 ± 0.2	11.0 ± 0.2	11.1 ± 0.2	17.6 ± 0.1

^(a) Median FWHM of the first (lowest-FWHM) Gaussian function within the Three-Gaussian model fitted from 12 *beammap* scans

5.2.4 FWHM distribution across the FoV

Figure 5.7 shows the distribution of the main beam FWHMs of the arrays A1, A3 and A2 using a *beammap* scan of Neptune acquired during the April 2017 commissioning campaign and for average weather conditions (scan ID: 20170424s123). We also show in red the best Gaussian fit to histogram data. We find an average main beam FWHM of $10.9''$ at 260 GHz and $17.5''$ at 150 GHz in agreement with the main beam estimates gathered in Table 5.2. The observed dispersion of about $0.6''$ is expected from the optics design and its associated field distortions across the 6.5 arc-minutes FoV, as discussed in Sect. 4.2. This quantifies the impact of the non-constant focus across the FoV, which is characterised in Sect. 4.3, on the individual detector main beams.

5.3 Beam efficiency

Building upon the description of the full-beam pattern in Sect. 5.1 and the main beam in Sect. 5.2, we derive the beam efficiency for each array, which is defined as the ratio of the solid angle sustained by the main beam to the total beam solid angle. The total solid angle

$$\Omega_{\text{tot}}(A_i, r_{\text{max}}) = \int_0^{r_{\text{max}}} B_{A_i}(r) 2\pi r dr \quad (5.3)$$

is estimated from the beam profile $B_{A_i}(r)$ of the array A_i at $r_{\text{max}} = 180''$ and the main beam solid angle is evaluated as the volume of the Gaussian main beam as $\Omega_{\text{mb}} = 2\pi \sigma_{\text{mb}}^2$.

The choice of the maximum radius is entailed both by the depth of the *beammap* scans and the filtering due to the data processing. However, heterodyne observations of the lunar edge

Draft

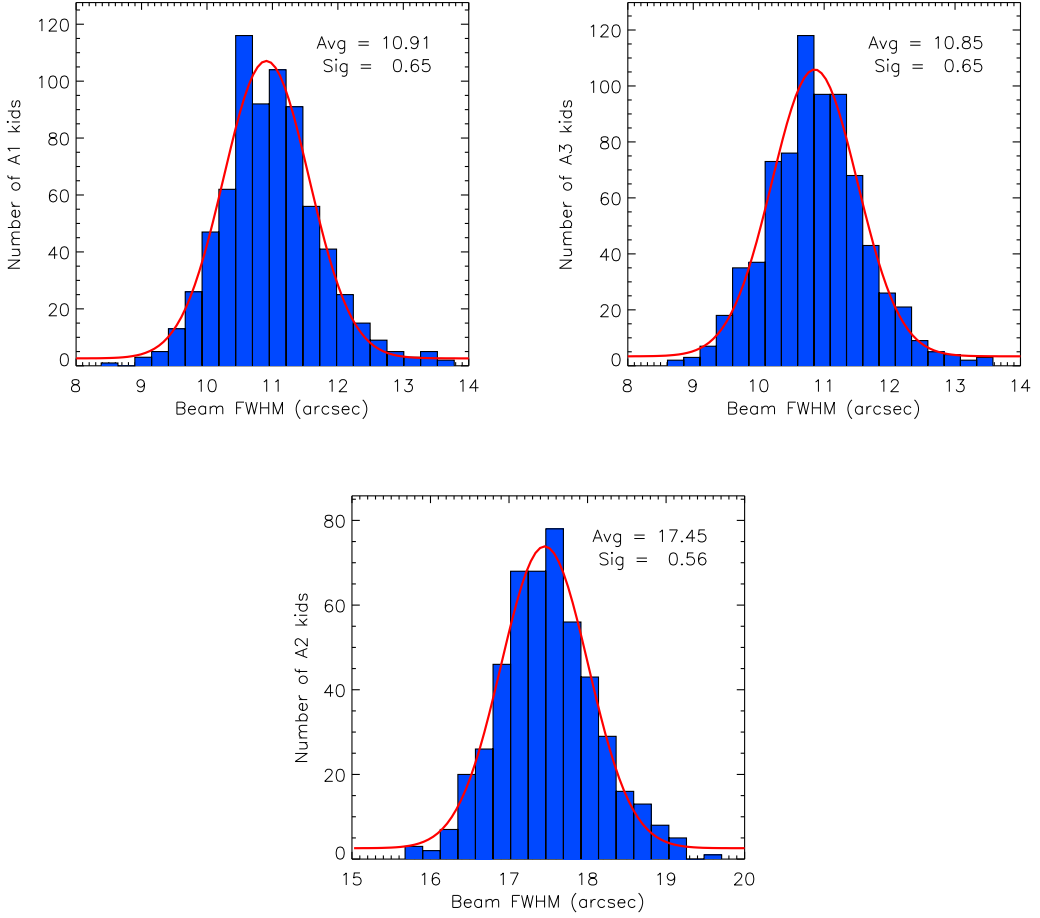


Figure 5.7: Main beam FWHM distribution of all valid KID detectors of arrays A1, A3, and A2. The main beam FWHM is the geometrical combination of the two-orthogonal FWHM estimates obtained from an elliptical Gaussian fit on side-lobe masked individual maps per KID using a *beammap* scan of N2R9 (scan ID: 20170424s123). The red curves show a Gaussian fit to the histogram data.

and of the forward beam efficiency derived from skydips show that a non-negligible fraction of the full beam is received from beyond a radius of $180''$. This fraction is not considered here.

A large set of *beammap* scans of Uranus and Neptune acquired during the N2R9, N2R12 and N2R14 campaigns have been used to evaluate Ω_{tot} from the measured beam profiles up to $r_{\text{max}} = 180''$ and Ω_{mb} derived with the main beam FWHM estimates using the sidelobe-masked 1D method. The result is given in Table 6.8.

This 75 *beammap* scan set, as well as the 12 *beammap* scan sub-set, which is defined in Sect. 5.2.2, are further used to measure the beam efficiencies. We compare the results based on various estimates of Ω_{tot} and Ω_{mb} :

- *Method 1* relies on the best-fitting parameters of the three-Gaussian model of the full beam to derive the two solid angles. The main beam solid angle thus corresponds to the volume enclosed by the first Gaussian;

Table 5.3: Solid angle of true beam based on Uranus and Neptune observations

run	Nber of scans	Ω_{tot} (arcsec 2)			$\Omega_{\text{tot}}/\Omega_{\text{gauss}}$		
		A1	A2	A3	A1	A2	A3
N2R9	27	265 \pm 23	466 \pm 17	252 \pm 23	1.80 \pm 0.12	1.35 \pm 0.05	1.74 \pm 0.13
N2R12	20	229 \pm 11	437 \pm 9	221 \pm 10	1.71 \pm 0.06	1.30 \pm 0.02	1.68 \pm 0.06
N2R14	28	251 \pm 16	457 \pm 15	245 \pm 18	1.73 \pm 0.08	1.32 \pm 0.03	1.72 \pm 0.08
mean		248	453	239	1.74	1.32	1.71

- *Method 2* consists in using the measured beam profile to estimate Ω_{tot} , while Ω_{mb} is derived with the main beam Gaussian FWHM fit using the sidelobe-masked 1D method, as discussed in Sect. 5.2.1;
- *Method 3* is similar to method 2 but the main beam FWHM is fitted using the sidelobe-masked 2D method, as in Sect. 5.2.2.

The beam efficiency estimates using the three methods are gathered in Table 5.4: central values and error bars are evaluated as the median and the rms error of the estimates on individual *beammaps* respectively. The rms error estimates for *method 2*, which are based on 75 *beammap* scans, provide us with a robust evaluation of the beam efficiency uncertainties. By contrast, error estimates for *methods 1&3* rely on 12 scans and are thus less robust. We combined the results of three methods using an error-weighted average. *Method 2* rms errors are conservatively used as a lower limit of the error estimates for all methods. The combined beam efficiency are given in Table 5.4.

Table 5.4: Main beam efficiency in %

Method	Array or array combination			
	A1	A3	A1 & A3	A2
method 1 ^a	54 \pm 3	54 \pm 4	53 \pm 3	74 \pm 4
method 2 ^b	55 \pm 3	56 \pm 3	55 \pm 3	76 \pm 2
method 3 ^c	59 \pm 7	58 \pm 4	59 \pm 4	80 \pm 1
combined	55 \pm 3	56 \pm 3	55 \pm 3	77 \pm 2

(a) based on the three-Gaussian model best-fitting parameters

(b) based on the sidelobe-masked 1D main beam FWHM

(c) based on the sidelobe-masked 2D main beam FWHM

As a stability check of the beam efficiency, the detailed beam efficiency estimates using *method 2*, as well as the level of the error beam, for each observation campaigns are given in Table 5.5. The level of the error beam is given relative to the main beam peak (we recall that -12dB as found is 6%). We find stable beam efficiencies using observations acquired one year apart.

Table 5.5: Main beam efficiency and level of error beam

run	Nber of scans	Main beam efficiency (%)			Error beam level (dB)		
		A1	A2	A3	A1	A2	A3
N2R9	27	54.1 ± 3.2	74.7 ± 2.9	55.9 ± 3.7	-11.5 ± 0.8	-14.9 ± 0.6	-12.0 ± 0.6
N2R12	20	55.7 ± 2.0	77.4 ± 1.0	57.1 ± 2.0	-13.4 ± 0.3	-16.1 ± 0.3	-13.8 ± 0.3
N2R14	28	55.0 ± 2.7	76.0 ± 1.8	56.1 ± 2.6	-12.5 ± 0.6	-15.3 ± 0.6	-12.7 ± 0.8

Chapter 6

Calibration

6.1 Photometric System

The calibration of the NIKA2 instrument in its final configuration of January 24th 2017 is studied in this section in using Uranus as the main primary calibrator. Neptune and Mars are also considered as valuable alternatives to calibrate when Uranus is not visible.

	1 mm	2 mm
Reference frequency ν_0	260 GHz	150 GHz
Reference FWHM	12.5 "	18.5 "

Table 6.1: NIKA2 reference frequencies and FWHM

6.2 Main photometric equation

Starting from the general equation for the response of a detector to an astronomical source, we derive the main photometric equation as detailed in Sect. A.3. The map (in units of the KID resonance frequency shift or Hz) of a source using a single KID k after correction of the atmospheric absorption is

$$R^k(\theta, \phi) \simeq G_k A_p \Omega_p \int_0^{+\infty} I(\nu) T(\nu) T_{atm}(\nu) B_k(\nu_0, \theta \times \frac{\nu}{\nu_0}, \phi) d\nu \quad (6.1)$$

where we have considered a source observed at airmass x under mm_{H_2O} of precipitable water, with specific intensity I_ν (in units of $W/m^2/sr/Hz$) in the direction θ, ϕ , where θ is the off-axis distance and ϕ the position angle, illuminating the KID k . The dependance on elevation and opacity is corrected, as discussed in section 3, so that Eq. 6.1 is the KID response outside of the atmosphere (in terms of airmass, but not in terms of transmission).

The integral in the right-hand part of Eq. 6.1 gives the total power (units of W) falling on the KID, where the factors are:

- $T(\nu)$, NIKA2 bandpasses, which are measured and corrected for the Rayleigh-Jeans term as discussed in Sect. 2.1.2
- $T_{atm}(\nu)$, the transmission of the atmosphere at zenith.

- $B_k(\theta, \phi, \nu)$, the fraction of source signal illuminating the KID, that is the beam function. It has been parametrized as a function of the effective frequency as defined in Eq 2.1 of Sect. 2.1.2, considering that its frequency dependency is only due to the diffraction law, hence a variation as $1/\nu$ from a reference frequency ν_0 .

The gain of the KID k G_k (units of $\text{Hz} \cdot \text{W}^{-1}$) converts the total power in W to the frequency shift in Hz. A_p is the area of the entrance pupil (*i.e.* the dish collecting area), and Ω_p is the solid angle of the source seen from the entrance pupil.

Because both A_p and Ω_p are not known with good accuracy, it is not possible to compute all the terms of Eq. 6.1 from first principles, and a practical way of calibrating the system must be used: it is done by observing a primary calibrator.

6.2.1 Calibrator map in the reference system

A primary calibrator is a source whose flux density (or spectral irradiance) is known. For NIKA2, we use two planets as primary calibrators, Uranus and Neptune.

The specific intensity $I_c(\nu)$ of the calibrator is:

$$I_c(\nu) = \frac{S_c(\nu)}{\Omega_p} = \frac{S_c(\nu_0)}{\Omega_p} f\left(\frac{\nu}{\nu_0}\right) \quad (6.2)$$

where $S_c(\nu)$ is the flux density of the calibrator (units of $\text{W/m}^2/\text{Hz}$ or Jy). We parametrize the source flux density as a function of a reference frequency ν_0 that we choose arbitrarily to be: $\nu_0 = 150 \text{ GHz}$ for the 2mm array and $\nu_0 = 260 \text{ GHz}$ for both 1mm arrays.

Ingesting Eq. 6.2 in the main photometric equation (Eq. 6.1), the map (in units of Hz) of a calibrator observed with the KID k is:

$$R_c^k(\theta, \phi) = G_k A_p S_c(\nu_0) \int_0^{+\infty} f\left(\frac{\nu}{\nu_0}\right) B_k(\nu_0, \theta \times \frac{\nu}{\nu_0}, \phi) T(\nu) T_{atm}(\nu) d\nu \quad (6.3)$$

This observed map is modelled with a fixed-width Gaussian as

$$R_c(\theta, \phi) = \frac{A_c}{2\pi\sigma_0^2} e^{-\frac{\theta^2}{2\sigma_0^2}}. \quad (6.4)$$

The reference FWHM, labelled FWHM_0 , which we recall, is related to σ_0 by $2\sqrt{2\ln 2}\sigma_0 = \text{FWHM}_0$, are $12.5''$ for the 1mm arrays and $18.5''$ for the 2mm array, as defined in Table 6.1. These values have been chosen sizably larger than the main beam values, as reported in Sect. 5, to account for a fraction of the signal smeared in the error beam.

We form an estimator of the FWHM_0 Gaussian amplitude:

$$\hat{A}_c = 2 \int \int R_c(\theta, \phi) e^{-\frac{\theta^2}{2\sigma_0^2}} \sin \theta d\theta d\phi \quad (6.5)$$

But we also know that the integral of the observed map should give the power emitted by the source. Therefore, we form the map:

$$M_c(\theta, \phi) = R_c(\theta, \phi) S_c(\nu_0) / \hat{A}_c \quad (6.6)$$

where $S_c(\nu_0)$ is the flux density of the calibrator at a reference frequency ν_0 given in Table 6.1.

This map has units of Jy. By construction, integrating over the map we have:

$$\int \int M_c(\theta, \phi) \sin \theta d\theta d\phi = S_c(\nu_0). \quad (6.7)$$

6.2.2 Calibration in FWHM₀ beam

Similarly, a point source with flux density $S_s(\nu)$ will generate a response at position (θ, ϕ)

$$R_s^k(\theta, \phi) = G_k A_p \int_0^{+\infty} S_s(\nu) B_k(\nu_0, \theta \times \frac{\nu}{\nu_0}, \phi) T(\nu) T_{atm}(\nu) d\nu \quad (6.8)$$

Note here that the effective frequency for the beam is not necessarily the same as the one for the primary calibrator, as it depends on the source spectrum.

We fit the amplitude of a Gaussian of FWHM₀ width \hat{A}_s . The flux density estimate for the source is then:

$$\hat{S}(\nu_0) = \frac{S_c(\nu_0)}{A_c} \times \hat{A}_s \quad (6.9)$$

In other words, the flux estimate is the flux that should have the calibrator in order to generate a response that would be fitted with a FWHM₀ Gaussian of the same amplitude as the source.

Let us form the map:

$$M_s(\theta, \phi) = \frac{S_c(\nu_0)}{A_c} R_s(\theta, \phi) \quad (6.10)$$

The map $M_s(\theta, \phi)$ is said to be calibrated in Jy / FWHM₀ beam. The factor $S_c(\nu_0)/A_c$ is referred to as the absolute calibration factor.

In the case of a single point source in M , fitting a Gaussian of fixed width, we have:

$$\int \int M_s(\theta, \phi) \sin \theta d\theta d\phi = \hat{A}_s S_c(\nu_0) / A_c = \hat{S}(\nu_0) \quad (6.11)$$

Note that the flux density estimate $\hat{S}(\nu_0)$ is *not* the flux of the source at the reference frequency. In order to find the flux of the source at the reference frequency, a color correction has to be applied

$$S_s(\nu_0) = \hat{S}(\nu_0) C_s \quad (6.12)$$

6.2.3 Color Correction

The color correction C_s is derived in Sect. A.3.5. Neglecting the effect of the atmosphere on NIKA2 transmission, we compute the color correction factor for target sources of spectral indices α_S that are different from Uranus using

$$C_s = \frac{\int_0^{+\infty} (\nu/\nu_0)^{1.6} T_\nu d\nu}{\int_0^{+\infty} (\nu/\nu_0)^{\alpha_S} T_\nu d\nu}. \quad (6.13)$$

Color correction factors for eight values of α_S , and in particular for $\alpha_S = 0.6$ which is the spectral indice of MWC349, are given in Table 6.2.

6.3 Reference flux densities of the primary calibrators

The two main calibrators of NIKA2 are the giant planets Uranus and Neptune. Mars can also be used as primary calibrator, but care must be taken to use a flux corresponding to the date of the observations.

Table 6.2: Color correction factor for a target source $S \propto \nu^{\alpha_S}$

Array	α_S							
	-2	-1	0	+0.6	+1	+2	+3	+4
A1	0.876	0.916	0.951	0.969	0.981	1.005	1.024	1.037
A2	0.945	0.972	0.990	0.996	0.998	0.997	0.986	0.966
A3	0.907	0.940	0.967	0.980	0.987	1.001	1.009	1.011

Note : Uranus/Moreno model used for Uranus in this Table.

6.3.1 Uranus and Neptune

For the flux densities of the giant planets, we use the ESA model from [13]: Version 5 for Neptune and Version 4 for Uranus. Both models provide the planet brightness temperature in the Rayleigh-Jeans approximation as a function of the frequency. The resulting flux is therefore:

$$S_\nu = \Omega \times \frac{2\nu^2 k T_{RJ}}{c^2} \quad (6.14)$$

where Ω is the solid angle of the planet on the sky. Following Bendo et al. (2013) and correcting their equation 12 we have:

$$\Omega = \pi \frac{r_e r_{p-a}}{D^2} \quad (6.15)$$

where r_e is the equatorial radius of the planet and r_{p-a} is its apparent polar radius, and D the distance to the planet. r_{p-a} can be computed from the sub-observer latitude ϕ (e.g. the latitude of the 30-m telescope as seen from the planet in the planet equatorial reference frame) and r_p the polar radius of the planet as:

$$r_{p-a} = \sqrt{r_p^2 \cos^2 \phi + r_e^2 \sin^2 \phi} \quad (6.16)$$

All quantities to compute the planet flux are obtained from the NASA Horizons web site [12], and are listed in table 6.3. To compute the planet fluxes for a given date, we use the python photometry package available at [11].

	Uranus	Neptune
r_e [km]	25559	24764
r_p [km]	24973	24341
ϕ	Ob-lat	Ob-lat
D [AU]	delta	delta

Table 6.3: Physical quantities used for the Uranus and Neptune fluxes computation (equation 6.15. Ob-lat and delta are quantities tabulated by NASA Horizons system [12] as a function of the date

The model spectra are linearly interpolated in log space at the reference frequencies of the NIKA2 bandpasses. Fluxes for all NIKA2 calibration runs are listed in table 6.4, together with the expected variation between the start and end of a run.

The Uranus and Neptune models have been compared to Planck observations of these planets [10]. For Uranus, the model used in the comparison is the ESA V2, and it is found to

overpredict by 4 K (about 4%) the observed RJ temperature at 143 GHz, to agree at 217 GHz, and to underpredict at 353 GHz. We use for NIKA2 calibration ESA model V4, that predict a flux respectively -3.3%, 0.3% and 4.7% higher in the the 143, 217 and 353 GHz, that would lead to a percent accuracy with respect to Planck observations.

For Neptune, the same study compared Planck observation with the ESA V5 model, *i. e.* the same one used for NIKA2 calibration. For this planet, temperatures are found to disagree at most by 5 K, i.e 4.1%, with the same trend with frequency as observed for Uranus. All thing considered, this study confirm that Uranus ESA V4 and Neptune ESA V5 models are accurate to 5% for predicting planet fluxes. Calibration values tabulated in Table 6.4 show that the variations of Uranus and Neptune over the duration of a typical NIKA2 run are negligible compared to the model accuracy. On the other hand, not taking into account the planet shape and orientation with respect to the observer in the computations of its solid angle can lead to errors between 1 and 2% as illustrated in the Python notebook [9] distributed with the software.

6.3.2 Mars

For Mars, we use the model of Belloche & Amri (2006) available at [8], with default parameters. Model output is computed at the two reference frequencies of NIKA2, 150 and 260 GHz.

Fluxes of Mars are tabulated in table 6.4. In many cases, the variations of Mars flux during the course of a run are larger than the model uncertainty (5%), and should be recomputed at more frequent times.

6.4 Relative calibration, flat field

Absolute calibration requires known sources in the sky and the ability to correct for atmospheric absorption. While absolute calibration of each KID also *de facto* provide relative calibration, the latter is interesting in itself to characterize the instrument. We focus on this aspect in this section.

The dispersion of the detector responsivity across the field of view (a. k. a. Flat Fields) has been characterized in several ways:

- **Main beam flat field.** This the relative calibration of the KID main beam. It is the PSF response to a point source in the far field of the telescope. It is estimated per KID using *beammaps* on bright sources that have the required sampling to give maps per individual KID (sect 2.3.6). We derive these “gains” G_k as:

$$G_k = \frac{S_{th}(\nu_0) e^{-\tau/\sin(\delta)}}{A_k}, \quad (6.17)$$

where $S_{th}(\nu_0)$ is the expected flux of the source integrated in the NIKA2 bandpasses and derived at the reference frequency ν_0 , $\tau/\sin(\delta)$ is the line-of-sight opacity measured using the *skydip* method (sect. 3) and A_k is the amplitude of a Gaussian of fixed FWHM fitted from the detector k map (as ϕ in Eq. 2.8).

- **Forward beam flat field:** the relative calibration of the response of each KID to the near field atmospheric background. It is estimated using the correlation factor of each detector TOI (apart from a bright source) to a median common mode estimated off-source (see sect. 2.2.4 for more details on common modes).

NR ^a	JD ^b	Δt ^c	$S_\nu(260 \text{ GHz})$ ^d	$S_\nu(150 \text{ GHz})$ ^e	$\Delta S_\nu / S_\nu^f$
	d	d	Jy	Jy	%
Uranus					
13	2457330.5	12	45.59	17.65	-0.89
14	2457354.5	8	44.44	17.21	-1.07
15	2457409.5	20	40.62	15.73	-3.22
16	2457455.5	14	38.27	14.82	-1.16
18	2457660.0	25	46.06	17.83	+1.25
19	2457690.0	7	46.09	17.85	-0.32
20	2457732.0	7	44.14	17.09	-1.04
21	2457764.5	4	41.82	16.19	-0.69
22	2457809.0	7	39.08	15.13	-0.83
23	2457865.0	7	37.96	14.70	+0.14
24	2457915.4	5	39.49	15.29	+0.66
Neptune					
13	2457330.5	12	17.09	7.18	-1.26
14	2457354.5	8	16.64	6.99	-0.92
15	2457409.5	20	15.76	6.62	-1.35
16	2457455.5	14	15.55	6.53	+0.19
18	2457660.0	25	17.65	7.41	-1.30
19	2457690.0	7	17.24	7.24	-0.68
20	2457732.0	7	16.46	6.91	-0.79
21	2457764.5	4	15.92	6.68	-0.34
22	2457809.0	7	15.56	6.53	-0.08
23	2457865.0	7	15.89	6.67	+0.57
24	2457915.4	5	16.73	7.02	+0.56
Mars					
13	2457330.5	12	146.19	48.30	+7.75
14	2457354.5	8	175.88	58.14	+8.70
15	2457409.5	20	319.71	105.62	+27.68
16	2457455.5	14	666.46	218.49	+30.37
18	2457660.0	25	597.17	199.44	-21.61
19	2457690.0	7	439.23	146.24	-4.82
20	2457732.0	7	311.78	103.98	-4.89
21	2457764.5	4	239.37	79.54	-2.12
22	2457809.0	7	174.99	57.94	-4.94
23	2457865.0	7	123.61	40.61	-5.44
24	2457915.4	5	102.08	33.68	+0.59

Table 6.4: a: Nika Run, b: Julian Date when the model are computed, c: Run duration, d, e: total fluxes at 260 and 150 GHz, f: variation of the 150 GHz flux density over the duration of the run

Figures 6.1 and 6.2 show the average main beam and forward beam flat fields for the three arrays. These have been constructed by combining the normalized flat fields of five *beammaps*, which were selected by thresholding the line-of-sight opacity measured in the 1 mm band, such as $\tau / \sin(\delta) \leq 0.85$. The distributions for the average flat fields are shown in the bottom panel of Fig. 6.1 and 6.2.

We observe a sizable variation of the flat fields for A1 from the left-most side to the right-most side of the FOV: this reveals a significant change of A1 detector responsivities depending on their position in the FOV. Namely, this effect, the origin of which is under investigation, mainly impacts the left-most third of the array, which will be referred to as the "shadow-zone". This variation of the flat field translates into a broadening of the distribution. However, we verified that A1's flat field dispersions are in line with the ones of A3 after the detectors within the shadow-zone were flagged out using a crescent-shaped mask. The masked flat field distributions are shown in green in Fig. 6.1 and 6.2, whereas shadow-zone distributions are in red. In addition to the average flat fields, we further characterize the flat fields for individual *beammaps*. Fig. 6.3 shows the dispersion of the flat fields for nine *beammaps* using either the whole FOV or masking the shadow-zone. The dispersion estimates for this two cases are gathered in Table 6.4.

Dispersion (%)	KID selection	A1	A3	A2
Main beam flat field	all the FOV	34.4 ± 3.4	15.5 ± 1.4	13.2 ± 1.7
	shadow-zone excluded	17.0 ± 1.1	14.2 ± 1.2	12.8 ± 1.3
Forward beam flat field	all the FOV	21.6 ± 1.4	10.1 ± 1.7	5.2 ± 0.9
	shadow zone excluded	12.2 ± 1.6	10.1 ± 2.1	4.9 ± 1.2

Table 6.5: Average flat field dispersions in percent for nine *beammaps* over all the FOV and after masking out the shadow-zone

6.5 Telescope-driven beam variations

In this section, we evidence a beam size broadening depending on the scan observation date. This effect, which mainly impacts late afternoon observations and is reproducible from a campaign to another, is probably due to deformations of the main dish subject to the Sun heating. This is a well-known effect, which also impacts EMIR and was observed for the previous generation of instrument MAMBO. However, compared to the period when MAMBO or NIKA were on activity, these daily deformations have probably strengthen due to the aging of the main dish white coating.

6.5.1 Beam monitoring using bright source scans

We monitor the time-dependent beam-size variations using all the available bright source scans acquired at the optimal focus for each campaign. Bright sources are selected by thresholding the flux density estimates above 1 Jy at both wavelengths. The beam size is estimated by fitting a 2D Gaussian from the map and taking the geometrical FWHM, defined as $\text{FWHM}_{\text{geom}} = (\text{FWHM}_x \text{FWHM}_y)^{1/2}$, where FWHM_x and FWHM_y are the best-fitting values of FWHM along the minor and major axis of the elliptical 2D Gaussian. For Uranus, the FWHM estimates are corrected for the beam broadening due to the finite extension of the apparent disc, as in Sect. 5.2.

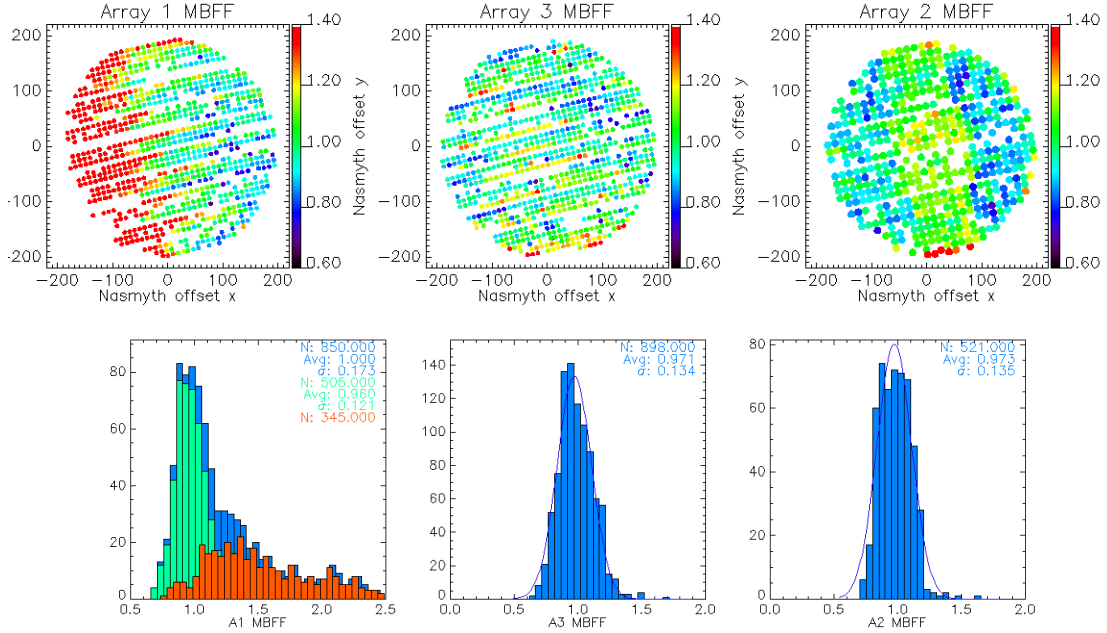


Figure 6.1: Average main beam flat fields obtained by combining the normalized flat fields of five *beammap* scans. The top row plots show the average flat fields of Array 1, 3 and 2 in Nasmyth coordinates, and the bottom plots show the average flat field distributions using all KIDs (blue), using Array 1 KIDs that are positioned out of the shadow zone (green) and using Array 1 KIDs inside the shadow zone, which is defined in the text.

Figure 6.4 shows the geometrical FWHM as a function of the observing time of the scans in UT hours for all OTF scans of bright sources for the N2R9 commissioning campaign as well as for the N2R12 and N2R14 science pools. For the three campaigns, we observe the same evolution of the FWHM, which goes from a plateau at a median value of $11.3''$ at 1 mm and $17.5''$ at 2 mm during the night, to a smooth rise that reaches a maximum of about $14''$ at 1 mm and $18.5''$ at 2 mm around 16:00 UT hours. The beam broadening begins to become sizable around 15:00 UT and one has to wait until around 22:00 UT for the beam sizes to lay down on the stability plateau. The UT time ranges that are discarded using the baseline scan selection (see Sect. 2.3.7) are shown as cross-hatched areas in Fig. 6.4. They correspond to the afternoon period between 15:00 and 22:00 UT hours, that is when the telescope main dish is heated by daylight, as well as the 9:00-to-10:00 Sun rising period. The same beam size variations in time using scans of giant planets (Uranus and Neptune) or other bright sources (mainly quasars) are observed. However, FWHM from planets observation tend to be slightly larger than FWHM from the observation of other sources. This originates from larger 2D Gaussian fitted values due to the error beams, which are measured with a signal-to-noise as higher so as the source is bright. This small effect is accounted for the beam-dependent calibration cross-check discussed in Sect. 6.7.

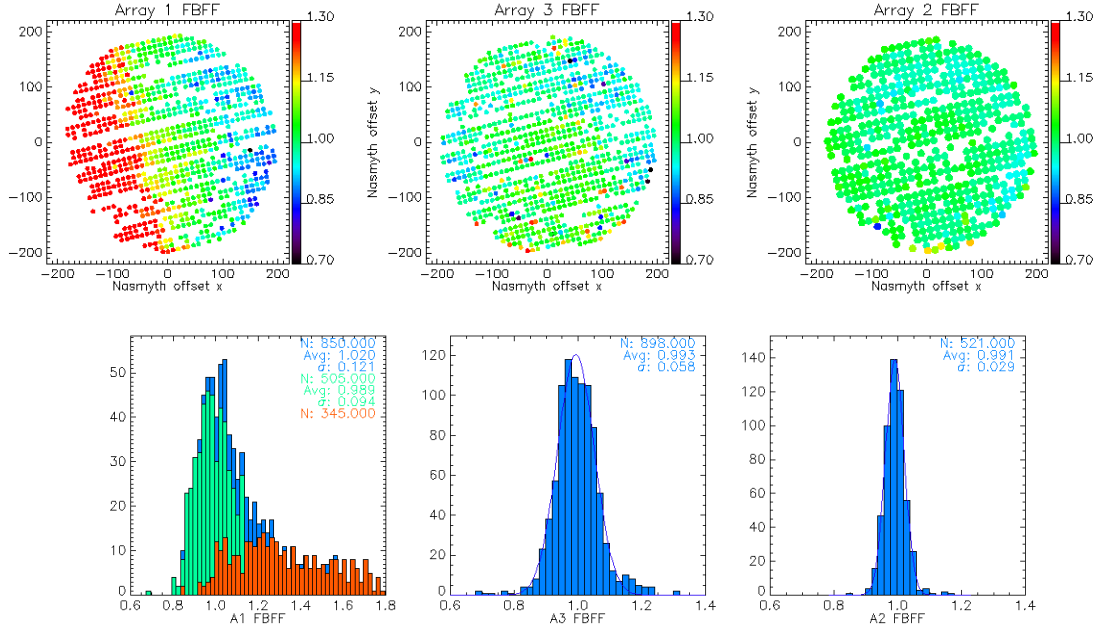


Figure 6.2: Average forward efficiency flat field for array 1, 3 and 2. Same legend as Fig. 6.1

6.5.2 Beam monitoring using pointing

As discussed in Sect. 2.3.4, the telescope pointing is monitored on a hour basis during observation using pointing scans. However, as they consist of two sub-scans in azimuth and elevation of about 10 seconds of integration time each, pointing scans can be used to make a map of the pointing source. For each campaign, we thus have on hand hundreds of maps of mostly point-like bright sources. These can be also used to monitor the beam size.

For this purpose, pointing scans are reduced using the data analysis pipeline described in Sect. 2.2 with the same parameters as for standard OTF scans, and projected onto maps of $2''$ resolution. As previously, an elliptical 2D Gaussian is then fitted from the map and a geometrical FWHM is formed from the best-fitting FWHM along the two ellipse radii. FWHM estimates on Uranus maps are corrected for an offset due to the finite size of the apparent disc, as discussed in Sect. 6.5.1. Pointing scans on other extended sources, such as NGC7027, are discarded from the analysis.

In Fig. 6.5, we present the FWHM estimates using pointing scans as a function of the observing time in UT hours for three observation campaigns. We observe the same the beam size evolution with UT hours as previously discussed in Sect. 6.5.1, that is a plateau during night-time and a smooth increase during day-time up to a maximum in the afternoon, which is followed by a smooth decrease down to the plateau a few hours after the sunset. Although the general trend is the same as the OTF-based FWHM variations, more dispersion is seen either using pointings toward giant planets or other bright sources. The pointing-based FWHM constitute a time-sampling of the FWHM during the whole observation campaign. They can serve to estimate the beam size of any observation scans, in particular toward sources too faint

Draft

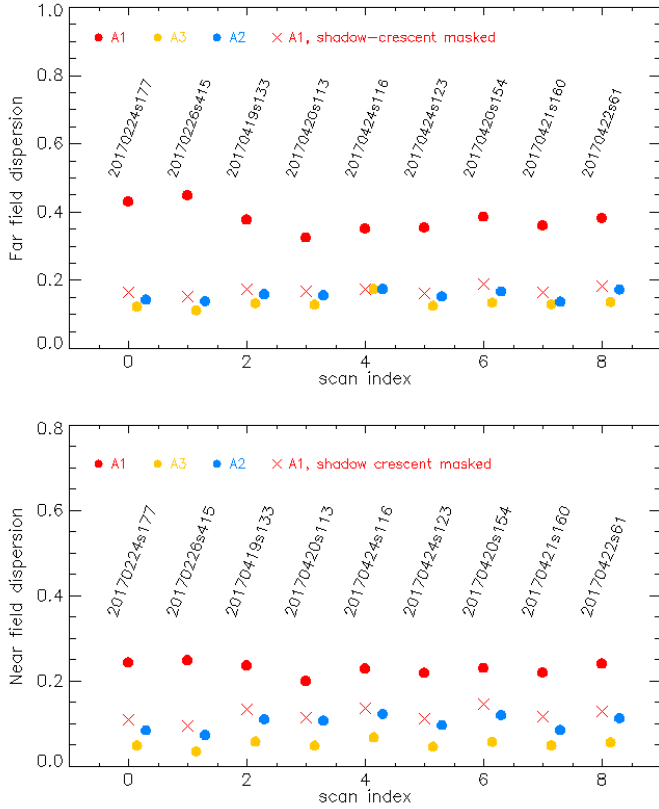


Figure 6.3: The RMS dispersion of the main beam flat field (upper panel) and forward beam flat field (lower panel) are shown using all valid KIDs of Array 1 (red circles), Array 3 (orange circles) and Array 2 (blue circles), and using the KIDs located outside the Array 1 "shadow area", which was discarded using a left crescent-shaped mask (red crosses).

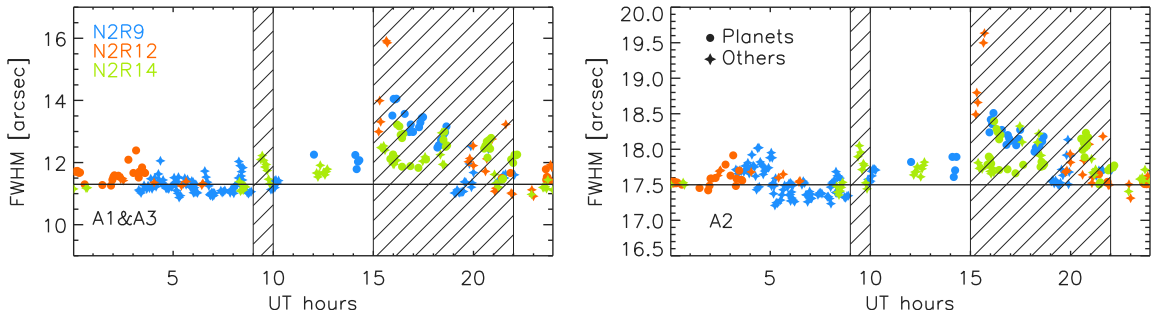


Figure 6.4: Beam size monitoring using OTF scans. FWHM at 1 mm (left panel) and 2 mm (right panel) as a function of the observation time in UT hours are shown using scans of giant planets (filled circles) and bright point-like sources above 1 Jy (filled stars) for N2R9 commissioning campaign and N2R12 and N2R14 science pools. The cross-hatched areas corresponds to observing time period that are discarded using the baseline selection, as described in Sect. 2.3.7.

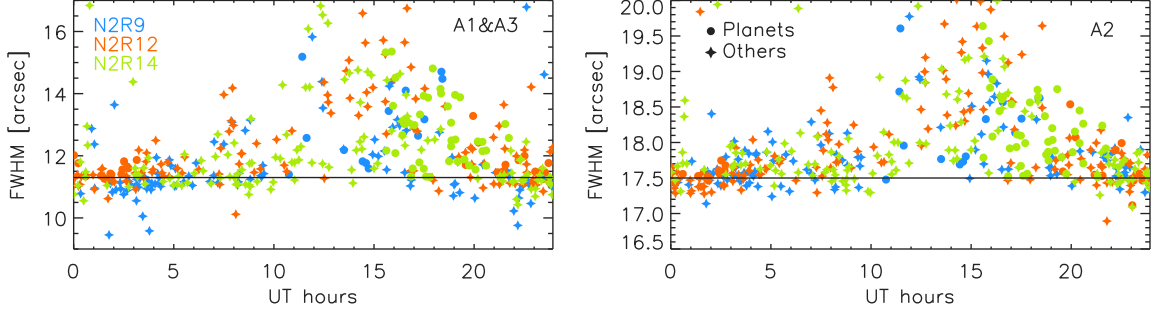


Figure 6.5: Beam size monitoring using pointing scans. Same legend as in Fig. 6.4.

for a direct FWHM fit to be made on the projected map. To mitigate the dispersion, the time-stamped pointing-based FWHM is filtered with a running median on a 70-minute width time window. Then, the FWHM at the time of the considered scans is interpolated from the smoothed pointing-based time-stamped FWHM. Figure 6.5 shows two different FWHM estimates for the

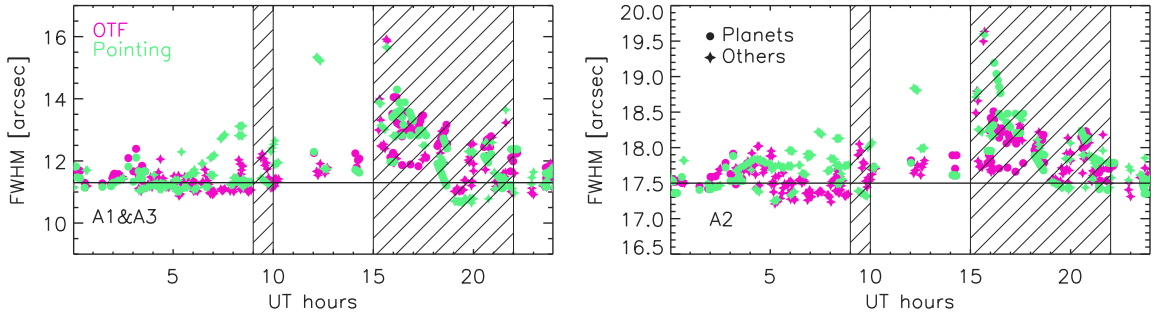


Figure 6.6: Beam size monitoring comparison. The FWHM estimates from a 2D Gaussian fit on the map of OTF scans toward bright sources ('OTF'-labeled pink data points) are compared to FWHM estimates that are obtained by interpolating the smoothed pointing-based FWHM at the time of the scans ('Pointing'-labeled light green data points).

same data set: the best-fitting FWHM estimates on the map are compared with the interpolation from the pointing-based FWHM monitoring. The two estimates are well in agreement with each other, although the pointing-based estimates have more dispersion and a few outliers.

As a summary, we have evidenced a systematic beam size variation with the observation time using two different data sets: a series of OTF scans of bright sources and pointing scans. The beam size variation is i) reproducible from a campaign to another, stable with ii) the data set and iii) the sources. It consists of a beam broadening during afternoons, as the 30 m dish is heated by the daylight, and an increase of the dispersion during sunrises. The most impacted observing periods are well discarded using the baseline selection criteria discussed in Sect. 2.3.7.

6.6 Baseline Calibration

6.6.1 Methodology

The absolute calibration is based on the calibration in $FWHM_0$ beam described in Sect. 6.2.2. Practically, it consists in evaluating a flux density rescaling factor using a series of OTF scans toward planets. This flux rescaling factor is an estimate of the $S_c(\nu_0)$ -to- A_c ratio of Eq. 6.9. The calibrator flux density expectation $S_c(\nu_0)$ is obtained as discussed in Sect. 6.3, whereas the measured amplitude A_c is estimated as the average amplitude of the $FWHM_0$ Gaussian fitted from a series of calibrator maps.

Before the flux density estimation, the calibrator raw data are i) intercalibrated as described in Sect. 6.4 and ii) corrected of the atmospheric attenuation as described in Chapter 3. To refine the intercalibration between the two 1-mm arrays after the KID Hertz to Jy/beam conversion factor estimates, a flux rescaling factor per array is calculated. Regarding the correction of the atmospheric attenuation, we resort to the ‘corrected skydip’ opacity correction, as described in Sect. 3.5, for the baseline calibration. However, calibrations relying on the ‘taumeter’ (Sect. 3.1) and the ‘skydip’ (Sect. 3.2) methods are also derived, and will be used for performing the photometry robustness tests discussed in Sect. 7.4. Finally, the telescope-driven beam effect, discussed in Sect. 6.5, is mitigated by using the baseline scan selection of Sect. 2.3.7, in which, we recall, the most impacted scans are discarded by mean of a cut on the observation date.

6.6.2 Scan selection

To illustrate the baseline selection efficiency, we present Uranus measured-to-predicted flux density ratios as a function of the 2D Gaussian FWHM estimates and color-coded from the observation dates given in UT hours in the first panels of Fig. 6.7. We note that the flux density estimates have been corrected by the rescaling factors, so that the flux density ratios are equal to unity in average by construction. First row panels of Fig. 6.7 show the flux ratio after correction from the baseline rescaling factors, whereas second and third row panels are for ‘taumeter’-based and ‘skydip’-based absolute calibration respectively. For the baseline calibration, the selected scan flux ratios (shown as full circles) are stable against the beam FWHM. The ‘taumeter’-based selected flux ratios show more dispersion but no significant dependence on the FWHM. The flux ratio-to-FWHM correlation is most clearly seen for the ‘skydip’-based calibration: broaden beams are associated with lower fluxes. However, this correlation is efficiently mitigated after the baseline scan selection. The residual anti-correlation between the ‘skydip’ flux ratios and beams originates from a mild correlation of the flux density with the atmospheric transmission as discussed later in Sect. 7.4.

The Uranus available scan numbers and the scan numbers after the baseline scan selection was performed are given per observation campaigns and for the combination of the three considered campaigns in Table 6.6. For N2R9 and N2R14, which were both February campaigns one year apart, Uranus was mainly visible during the day. As a result, only two good scans are used to derive the absolute calibration. However, we will verify in Sect. 7.3 that this suffices to obtain an accurate photometry. By contrast, due to the night time visibility of Uranus during N2R12, almost all the available scans meet the baseline section criteria.

		Datasets			
Scan number		N2R9	N2R12	N2R14	Combined
Total		27	25	40	92
Selected	Baseline	2	22	2	26
	Photocorr	2	24	12	38

Table 6.6: Number of scans for the absolute calibration

6.6.3 Stability against the atmospheric transmission

We test the stability of Uranus flux density ratio against the atmospheric transmission. The later quantity, we recall, depends on the measured zenith opacity τ and the scan average airmass $x = \text{cosec}(\delta)$ as $\exp -\tau \cdot x$. In Fig. 6.8, Uranus flux ratios of Array 1, Array 3, the 1-mm array combination and Array 2 are plotted as a function of the atmospheric transmission for the three considered observation campaigns (N2R9, N2R12 & N2R14). Although Uranus flux ratio per campaign is equal to the unity in average by construction, any trend as a function of the observing conditions would sign the presence of a systematic effect. However, no sizable dependencies of the flux ratio on the atmospheric transmission is observed in Fig. 6.8. This constitutes a first indication of the robustness of the flux density estimates against the atmospheric conditions using the baseline calibration. This will be further tested using more scans in Sect. 7.3.

6.6.4 Comparison with other opacity correction methods

Whereas the baseline calibration relies on correcting for the atmospheric attenuation using the ‘corrected skydip’ method described in Sect. 3.5, here we derive the absolute calibration factor using the ‘taumeter’ and the ‘skydip’ opacity correction methods, as discussed in Sect. 3.1 and Sect. 3.2. The baseline Uranus measured-to-modeled flux ratio as a function of the atmospheric transmission for A1&A3 and for A2 are copied in the first row of Fig. 6.9, and are compared to the ‘taumeter’-based flux ratios (second row) and ‘skydip’-based flux ratios (third row). We observe more dispersion for the ‘taumeter’-based flux ratio, whereas the ‘skydip’-based ratios are very similar as the ‘baseline’ ratios except for a slight decrease of the flux at low atmospheric transmission. We further quantify the difference between methods in evaluating i) the average absolute calibration rescaling factor with respect to the baseline factor and ii) the rms dispersion of the measured-to-modeled flux ratio. These quantities are gathered in Table 6.7 in the rows labeled ‘Factor’ and ‘RMS’ respectively. Resorting to a different opacity correction results in small changes of the absolute calibration factors, up to a 13% increase for Array 1 using ‘skydip’. However, these modifications of the absolute calibration has no sizable impact on the photometry, as we will check in Chapter 7 (see e.g. Table 7.3). From the RMS row, we confirm an increase of the ‘taumeter’-based flux ratio dispersion of about 40% at 1 mm and about 60% at 2 mm w.r.t. the baseline dispersion, whereas ‘skydip’ dispersions are basically the same as ‘baseline’. Thus the ‘taumeter’ and ‘skydip’ methods can be used for the absolute calibration in complement to the baseline method, e.g. to perform robustness tests as in Chapter 7.

6.7 Calibration using a photometric correction

As discussed in Sect. 6.5, observations during the afternoon sessions or during sunrise are deeply affected by the telescope-driven beam size variations, which are either due to an increase of the main dish temperature (afternoons) or to a focus drift (sunrises). For the baseline calibration presented in Sect. 6.6, this effect was mitigated by discarding the scans acquired during these periods, as defined by the baseline selection of Sect. 2.3.7. However, in this section, we address the issue of calibrating in telescope-driven unstable observing conditions. We discuss a calibration method that relies on a photometric correction depending on the beam size.

When using the photometric correction, no scan selection based on the observation date is performed. However, the scans from which the absolute calibration is derived, are selected on the FWHM estimate using the same criteria as for the baseline calibration, that are FWHM thresholds of $12.5''$ at 1mm and $18''$ at 2mm. Thus, only the scans that are moderately affected by the beam effect are included in the absolute calibration in order not to include twice the photometric correction uncertainties in the error budget (once for the absolute calibration and once for the photometry).

6.7.1 Photometric correction methods

When the beam size broadens due to e.g. temperature increase of the telescope main dish, the flux density is smeared in a larger solid angle and the flux density estimator, which is based on the amplitude fit of a Gaussian beam of fixed FWHM as described in Sect. 6.2.2, is biased toward low flux densities.

Considering only the main beam broadening, modeled as a Gaussian of size $FWHM' = 2\sqrt{2 \ln 2} \sigma'$, we show in Sect. A.3.6 that the flux density estimator depends on the size of the convolution function between the enlarged σ' Gaussian and the σ_0 fixed width Gaussian of our reference system. An unbaised flux density \hat{S}_{pc} can be derived from the flux density estimate \hat{S} as

$$\hat{S}_{pc} = f(\sigma') \hat{S}, \quad (6.18)$$

where $f(\sigma')$ is a photometric correction of the beam variation effect. Within the Gaussian model, it reads:

$$f(\sigma') = \frac{(\sigma'^2 + \sigma_0^2)}{\sigma_*^2 + \sigma_0^2}. \quad (6.19)$$

The beam size in stable observing condition σ_* is determined by measuring the 2D Gaussian beam on the series of scans of source with various flux density, which has been used for the beam characterization in Sect. 5.2. An empirical model for the small correlation of σ_* with the source flux density is given in Sect. A.3.6.

The photometric correction thus relies on the measure of the current beam size σ . The induced uncertainty on the flux density measurements depends on the precision of which we are able to monitor the beam size.

We perform two case studies: Sect. 6.7.1 presents a demonstration calibration assuming the beam is precisely monitored, whereas Sect. 6.7.1 addresses a practical calibration relying on a beam monitoring using pointing scans.

Demonstration case

For the demonstration case, shortened as 'demo' hereafter, we use a photometric correction based on the Gaussian FWHM fitted on the map of the source. This method thus applies only on point-like sources that are bright enough for an accurate fit of the beam to be obtained using a single scan.

The beam size is estimated by fitting a 2D Gaussian from the map and forming the geometrical σ , $\sigma_{\text{geom}} = (\sigma_x \sigma_y)^{1/2}$.

In order to capture only the beam size variations driven by the telescope, a small correction δ_{geom} has to be made to the 2D Gaussian beam estimate for bright sources. The estimate of the actual Gaussian size $\hat{\sigma}'$ is

$$\hat{\sigma}' = \sigma_{\text{geom}} - \delta_{\text{geom}}, \quad (6.20)$$

where the offset δ_{geom} is null for faint or moderately bright point sources, and non-zero for bright sources. As for σ_* , the 2D Gaussian fit yields slightly broaden σ_{geom} for bright sources (e.g. planets) to accomodate for the side lobes, which are measured with high signal-to-noise. For Uranus, δ_{geom} includes also the beam widening due to Uranus disc, which is seen with a diameter of about 3.5'' at the IRAM 30-m telescope latitude. We measure Uranus δ_{geom} by comparing the average σ_{geom} estimates using Uranus scans and using MWC349 scans, we found $\delta_{\text{geom}} = 0.4$ at 1-mm and $\delta_{\text{geom}} = 0.25$ at 2-mm, in consistency with the empirical σ_* variations with flux discussed in Sect. A.3.6.

Practical case using pointing scans

For sources fainter than about one Jy, the signal to noise ratio is in general not high enough to allow for a precise measure of the beam to be made from a single observation scan, so that the 'demo' is not usable. Ideally, dedicated scans must be made in order to accurately monitor the beam variations, e.g. a few minute duration OTF scan on a pointing sources every 30 or 60 minutes. These scans are not available yet. However, here we propose and test the use of the *pointing* scans themselves to monitor the beam.

The pointing scans, which are described in Sect. 2.3.4, are used to estimate pointing corrections during observations. As they consist of two sub-scans in azimuth and elevation of about 10 seconds of integration time each, they can be used to project a map of the pointing source. The beam size is estimated by fitting a 2D Gaussian and forming the geometrical FWHM, labeled $FWHM_p$. No significant offset is observed for bright sources because, unlike maps based on OTF scans, pointing scan maps have not enough signal to noise for a significant impact of side lobes on the geometrical FWHM. However, the beam widening due to the apparent diameter is corrected in the case of Uranus. As a summary, for the pointing-based photometry correction method, shortened as 'pointing' hereafter, the beam variations are monitored using the estimate of the actual Gaussian size $\hat{\sigma}'$

$$\hat{\sigma}' = \sigma_p - \delta_p, \quad (6.21)$$

where σ_p is the geometrical σ corresponding to $FWHM_p$ and the offset δ_p is null for point-like sources and equals to 0.2'' at 1mm and 0.13'' at 2mm for pointing scan of Uranus. The beam variation monitoring using pointing scans is further detailed in Sect. 6.5.

6.7.2 Stability against observing conditions

Here we check the stability of Uranus measured-to-predicted flux density ratio against the beam size and the atmospheric transmission when using a photometric correction for the beam variations. The measured flux density relies on the 'corrected skydip' opacity measurements to correct for the atmospheric attenuation.

First, we present Uranus flux density ratio as a function of the beam FWHM after the photometric correction with the 'demo' and 'pointing' methods in the fourth and fifth row panels of Fig. 6.7 respectively. The flux density is stable against the beam FWHM within rms errors for both wavelengths. In addition, more scans are used for the absolute calibration, as also reported in Table. 6.6, including scans acquired in the early afternoon.

In Fig. 6.9, we check the stability of Uranus flux density ratios againts the atmospheric transmission using the 'demo' (fourth row) and 'pointing' (last row) photometric corrections. The atmospheric transmission model and the colour conventions are the same as in Sect. 6.6.3. The flux ratios at both wavelengths are consistent with the unity within statistical errors for the whole tested range of atmospheric transmissions using both the 'demo' and the 'pointing' photometric correction. Average absolute calibration factors normalised to the baseline calibration factor, as well as the rms errors are gathered in Table 6.7 in the columns labeled 'photocorr demo' and 'photocorr pointing'. We find that, resorting to a photometric correction i) allows us to use 45% more scans for the absolute calibration, ii) has a negligable impact on the absolute calibration factor and iii) yields a small reduction of the flux density ratio dispersion. For the absolute calibration, the 'pointing' photometric correction performs as well as the 'demo' case. Photometry capability and stability when using a photometric correction will be further tested in Sect. 7.4.

Characteristics		Methods				
		baseline	taumeter	skydip	photocorr demo	photocorr pointing
# selected scans		26	26	26	38	38
Factor	A1	1.00	0.97	1.13	1.01	1.02
	A3	1.00	0.97	1.02	1.01	1.00
	1mm	1.00	0.95	1.06	1.01	1.01
	2mm	1.00	0.94	0.99	1.01	1.01
RMS	A1	3.2	4.2	3.4	3.5	3.0
	A3	3.6	4.3	3.3	3.5	3.0
	1mm	3.3	4.5	3.3	3.1	2.6
	2mm	1.6	2.6	1.5	1.5	1.5

Table 6.7: Comparison of calibration results using five methods

6.8 Aperture Photometry Calibration

The total flux density of a source can be measured in the NIKA2 image over a large circular aperture to recover the source power incident on the telescope through its main beam as well as its side lobes. It is computed as :

$$S_\nu = \sum_m \sum_n I_{m,n} (\text{Jy}/\text{beam}) \times \frac{dx^2}{\Omega_{tot}} \quad (6.22)$$

$I_{m,n}$ is the brightness in Jy/beam measured in each pixel (m, n) ; dx is the pixel size; Ω_{tot} is the solid angle of the *total* beam; pixel indices (m, n) are such that the radial distance $dx \times \sqrt{(m - m_c)^2 + (n - n_c)^2}$ from the map center (m_c, n_c) is within the aperture radius.

Since flux density uncertainty grows with aperture radius, we have tested various aperture size from $60''$ to $250''$ and found that $150''$ is a good compromise between uncertainty and full saturation of the flux density (see Figure 6.10). We note however that the power uncounted for beyond an aperture radius of $250''$ is about 30% at 260 GHz in using parameters in Tables 1 and 4 of Kramer et al. (2013).

In each pixel, brightness $I_{m,n}$ is naturally expressed in unit of Jy/beam, where *beam* stands for the *total* beam. Hence, prior to summing all pixels within the aperture with Eq. 6.22, brightness $I_{m,n}$ must be converted from Jy/beam to Jy/pixel. This conversion is done with the factor $\frac{dx^2}{\Omega_{tot}}$ which is, effectively, the pixel area dx^2 in unit of fractional beam.

The solid angle of the total beam Ω_{tot} has been assumed constant and taken as the mean value computed from the series of 75 *beammap* scans of Uranus and Neptune that are described in Sect. 5.3. It is :

$$\Omega_{tot}(r_{max}) = \int_0^{r_{max}} B(r) 2\pi r dr \quad (6.23)$$

where $B(r)$ is the full beam profile as defined in Sect. 5.1.3 and have been obtained in azimuthally averaging brigtness over narrow annuli dr in width, and normalised so that $B(0)=1$ (R. Adam's thesis (2016) or J.D. Kraus (1980)). We have used $r_{max} = 180''$ which is the maximum extent allowed for uniform rms in the maps acquired during observations of N2R9, N2R12 and N2R14. Results are given in Table 6.8.

The excess of the total beam relative to the Gaussian main beam is the ratio $\Omega_{tot}/2\pi(\sigma_{Gauss})^2$, with σ_{Gauss} derived from the *FWHM* of the main beam determined in Sect. 5.2.

Table 6.8: Solid angle of total beam based on Uranus and Neptune observations

run	Nber of scans	Ω_{tot} (arcsec 2)			$\Omega_{tot}/\Omega_{gauss}$		
		A1	A2	A3	A1	A2	A3
r9	27	265 \pm 23	466 \pm 17	252 \pm 23	1.80 \pm 0.12	1.35 \pm 0.05	1.74 \pm 0.13
r12	20	229 \pm 11	437 \pm 9	221 \pm 10	1.71 \pm 0.06	1.30 \pm 0.02	1.68 \pm 0.06
r14	28	251 \pm 16	457 \pm 15	245 \pm 18	1.73 \pm 0.08	1.32 \pm 0.03	1.72 \pm 0.08
mean		248	453	239	1.74	1.32	1.71

Finally, in Table 6.9, we provide the ratio between the flux densities derived by aperture photometry and derived using the fixed-width Gaussian photometry, as defined in Sect. 6.2.2. These ratios are larger than unity and indicate that aperture photometry recovers more flux density than a Gaussian fit as expected.

Table 6.9: ratio aperture photometry / fixed-width Gaussian flux densities

run	Nber of scans	A1	A2	A3
r9	27	1.08 ± 0.03	1.04 ± 0.02	1.09 ± 0.03
r12	20	1.12 ± 0.02	1.05 ± 0.02	1.13 ± 0.02
r14	28	1.09 ± 0.03	1.03 ± 0.02	1.09 ± 0.03

Draft

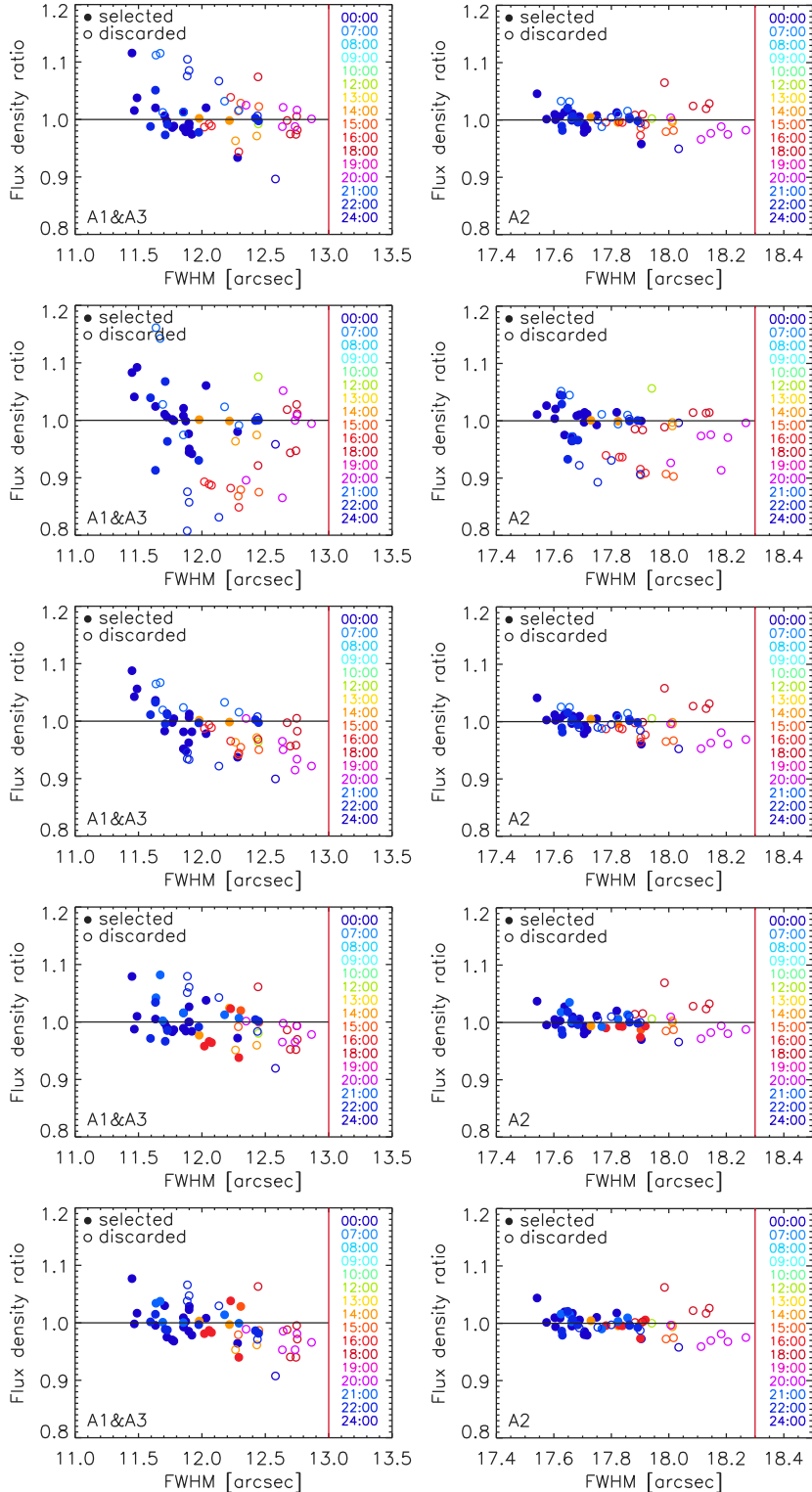


Figure 6.7: Uranus flux density ratio vs beam size for five calibration methods. The ratio of Uranus measured flux densities to expectations in function of the measured 2D Gaussian beam FWHM is shown for the 1-mm array combination (left column) and for array 2 (right column) after absolute calibration using (*first row*): the baseline method, as well as (*second row*): the 'taumeter'-based and (*third row*): the 'skydip'-based methods, and methods relying to (*fourth row*): the 'demo' and (*fifth row*): the 'pointing' photometric corrections. These plots include all Uranus scans acquired during N2R9, N2R12 and N2R14 campaigns and whose beam FWHM are below the threshold indicated by the vertical red lines, (open circles), as well as the scans that met the baseline selection criteria (filled circles).

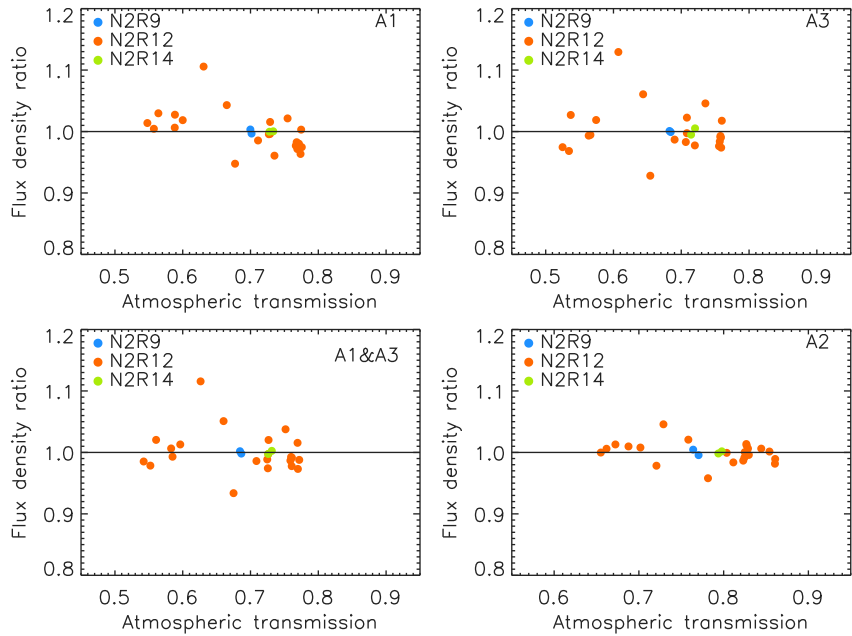


Figure 6.8: Uranus flux density ratio stability against the atmospheric transmission using the baseline calibration. The measured-to-modeled flux density ratio as a function of the measured atmospheric transmission is shown for array 1 (upper left), array 3 (upper right), 1mm array combination (lower left) and array 2 (lower right). The datapoints denote the flux ratio of Uranus scans acquired during N2R9 in blue, N2R12 in orange and N2R14 in Chartreuse (yellow green). For each campaign, flux ratios are equal to unity in average by construction. We observe no sizable systematic effect depending on the atmospheric transmission, modelled as the decreasing exponential function of the zenith opacity times the air mass at the telescope elevation.

Draft

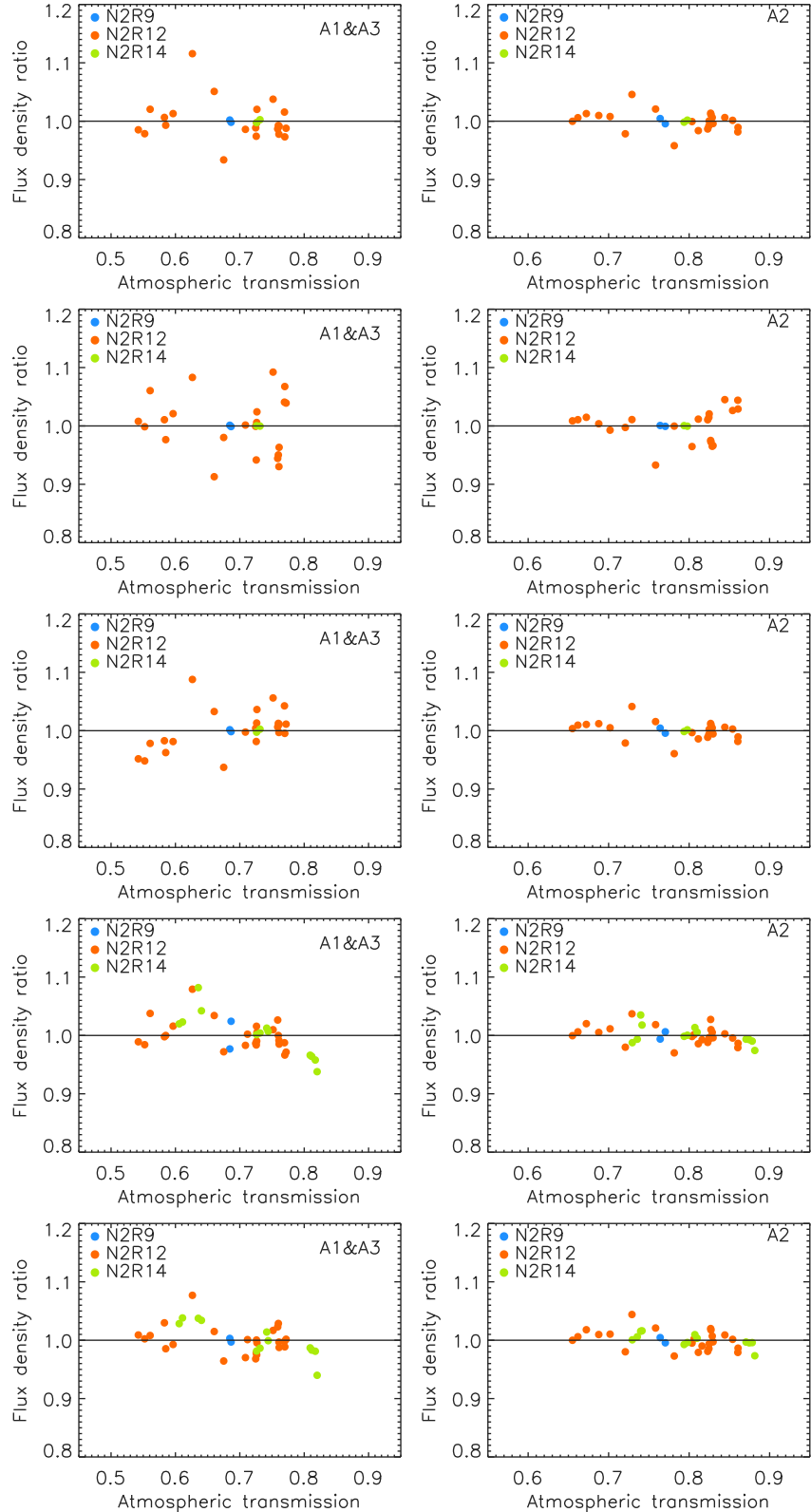


Figure 6.9: Uranus flux density ratio vs atmospheric transmission shown for the 1-mm array combination (left column) and for array 2 (right column) after absolute calibration using (*first row*) the baseline method, as well as (*second row*) the 'taumeter'-based and (*third row*) the 'skydip'-based methods, and methods relying to (*fourth row*) the 'demo' and (*fifth row*) the 'pointing' photometric corrections. These plots include all Uranus scans acquired during N2R9, N2R12 and N2R14 campaigns.

Draft

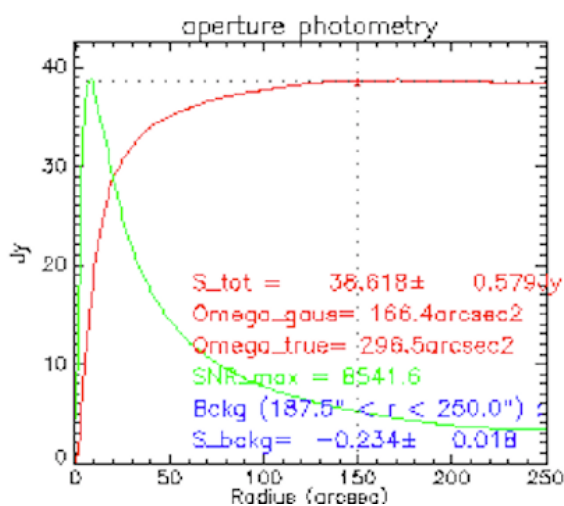


Figure 6.10: Aperture photometry of Uranus (20170227s308). Integrated flux density is the red curve that saturates at an aperture radius of $\sim 150''$. Uncertainty over this aperture is $\sim 2\%$ of the total flux density. **Alessia's comment: could you improve the resolution of the plot ?**

Chapter 7

Photometry accuracy and stability assessments

NIKA2 photometric capabilities after the calibration presented in Chapter 6, are assessed in this section. Firstly, we use observation of secondary calibrators (planetary nebulae NGC7027, CRL2688, and MWC349A) to test the consistency of the flux density estimates with expectations. Then, we verify the stability of the photometry with respect to the atmospheric conditions using a large amount of bright source observations.

The methodology to evaluate the photometric capabilities and calibration results are further described in Sect. 7.1. In Sect. 7.2, the flux density expectations in NIKA2 bands for the considered secondary calibrators are determined. Then, we evaluate both the calibrator measured-to-expected flux density ratio and the calibration statistical errors for the baseline calibration method in Sect. 7.3. In Sect. 7.4, we compare these results with other calibration method results.

7.1 Calibration validation criteria

7.1.1 Calibration bias

The calibration accuracy is primarily assessed by checking that the flux density measurement of known sources is unbiased.

This performance test also depends on the accuracy with which the chosen secondary calibrator SED is known. Our main secondary calibrator is MWC349, for which we have derived precise NIKA2 flux density expectations as discussed in Sect. 7.2. These are mainly limited by the absolute calibration of the Plateau de Bure interferometer and VLA.

We define the calibration bias b for array i as the ratio between the measured flux density \hat{S}_i using the fixed-width Gaussian beam photometry as discussed in Sect. 6.2.2 and the flux density expectations S_i^0 as given in Sect. 7.2. From a series of secondary calibrator scans, we evaluate the average calibration bias per array b_{A_i} , which by construction, should be equal to unity within the precision with which the expected flux densities are known. Moreover, the calibration bias stability against the observed opacity provides us with a robustness test of the opacity correction, and the stability against the measured beam size, a test of the photometric susceptibility to optical variations.

7.1.2 Calibration stability

We use a large amount of bright source observation scans to test the stability of the measured flux densities with respect to the observing conditions.

The selected bright source scans consists of the OTF scans that meet the baseline selection criteria and for which the flux estimate is above 800 mJy at 1 mm and 400 mJy at 2 mm. We consider only the sources for which a minimum of 10 scans are available after selection.

We evaluate the standard deviation of the bright source measured-to-median flux density ratio σ_{A_i} for each array or array combination. This quantity constitutes an estimate of the statistical calibration uncertainties that encloses errors of optical, atmospheric, noise and data processing origins. Added in quadrature with the model uncertainties reported in Moreno et al. and with the bandpass uncertainties, it represents a conservative estimate of the total absolute calibration errors.

7.2 Reference flux densities of the secondary calibrators

The secondary calibrator MWC349 consists of a stellar binary system, including the young Be star MWC349A, surrounded by a disk. Its radio continuum emission originates in an ionized bipolar outflow [7]. MWC349A has been monitored with the Plateau de Bure interferometer and VLA, and shown to be stable in time and only slightly angularly resolved, making it a point source for the 30-metre telescope. The SED of MWC349A [14] is presented in Fig. 7.1. We have computed its flux densities at the NIKA2 reference frequencies 150 and 260 GHz with $S_\nu = 1.16 \pm 0.01 \times (\nu/100\text{GHz})^{0.60 \pm 0.01}$ provided by this monitoring [14].

The secondary calibrator CRL2688 is an Asymptotic Giant Branch star. Its radio continuum emission is mostly from circumstellar dust and is somewhat extended [6]. Its flux densities at 850 μm and 450 μm have been stable at the 5% level as monitored by SCUBA2 in 2011-2012 [5]. We have extrapolated their flux densities to 150 and 260 GHz with the power law $S_\nu \propto \nu^\alpha$ and index $\alpha = 2.44 \pm 0.18$ derived from their SCUBA2 measurements.

The secondary calibrator NGC7027 is a young, dusty, carbon rich Planetary Nebula with an ionized core. It is extended in the continuum and molecular lines (Bieging et al 1991), and is not a point source for the 30-metre telescope. Its most recent flux densities are reported at 1100 μm and 2000 μm by Hoare et al (1992). It has been reported to decrease by ~ 0.145 percent/yr in the optically thin part of its spectrum above 6 GHz from VLA observations (Zijlstra, van Hoof & Perley 2008, and Hafez et al, 2008) that makes these flux densities uncertain by 3.6% currently. Its SED from cm wavelengths to optical is also presented in Hafez, Y.A. et al (2008). Its flux densities have been extrapolated to 150 and 260 GHz and the modelled decrease since 1992 included.

All these expected flux densities extrapolated from the literature are in Table 7.1.

Measured flux densities however is determined over the broad bandwidth of each array and so must be color-corrected to be compared to the expected flux densities of Table 7.1. For this purpose, we have derived color-corrections for sources with spectral indices α comprised between -2 and +4 in Table 6.2 of Sect. 6.2.3. As it can be seen, this effect can be a few % for MWC349, NGC7027, and CDL2688.

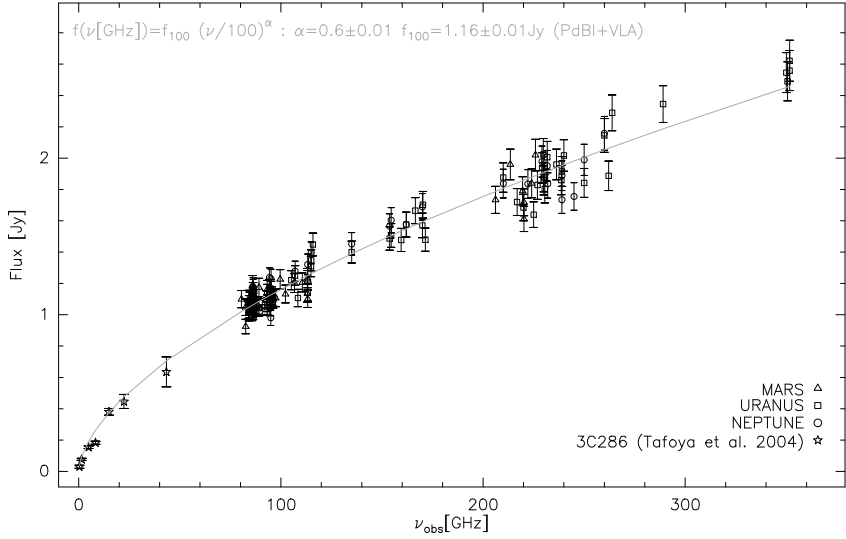


Figure 7.1: SED of MWC349A from its flux density monitoring at PdB and VLA [14]. Symbols are for primary calibrators used (Uranus, Neptune and Mars).

	flux densities (Jy)			
	A1 & A3 260 GHz	A2 150 GHz	α^1	Ref.
MWC349A	2.06 ± 0.04	1.48 ± 0.02	$+0.60 \pm 0.01$	PdB [14]
NGC7027	3.46 ± 0.11	4.26 ± 0.24	-0.34 ± 0.10	Hoare et al 1992 [16]
CRL2688	2.91 ± 0.23	0.76 ± 0.14	$+2.44 \pm 0.18$	Dempsey et al 2013 [5]

¹ Spectral index is defined as $S_\nu \propto \nu^\alpha$.

Table 7.1: Reference flux densities of secondary calibrators at the NIKA2 reference frequencies 150 and 260 GHz. Uncertainties of flux densities extrapolated at 150 and 260 GHz include contribution of the uncertainty on α .

7.3 Baseline calibration results

We test the calibration bias and statistical uncertainties using the baseline calibration method, which we recall, relies on the following main ingredients: atmospheric attenuation is corrected using the *corrected skydip* opacity correction described in Sect. 3.5 and the telescope-driven beam impact is mitigated using the *baseline* scan selection described in Sect. 2.3.7.

The calibration bias is evaluated using a series of scans of MWC349 acquired during the N2R9, N2R12 and N2R14 campaigns. Namely, we use the 72 scans that met the baseline selection criteria over the 109 available scans for MWC349. Figure 7.2 shows the bias b_A for Array 1, Array 3, the combination of the 1 mm arrays and Array 2 as a function of the atmospheric transmission. This quantity relates to the zenith opacity and the airmass as $\exp(-\tau \cdot x)$.

For the 1 mm arrays and array combination, we find calibration biases in agreement with unity within the statistical dispersion for the three campaigns, whereas a 5% lack of flux with respect to expectations is observed at 2 mm, consistently for the three campaigns. This bias has a

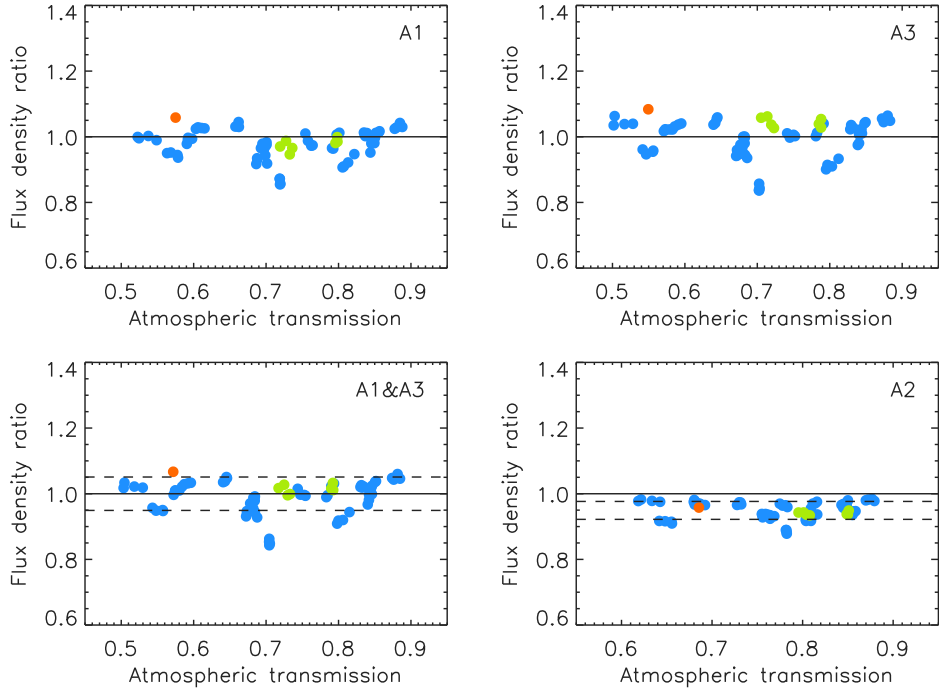


Figure 7.2: Baseline calibration bias. The measured-to-expected flux density ratio is shown as a function of the atmospheric transmission, defined as $\exp(-\tau \cdot x)$, using MWC349 scans acquired during N2R9 (blue), N2R12 (orange) and N2R14 (lime green) campaigns. Dashed lines show the flux density ratio 1σ dispersion.

low significance with respect to the absolute calibration precision of both NIKA2 (5%) and PdB. No sizable dependency of the calibration bias with the atmospheric transmission is seen. Hence we conclude that the NIKA2 photometry is assessed at the level of 5% on reference sources of about one Jy, which corresponds to the same level of accuracy as the absolute calibration errors.

We further test the calibration stability against atmospheric condition as described in Sect. 7.1. From a total of 487 scans flux-selected sources acquired during N2R9, N2R12 and N2R14, 264 met the baseline selection criteria and are used for testing stability. The first panels of Fig. 7.3 show the measured-to-median flux densities evaluated from these scans for Array 1, Array 3, the combination of Array 1&3 and Array 2 as a function of the atmospheric transmission.

In addition, the statistical calibration uncertainties are estimated using the standard deviation of the flux density ratios using all selected scans. We find uncertainties of 5.5% for A1, 6.1% for A3, 5.7% for the 1 mm band and 2.9% for A2. These 1σ statistical errors are shown as the inner dashed lines from either sides of the unity lines in Fig. 7.3, while 3σ errors are shown as the outer dashed lines.

No sizable dependency of the flux density ratio is seen within the wide range of atmospheric transmission that have been tested, which goes from 0.5 to 0.9. The flux density ratio is in general well within the 1σ errors, whereas some scans at atmospheric transmissions of about 0.7 show a mild lack of flux density with respect to the median at a significance below 3σ .

We further investigated this lack of flux in the third row of Fig. 7.3. The flux density ratio versus atmospheric transmission in the 1 mm and 2 mm bands are shown color-coded as a

function of the observation date. The scans affected by the lack of flux have all been observed either between 12:00 and 14:00 UT or between 8:00 and 9:00 UT hours, that are close to the observation date cut thresholds of the baseline selection (see Sect. 2.3.7). These scans are likely to be impacted by the telescope-driven beam broadening or by the sunrise focus drift respectively.

The last row of Fig. 7.3 shows the flux density ratio distribution at 1 and 2 mm. These consist in bulk Gaussian distributions, which correspond to the nightly observations and large distribution queues toward the low flux density ratio, due to morning observations. Gaussian fits of these distributions mainly capture the Gaussian bulk and are thus indicative of the uncertainty improvement from narrower observation date windows. We find in Fig. 7.3 that restricting the used observation dates to the 10 more stable hours (from 22 : 00 to 08 : 00 UT) would result in relative calibration uncertainties of 3.6% at 1 mm and 1.2% at 2 mm, which constitute an improvement of about 60% at 1 mm and 40% at 2 mm of the calibration uncertainties. The baseline selection, which i) retains 16 hours of observation time a day and ii) results in calibration uncertainties that meet the requirement for a millimetric ground-based instrument, constitutes an advantageous tradeoff.

Characteristics		Datasets			
		N2R9	N2R12	N2R14	Combined
Bias	# total	68	14	27	109
	# selected	64	1	7	72
	A1	0.99	1.06	0.98	0.98
	A3	1.01	1.08	1.04	1.00
	1mm	1.00	1.07	1.01	0.99
	2mm	0.95	0.96	0.94	0.95
using color corrections as of Table A.1					
Bias	# total	68	14	27	109
	# selected	64	1	7	72
	A1	0.95	1.03	0.94	0.95
	A3	0.99	1.07	1.00	1.00
	1mm	0.97	1.05	0.97	0.98
	2mm	0.95	0.95	0.93	0.95
Rms [%]	# total	303	72	112	487
	# selected	219	33	12	264
	A1	5.7	4.6	2.9	5.5
	A3	6.2	5.7	2.4	6.0
	1mm	5.9	5.0	2.5	5.7
	2mm	3.2	2.1	1.1	3.0

Table 7.2: Baseline calibration results: photometry accuracy and uncertainties. The first row gives the calibration bias b_A and the second row the calibration rms error σ_A , as defined in Sect. 7.1, using observations during N2R9, N2R12, N2R14 and the combination of the three campaigns.

As a summary, the baseline calibration results in flux densities in agreement with expectations for MWC349 at 1 mm and 5% below expectations for MWC349 at 2 mm. This bias, which has

a low significance with respect to the absolute calibration precision of both NIKA2 (5%) and PdB, will be further investigated by using other calibration methods in Sect. 7.4. Moreover, the photometry is stable against the atmospheric condition within uncertainties over a wide range of opacities. The calibration statistical errors are about 6% at 1 mm and 3% at 2 mm. All results for the baseline calibration are gathered in Table 7.2.

7.4 Comparison with other calibration methods

The baseline calibration results are compared to results drawn using other calibration methods that either resort to different opacity correction or include a photometric correction to correct for the beam impact. The ‘taumeter’ and ‘skydip’ methods are named from the ‘taumeter’ and ‘skydip’ opacity corrections described in Sect. 3.1 and Sect. 3.2 respectively. As the baseline calibration, these methods are based on the baseline selection (see Sect. 2.3.7) for discarding the scans that are the most impacted by the telescope-driven beam effect. By contrast, ‘photocorr demo’ and ‘photocorr pointing’ use the same opacity correction as the baseline method, that is ‘corrected skydip’ (see Sect. 3.5), but resort to the ‘demo’ and ‘pointing’ photometric corrections respectively, as discussed in Sect. 6.7.1. Using these ‘photocorr’ methods alleviate the need of a scan selection on the observation date: all scans that meet the mild criteria based on the atmospheric condition are included whatever the observation date at which they have been acquired.

Calibration bias

Characteristics		Methods				
		baseline	taumeter	skydip	photocorr demo	photocorr pointing
Bias	A1	0.95	0.98	0.97	0.95	0.97
	A3	1.00	1.02	1.02	0.99	1.00
	1mm	0.98	1.01	1.00	0.97	0.99
	2mm	0.95	0.95	0.95	0.95	0.95
Rms [%]	# total	487	487	487	396	396
	# selected	264	264	264	291	283
	A1	5.5	7.5	7.3	4.0	4.9
	A3	6.0	8.1	7.1	4.1	5.2
	1mm	5.7	7.9	7.1	3.8	4.9
	2mm	3.0	3.8	3.0	2.2	2.4

Table 7.3: Comparison of calibration results using five methods

We present the calibration bias (see the definition in Sect. 7.1) as a function of the atmospheric transmission for the five calibration methods in Fig. 7.4 and report the results in the row labelled ‘Bias’ of Table 7.3.

At 1 mm, all methods lead to flux density estimates in agreement with expectations within the rms dispersion. However, ‘taumeter’ ratios have more dispersion than the baseline method ratios, whereas ‘skydip’ shows some dependency on the atmospheric transmission, with a 10 to

15% excess of the flux density with respect to expectations at high transmission. These features, which are already noticeable from Fig. 7.4, will be confirmed and further discussed using more scans. On the other hand, the calibration methods based on photometric correction yield an unbiased photometry (calibration bias in agreement with the unity within the rms error) while using 30% more scans. These results are encouraging for the exploitation of scans acquired in difficult observing condition.

At 2 mm, all methods result in a similar calibration bias of 0.95 ± 0.05 . We also obtained the same 2mm-calibration biases when using scans per campaign. To summarize, the 2mm-calibration bias is stable against i) a large range of atmospheric conditions, ii) the observation campaign, iii) the opacity correction method, iv) the method to treat the beam effect. An explanation for the 5% lack of flux density toward MWC349 is probably to be sought on the side of the flux density expectations for this source. Uncertainties on the derivation of the flux density expectation comes in two flavours: firstly, the accuracy of the SED fitted from PdB and VLA observations depends on these instruments absolute calibration errors, which is roughly estimated not to be better than 5% for PdB, and secondly, the NIKA2 flux density extrapolation from interferometer data may be not straightforward for MWC349 (e.g. due to the contamination by strong masers in the radio recombination lines [15]).

Calibration uncertainties

We present the measured-to-median flux ratio versus the atmospheric transmission at 1 and 2 mm and their distribution for the five calibration methods in Fig. 7.5, and gather the derived calibration uncertainties in the row labelled 'Rms' of Table 7.3. From both these information, we conclude that the 'taumeter' method leads to statistical uncertainty increases of about 40 and 30% at 1 and 2 mm. The 'skydip' method shows less dispersion but a correlation with the atmospheric transmission. Although of a low significance (less than 3σ), this effect has motivated the development of the 'corrected skydip' method.

Comparing the flux density ratios using calibration methods with or without photometry correction in Fig. 7.5, we notice a clear difference for the bunch of N2R9 scans at an atmospheric transmission of about 0.7: whereas the flux density ratios are low for these scans in the three first methods, they are with 1σ from unity when using a photometric correction. This further validates the hypothesis that the low flux density of these scans is due to telescope-driven beam effect, as assumed in Sect. 7.3. This also constitutes an example of the calibration improvement obtained from resorting to a photometric correction.

Moreover, results based on the 'photocorr demo' method show that calibration uncertainties as low as 3.8 and 2.2% at 1 and 2 mm are within the reach of NIKA2 without rejecting any observation dates. However, we recall this method relies on accurate beam estimates. Using the 'photocorr pointing', which is the practical case, still decreases the calibration uncertainties w.r.t. the baseline results but by a factor of about 20% in both bands. By inspecting the appropriate panels of Fig. 7.5, we notice some differences between the flux density ratios from 'photocorr demo' and 'photocorr pointing', which are likely to be due to the photometry correction noise when monitoring the beam from pointing scans. We conclude that more control on the beam monitoring is needed before proposing a calibration based on photometry correction as the nominal method.

Summary

Amongst the methods that rely on the baseline scan selection to mitigate the beam effect, the baseline method shows the best performance in terms of calibration bias and uncertainties.

The lack of flux density at 2σ significance that was observed for a small fraction of the N2R9 scans is confirmed to be due to the telescope-driven beam effect.

Methods that rely on a photometric correction lead to good calibration results: the calibration biases are in agreement with calibration biases of the baseline method, while calibration uncertainties as low as 3.8 and 2.2% have been obtained without selecting the scans on the observation date basis. However, the practical method (a. k. a. ‘photocorr pointing’) yields slightly larger rms errors than the demonstration method (a. k. a. ‘photocorr demo’), indicating an impact of the noise induced by the beam monitoring with pointing scans. More extensive robustness tests and better control of the error induced by the beam monitoring are thus needed before routinely using the Photocorr Pointing method. By contrast, the baseline method allies good performance and robustness.

Draft

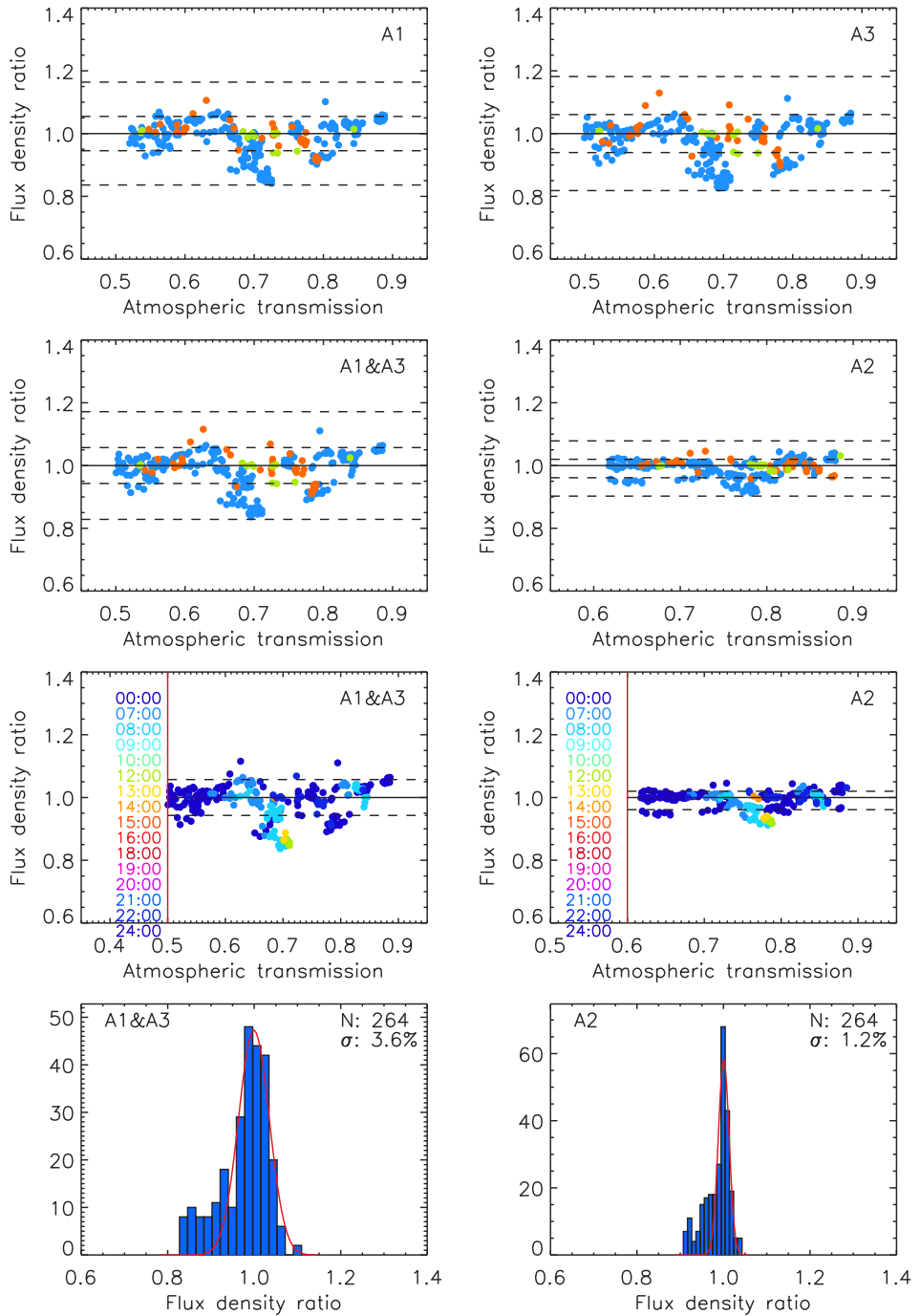


Figure 7.3: Baseline calibration uncertainties. The four first panels shows the measured-to-median flux density ratio of bright sources vs atmospheric transmission using the baseline calibration for Array 1 (A1), Array 3 (A3), the combination of A1&A3 and A2. Blue points are N2R9 scans, orange points N2R12 and lime green points N2R14. The dashed lines from either sides of the unity-ratio line show the 1σ (inner lines) and 3σ (outer lines) errors. The third row panels are copies of the 'A1&A3' and the 'A2' panels color-coded from the UT observation time of the scans. Lower flux ratio datapoints correspond to scans acquired after 8:00 UT hours. Flux density ratio distributions for A1&A3 and A2 are plotted in the fourth row panels. The Gaussian fits of this distribution, plotted in red, mainly capture the bulk of night-time observation scans, as seen on the plot of the panel above, indicating the impact of scans acquired after 8:00 UT on the calibration uncertainties.

Draft

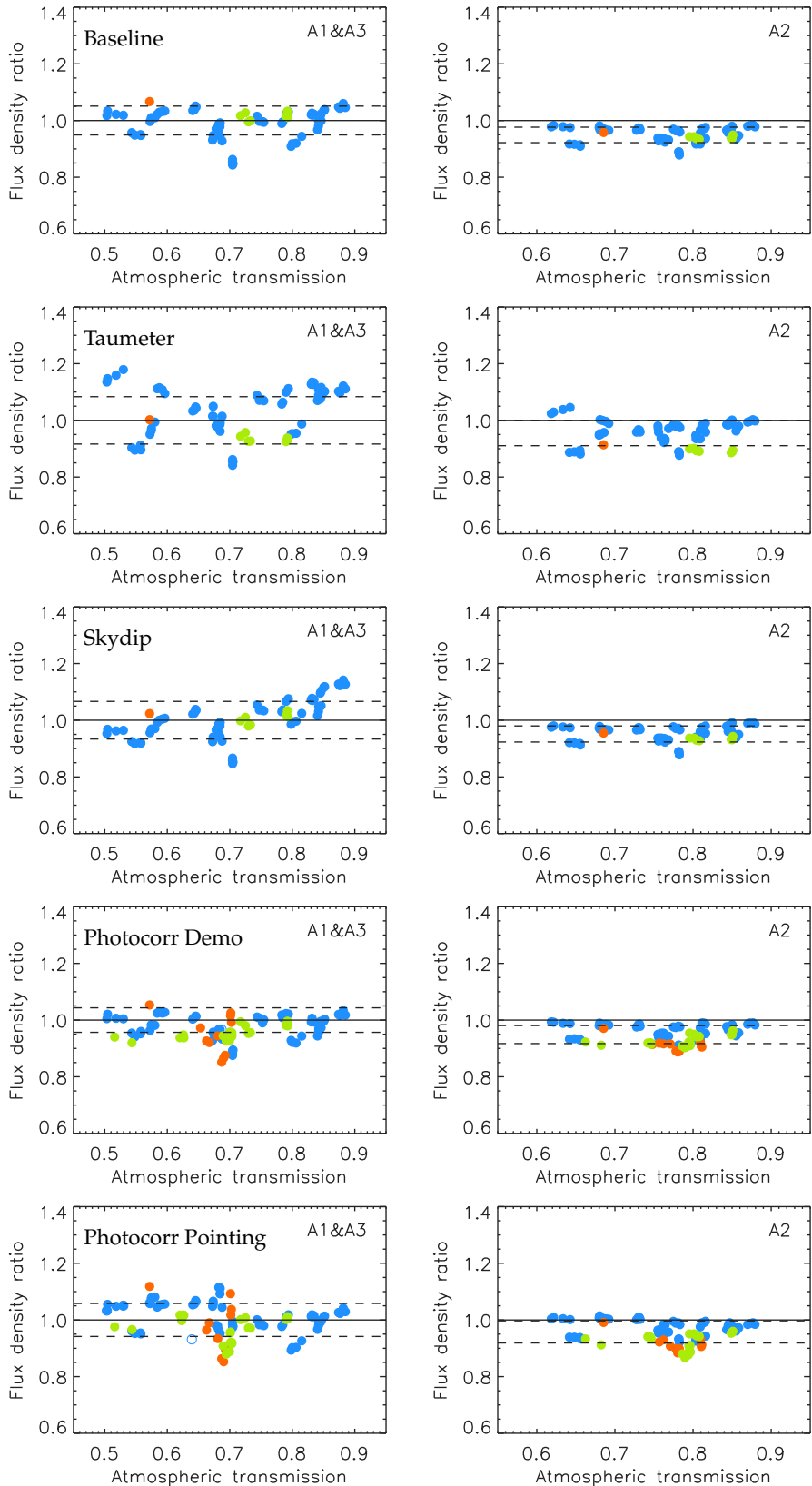


Figure 7.4: Comparison of the calibration bias for five calibration methods. The measured-to-expected flux density ratio is shown as a function of the atmospheric transmission for the baseline method (first row) as well as for methods using the 'taumeter' (second row) and 'skydip' (third) opacity correction, and for methods resorting to the 'demo' (fourth) and 'pointing' (fifth) photometric correction. Dashed lines show the flux density ratio 1σ dispersion.
86

Draft

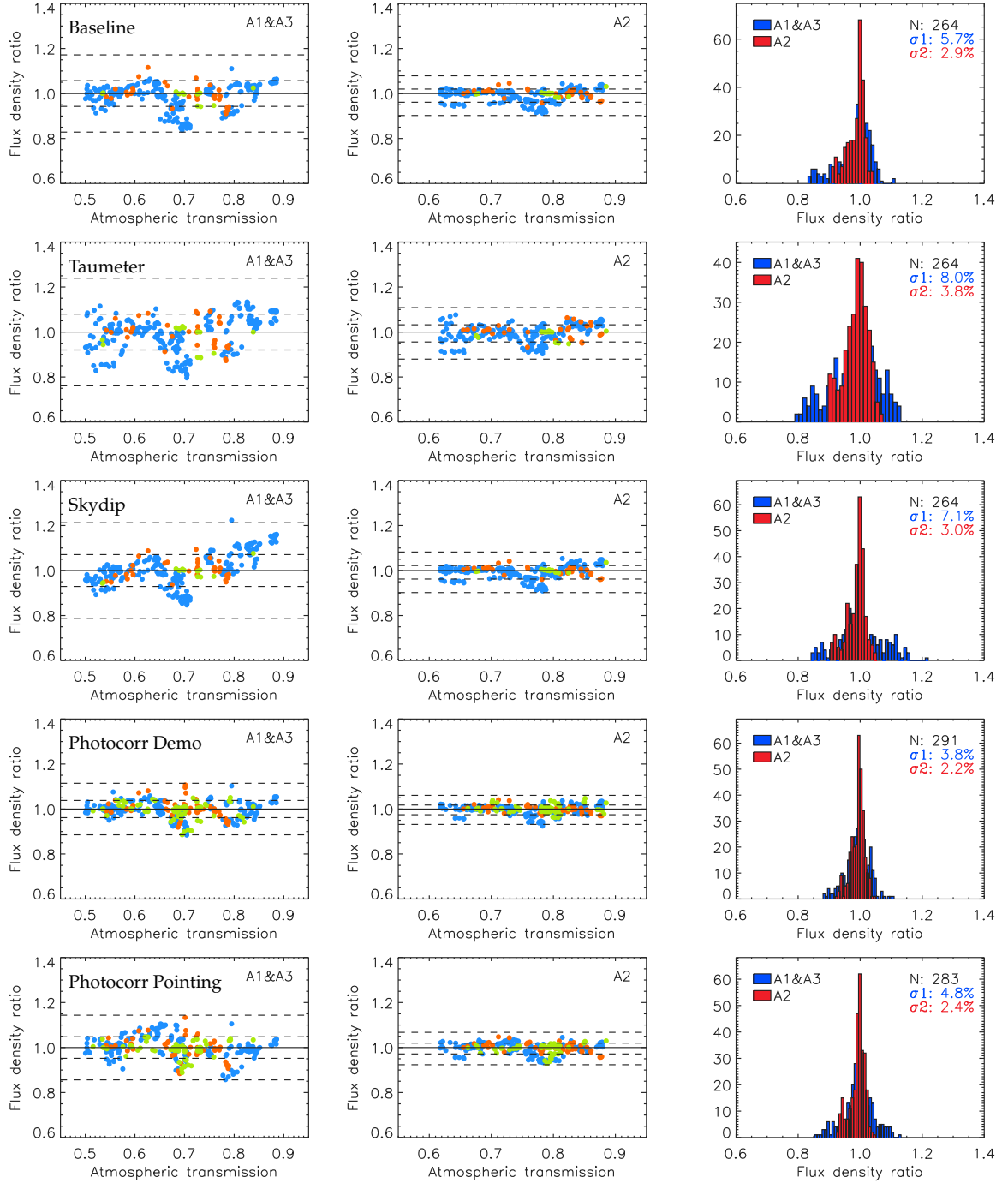


Figure 7.5: Comparison of the calibration uncertainties for five calibration methods. The measured-to-median flux density ratio at 1 mm (first column) and 2 mm (second column) of bright sources vs atmospheric transmission are shown as well as the flux density distributions, using (first row) the baseline calibration, methods relying on (second row) the 'taumeter' and (third row) the 'skydip' opacity correction, and methods resorting to (fourth) row the 'demo' and (fifth row) the 'pointing' photometric correction.

Chapter 8

Sensitivity

In Sect. 2.2.4, we have introduced the TOI properties of the instrument and our reference data reduction scheme. We here go up to the final maps while considering the time spent observing to derive the sensitivity of the instrument, a. k. a. the *Noise Equivalent Flux Density*, (NEFD).

The MoU defines the NEFD: *The Noise Equivalent Flux Density (NEFD) is the 1σ sensitivity in one second of effective on-source telescope integration time after the absolute calibration has been performed (i.e. after beam efficiency and opacity corrections). It is appropriate for 2 mm of precipitable water vapor (pwv) content in the atmosphere and 60 degrees elevation source. It refers to the inverse variance of the noise on the flux measurement of a point-source, averaged over the valid receiver pixels.*

IRAM has its own time estimator for astronomers that will compute the “effective NEFD”, provided we give the “detector NEFD” and a fraction of valid KIDs η . To derive the detector NEFD, we must clearly define the “detector time of integration” and relate it to the “time of observation” which is the time actually spent by an astronomer at the observing desk. Going from the intuitive understanding of the time of integration to its actual value is not as trivial as it seems because of the dependence on the scanning strategy and the distribution of valid KIDs across the FOV.

8.1 Estimating the time of integration

8.1.1 Time of integration from the density of samples

Let’s take a map of resolution r (arcsec) and consider the map pixel that is centered on the position where we estimate the flux uncertainty σ_ϕ . The number of hits in this pixel $N_h(r)$ allows us to define a time of integration on this pixel via the sampling frequency ν

$$t_{pix} = N_h(r) / \nu \tag{8.1}$$

To estimate how much wall clock time was necessary to the entire matrix to produce this density of samples, we need to account for how many KIDs, on average, contribute to $N_h(r)$ at the same time, that is to say the average number of KIDs per map pixel. Indeed, if the pixel is large enough to contain n KIDs at each time, the number of samples in this pixel will be n times larger for the same time of observation. The same is true if we combine A1 and A3 for instance.

We therefore note S the surface of the FOV, g the distance between adjacent KIDs and note that $S = N_{pix} \times r^2 = N_{kids} \times g^2$. The number of KIDs per pixel of r arcsec resolution is thus r^2/g^2 , so the actual observation time reads

$$t_{det} = t_{pix} \frac{g^2}{r^2} = \frac{N_h(r)}{\nu} \frac{g^2}{r^2} \quad (8.2)$$

For the combination of arrays 1 and 3, the number of KIDs per pixel is the sum of the two contributions that impact the number of KIDs per pixel:

$$t_{det}^{1mm} = \frac{1}{2} \frac{N_h^{1mm}(r)}{\nu} \frac{g^2}{r^2} \quad (8.3)$$

So finally, if σ is the uncertainty on the flux estimate, the detector NEFD reads

$$NEFD_{det} = \sigma_\phi \sqrt{t_{det}} \quad (8.4)$$

To relate it to the effective “observer” NEFD, we must account for the fraction of valid pixels actually used to derive the map. Indeed, the integration time per pixel goes like η for the same observation, thus:

$$NEFD_{det}^{eff} = \sigma_\phi \sqrt{t_{det}/\eta} \quad (8.5)$$

which in turn translates into a time requirement to reach the same level of integration:

$$t_{det}^{req} = \left(\frac{NEFD_{det}}{\sigma_\phi} \right)^2 \frac{1}{\eta} \quad (8.6)$$

8.1.2 Time of integration from the matrix footprint

One can also think of the “time spent on the source”, for a full matrix (ie. all valid KIDs), as the time when the source is inside the circular footprint of the matrix. During a scan, it’s easy to count how much time the source is at a distance from the FOV center that is smaller than the FOV radius. This time, t_{geom} is a direct estimate of the time “at the desk”, so it enters the definition of effective NEFD, not the detector NEFD, hence:

$$NEFD_{geom}^{eff} = \sigma_\phi \sqrt{t_{geom}} \quad (8.7)$$

Fig. 8.1 compares ηt_{geom} to t_{det} and shows the good agreement between the two. Because the definition of t_{det} is more straightforward in terms of measurement from the map and design parameters and does not require an approximate determination of the FOV radius, it is *our reference time estimator*.

8.2 NEFD estimation methods

With the uncertainty on flux measurements as described in Sect. 7 and now an estimator of the time of integration, we have everything in hand to derive the NEFD. We have devised several ways to estimate it at the same time as checking the good behaviour of the instrument. Two methods are based on deep integrations on a source, one is based on the joint analysis of multiple scans without combining them:

Draft

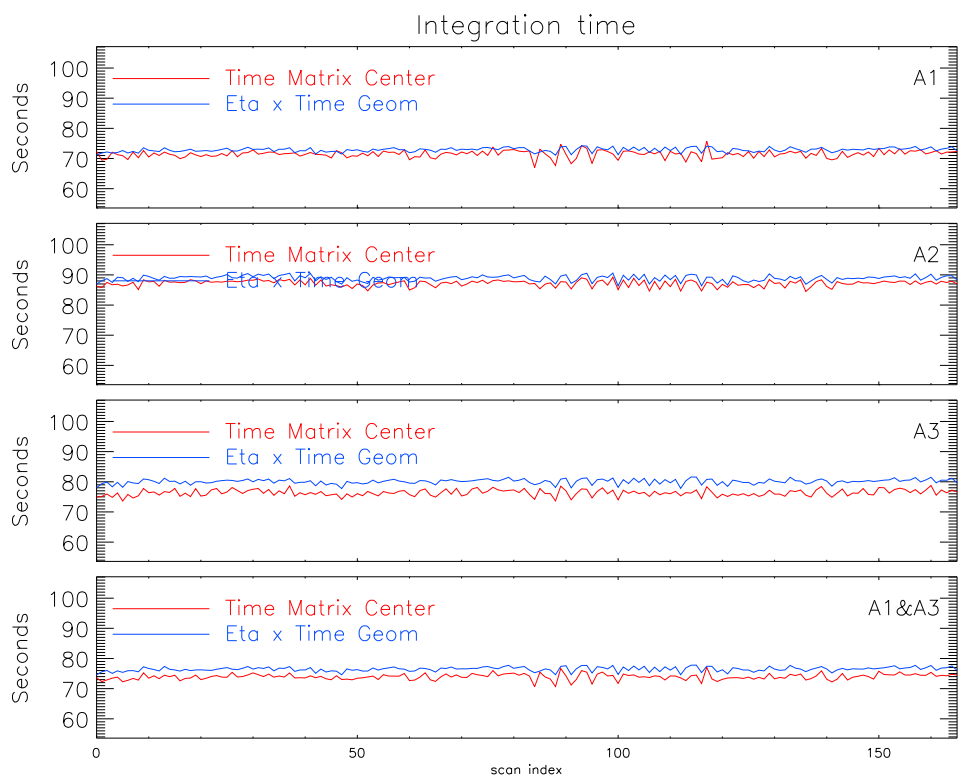


Figure 8.1: Comparison between two estimators of the time of integration on HLSJ0918+5142 during Run 9 for FOV diameter of 6.2 arcmin. The difference goes from 2% to 5%, hence translating into a NEFD relative difference of 1 to 2.5%.

1. **Deep Integration method 1:** the error on the flux of a point source for an integration time t is $\sigma = NEFD / \sqrt{t}$. Co-adding several scans of the same source and fitting σ as a function of the square root of the time of integration must therefore give a straight line whose amplitude is the NEFD if correctly corrected for the different elevation and opacity conditions of observations.
2. **Deep Integration method 2:** by summing a large and even number of scans with alternative positive and negative weights, we cancel the signal while keeping the noise properties. This final “Jackknife” map can then be analyzed to provide estimates of flux uncertainties for a the effective time of integration, hence giving an alternate estimation of the NEFD.
3. **Scatter method:** analyzing each scan in terms of sensitivity and time of integration, we have an NEFD per scan that varies with opacity and elevation. Fitting the distribution of measures against $\exp[\tau / \sin \delta]$ provides the zenith opacity.

In this section, we use two data sets from Runs 9 and 12.

For Run 9, HLSJ0918+5142 is moderately faint source [3], expected to be 74.5 mJy at 1mm and 15.7 mJy at 2mm (M. Bethermin, private communication). This source was chosen for its flux and its availability during Run9 for long integration. It has been observed for about 9 h in total over three nights. The scans were 8x5 arcmin², alternatively oriented in (ra,dec), (dec,ra), (az,el), (el,az).

For Run 12, G2 has become the nickname of an empty target close to sources known to IRAM but not to the commissioning team in order to check our source detection capabilities blindly.

The data were processed according to sect. 2.2.

8.2.1 Deep integration method 1: $\sigma = NEFD / \sqrt{t}$

We co-add the scans one by one and each time perform a photometric analysis on the map according to Sect. 7. The uncertainty on the flux at the center of the field (on source in the case of HLSJ0918+5142, off source in the case of G2) is plotted and fitted against $\sqrt{t_{\text{det}}}$. It should go like a straight line if scans were all taken in the exact same conditions and stacked with equal weights. In practice, the weights are sensitive to the conditions of observations, namely the elevation and opacities (see Fig. 8.2 and they must be accounted for. The uncertainty on the central flux reads

$$\sigma = NEFD_{\text{det}} \times e^{\tau / \sin \delta} t^{-1/2} \quad (8.8)$$

Because scans are coadded with inverse variance weighting, the combined flux is

$$\phi = \frac{1}{\sum_n 1/\sigma_n^2} \sum_n \frac{\phi_n}{\sigma_n^2} \quad (8.9)$$

whose variance is

$$\sigma^2 = \frac{1}{\sum_n 1/\sigma_n^2} \quad (8.10)$$

which, according to Eq. (8.8) becomes

$$\sigma^2 = \frac{NEFD_0^2}{\sum_n t_n e^{-2\tau_n / \sin \delta_n}} \cdot \quad (8.11)$$

Draft

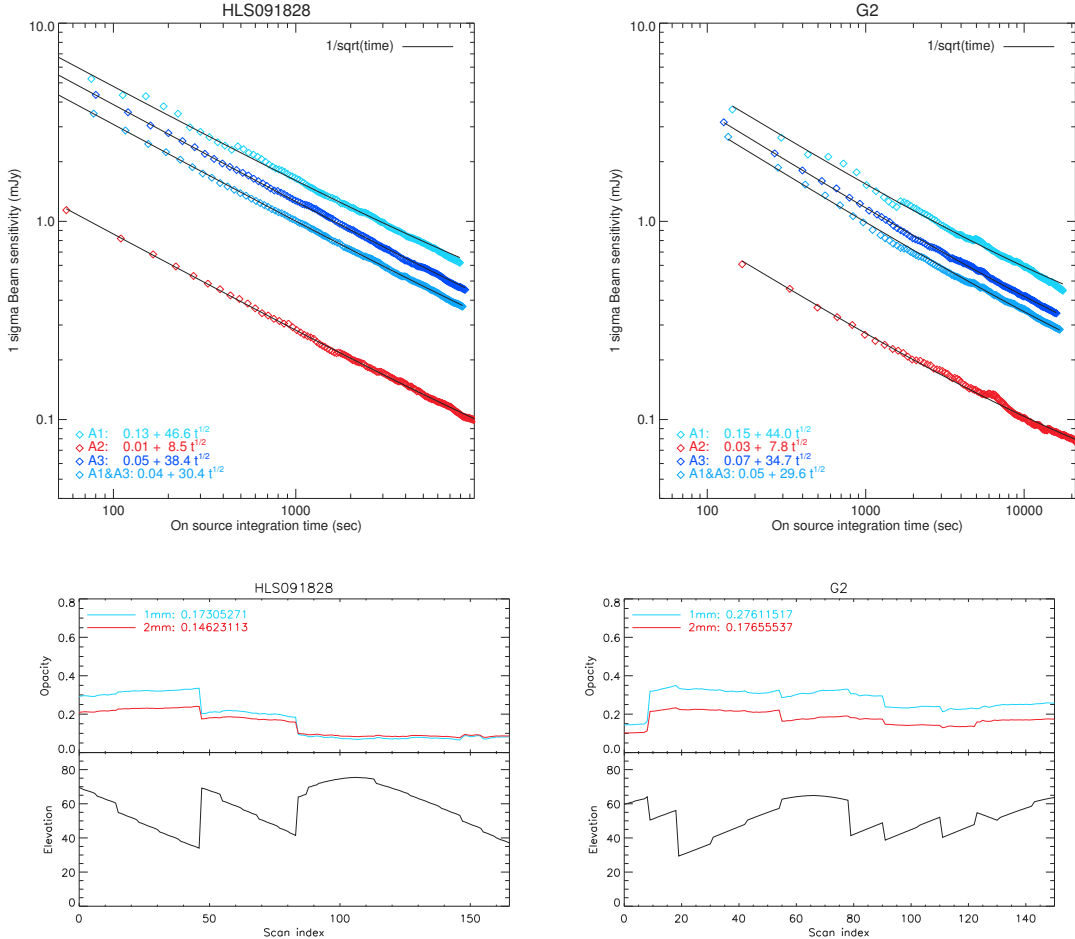


Figure 8.2: Top row: 1σ sensitivity on the measure of the flux of a point source vs the time of integration on this source in two cases. The sensitivity goes like $t^{-1/2}$ as expected. Bottom row: Opacities and elevations of the scans used in this analysis.

If the opacity and the elevations are the same for all scans, we recover the integration like \sqrt{t} . In general, if the observing conditions vary, we must fit the integrated sensitivity vs the effective time $\sum_n t_n e^{-2\tau_n / \sin \delta_n}$ in order to recover an unbiased estimate of $NEFD_0$. The method was applied to HLS J0918+5142 and G2, results are summarized on Fig. 8.2 and in Tab. 8.1.

8.2.2 Deep integration method 2: Jackknife

With enough scans of the same source, it is possible to alternate addition and subtraction of the scans and therefore cancel the contribution of the signal to the final combination, while preserving the noise properties. This method is often referred to as “Jackknife” and is a powerful test for residual systematics. The Jackknife maps of HLS J0918+5142 and G2 are presented on Fig. 8.3. Photometry at their center provides estimates of the zenith NEFD that are reported in Tab. 8.1.

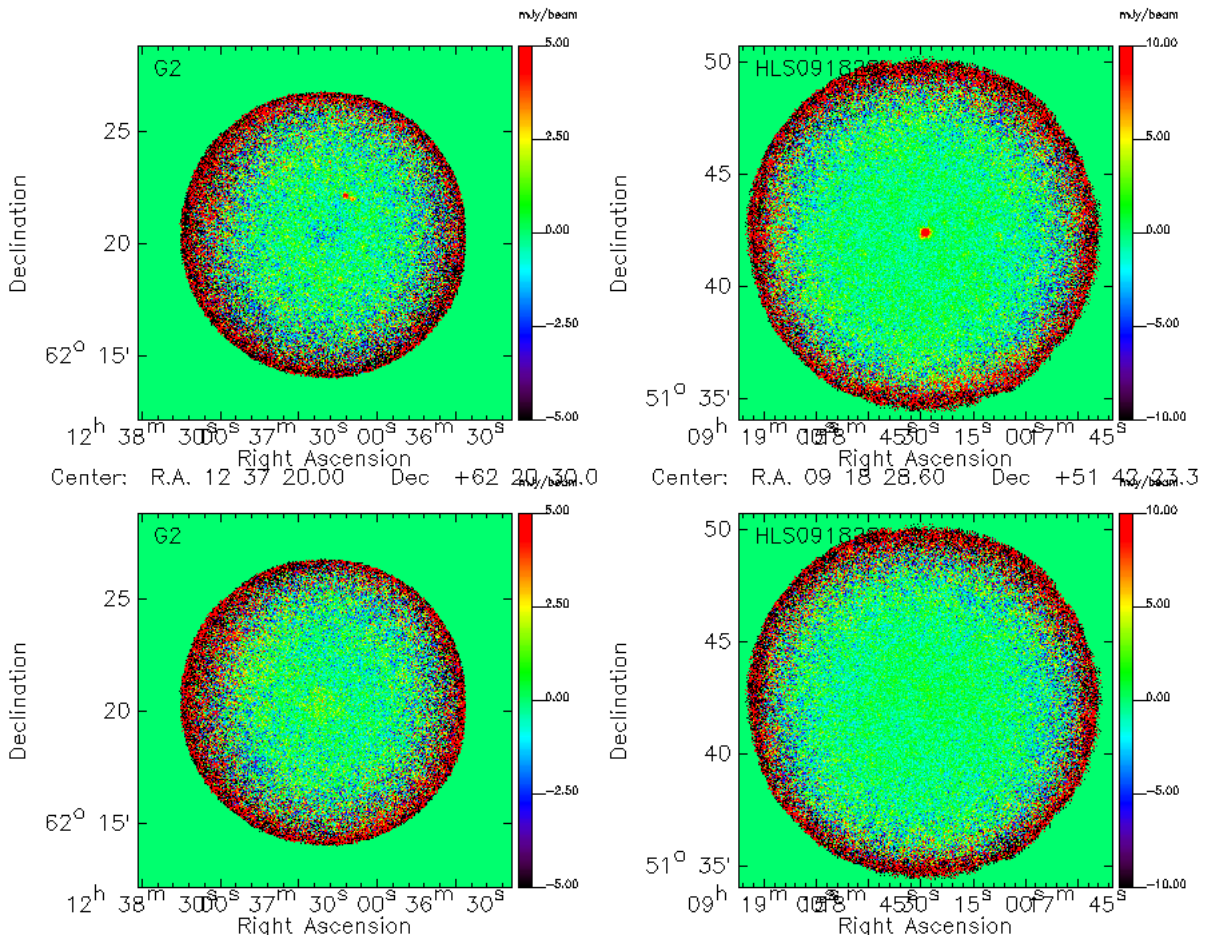


Figure 8.3: Top row: Maps of HLS J0918+5142 and G2 at 1mm. Bottom row: Jackknife maps :After the sum of scans with alternative positive and negative weights, signal residuals are negligible while noise properties are preserved.

8.2.3 NEFD per scan vs $e^{\tau/\sin\delta}$: Scatter

Performing photometry on each individual scan on G2 or HLS J0918+5142, we can estimate the sensitivity on the central flux and measure the time of integration, hence derive the NEFD for this scan. This determination is intrinsically noisier than the two previous maps because of the variance associated to each scan. However, taken altogether, the scans provide another estimate of the instrument NEFD. Results are presented on Fig. 8.4 and the derived zenith NEFD are given in Tab. 8.1.

While the two first methods require long integration on the same source, this *scatter* method can be used on all scans. In practice, noise characterization may be biased by residuals of a strong source and the instrument far side lobes (Fig. 8.5). We therefore restrict to sources with a flux below 1Jy. Fig. 8.6 further shows the comparison between runs N2R9, N2R12 and N2R14 and their consistency.

Combining the data set of N2R9, N2R12 and N2R14 campaigns, more than one thousand observations scans of sub-Jy sources meet the baseline selection criteria (see Sect. 2.3.7), providing

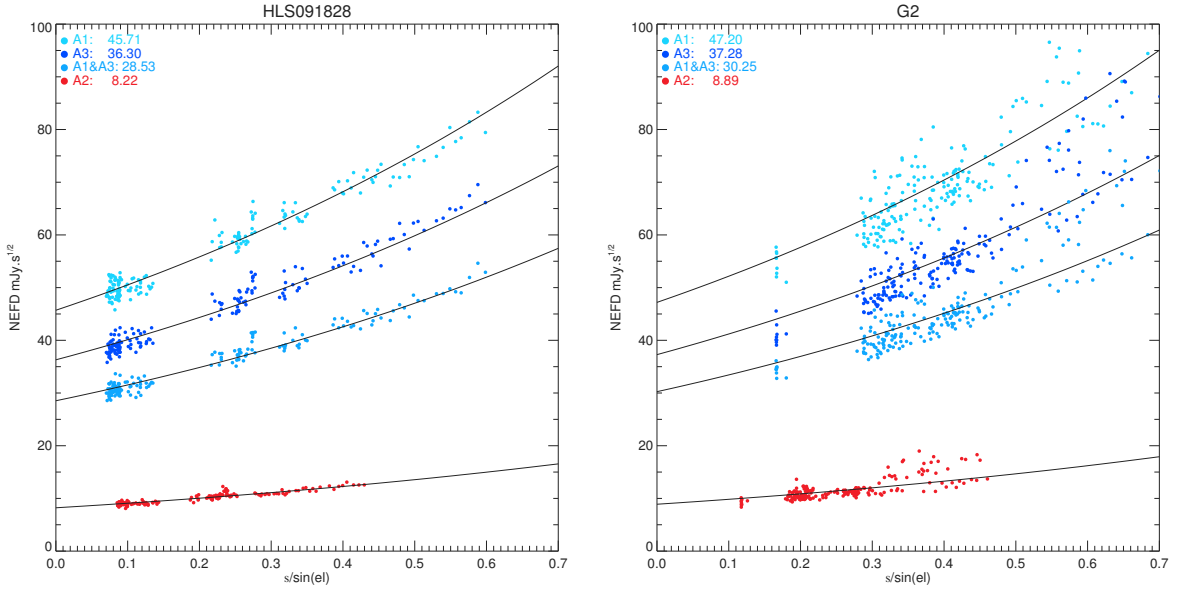


Figure 8.4: 1σ sensitivity on the central flux for each observation of G2 and HLS J0918+5142. The solid black line is the theoretical fit of $\sigma = \sigma_{ref} e^{\tau/\sin\delta}$ and gives the zenith NEFD when extrapolated to $\tau/\sin\delta = 0$.

us with robust NEFD estimates that are representative of average NIKA2 performance, which are gathered in Tab. 8.2. The zenith NEFD and RMS uncertainties are evaluated as the median and the scatter of the individual NEFD corrected with $\exp[\tau/\sin(\delta)]$. These values are then extrapolated at the reference IRAM observing conditions, which consists of 2 mm of precipitable water vapor (pwv) in the atmosphere and 60 degrees elevation.

To further estimate the mapping capabilities, we also evaluate the mapping speed m_s , which is defined as the sky area that is covered in one hour of observation to a noise level of 1 mJy, using

$$m_s = \frac{\pi}{4} d_{\text{FoV}}^2 \frac{\eta}{\text{NEFD}^2}, \quad (8.12)$$

where $d_{\text{FoV}} = 6.5'$ is the FoV diameter and η the fraction of valid KIDs, as given in Tab. 4.1 in Sect. 4.1. The zenith mapping speed that is extrapolated at zero opacity, and the astronomer mapping speed that is extrapolated at the reference IRAM observing conditions are given in Tab. 8.2.

Draft

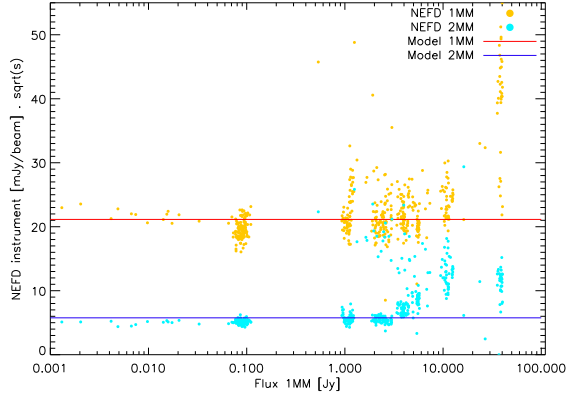


Figure 8.5: Measured NEFD versus source flux for N2R9 at 1 and 2 mm

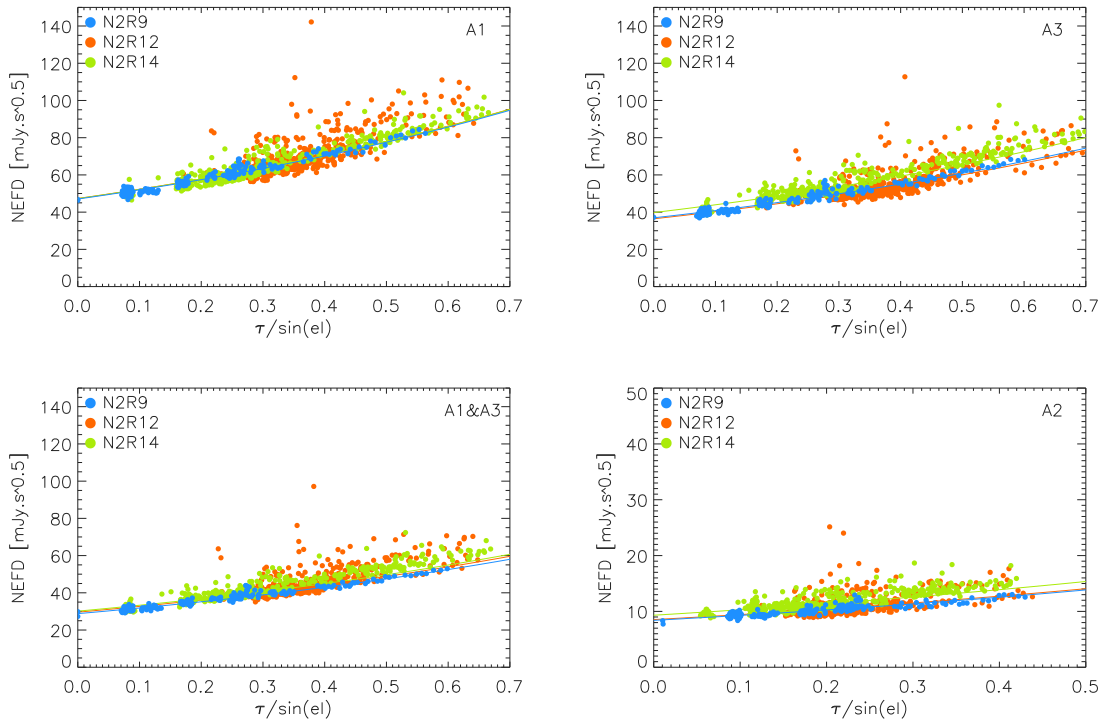


Figure 8.6: Measured NEFD as a function of atmospheric background for array 1 (upper left), array 3 (upper right), the 1 mm (lower left) and 2 mm (lower right) channels. Datapoints are NEFD estimates in $\text{mJy}\cdot\text{s}^{1/2}$ for N2R9 (blue), N2R12 (orange) and N2R14 (chartreuse). We also show in the plots the expected NEFD evolution with atmospheric background as solid curves.

		HLS J0918+5142	G2	<1 Jy			
				N2R9	N2R12	N2R14	Combined
<i>Scatter</i>	A1	45.7	47.2	47.0	47.3	47.3	47.2
	A3	36.3	37.3	36.9	36.4	39.8	37.9
	A1&A3	28.5	30.3	28.8	30.2	30.9	30.1
	A2	8.2	8.9	8.4	8.5	9.3	8.8
<i>Jackknife</i>	A1	48.1	52.1				
	A3	37.5	38.8				
	A1&A3	29.0	32.2				
	A2	8.9	10.9				
$t^{-1/2}$	A1	46.6	44.0				
	A3	38.4	34.7				
	A1&A3	30.4	29.6				
	A2	8.5	7.8				

Table 8.1: NEFD's in $\text{mJy}\cdot\text{s}^{1/2}$ for the three methods described in the text and obtained on G2, HLS J0918+5142, and all sub-Jy sources of runs N2R9, N2R12, N2R14. The results given in the last column are based on more than a thousand scans, which distribute as 202, 481 and 430 scans of N2R9, N2R12 and N2R14 respectively.

<1 Jy	A1	A3	A1&A3	A2
NEFD ₀	47.2	37.9	30.1	8.8
RMS NEFD ₀	3.9	3.5	2.9	1.1
$m_s^{(0)}$	45	70	111	1388
NEFD _A	56.6	45.6	36.1	9.8
RMS NEFD _A	4.7	4.2	3.5	1.2
$m_s^{(A)}$	31	48	77	1119

Table 8.2: Median NEFD and rms uncertainties in $\text{mJy}\cdot\text{s}^{1/2}$, as well as the derived mapping speed in $\text{arcmin}^2 \cdot \text{mJy}^{-2} \cdot \text{h}^{-1}$, evaluated in using the scatter method on all sub-Jy sources of runs N2R9, N2R12 and N2R14, given at zenith (first two rows) and extrapolated at the reference IRAM observing conditions (last two rows), which are defined as 2 mm pwv and 60 degrees elevation.

Chapter 9

Performance of NIKA2 at the IRAM 30 m telescope

Scope & objectives

NIKA2 performance in intensity have been assessed, as defined in the MoU, after the end of the commissioning in intensity (phase 1). This commissioning phase ended with the April 2017 technical campaign, which included a science verification phase, and was officialised at the ‘End-of-commissioning’ review that took place at the IRAM in September 2017. This document, which comes along with the instrument delivery, presents the performance, as well as the methods that we have developed for their assessment and the robustness tests we performed.

Data set

The performance assessment is based on observations acquired at the February 2017 technical campaign (a.k.a. N2R9), during which NIKA2 instrumental set-up was in final configuration for the first time, and on observations taken during the first science pools of October 2017 (a.k.a. N2R12) and January 2018 (a.k.a. N2R14). Data acquired during April 2017 technical campaign (a.k.a. N2R10) were not considered for the sensitivity assessment due to extra noise induced by an end-of-life turbo pump, which disappears once the turbo pump was replaced. The considered data set allow us to check the performance stability for one year and a large range of atmospheric conditions.

Methods

The performance assessment utilizes an IDL-based data reduction pipeline that was internally developed in the NIKA2 collaboration to go from raw time-ordered data to calibrated maps. We give a synthetic description of the entire pipeline in Sect. 2.2 for the reader convenience. The calibration and performance assessment methods are briefly presented in Sect. 2.2 and further detailed in Chapters 3 to 8, which are summarized below.

In Chapter 3, the atmospheric attenuation is corrected using two-step method: first, the line-of-sight opacity of each observing scans is estimated using a series skydip observations performed with the NIKA2 instrument, then a correction coefficient is applied to the skydip opacity to ensure the flux density stability against the atmospheric condition. Opacity derivation based on the resident IRAM taumeter measures is also tested for consistency checks.

In Chapter 4, *beammap* scans are used to derive the position of each KIDs in the FoV and perform a first selection to discard noisy and cross-talking KIDs. The KIDs are further selected on the comparison between their measured position and the expected designed position. Finally, series of defocused *beammap* scans are used to reconstruct the focus surfaces and estimate the telescope focus setting that optimizes the focus across the arrays.

In Chapter 5, noticeable features of the beam pattern are identified using *beammap* scans. Radial profiles of the full beam are measured up to a radius of $180''$ and are fitted using a three-Gaussian model. The main beam of each array is evaluated using three complementary methods: the first Gaussian that best fits the full beam profile, a single Gaussian fit on a side-lobe-masked version of the profile and a 2D Gaussian fit on a side-lobe-masked version of the beam map. Then we use the knowledge we have gained on the full beam and main beam to derive the main beam efficiency up to $180''$. A more precise description of the beam pattern above $180''$, which is useful for diffuse emission studies, is left for a future dedicated study that will be conducted as part of the diffuse emission NIKA2 Large Programs.

Chapter 6 deals with all the aspects related to the calibration. Sections 6.1 and 6.2 describe the reference photometric system that has been adopted: flux densities rely on a fit of a Gaussian with a fixed FWHM at reference values and are given at reference frequencies. However, we also tested a method based on aperture photometry and reported the conversion coefficients between the point-source and aperture photometry calibration in Sect. 6.8. The main primary calibrator is Uranus, although Neptune is also considered. In Sect. 6.3, the flux expectations for the primary calibrators are derived using the Moreno model, which is precise at a 5% level. In Sect. 6.4, the KID-to-KID relative calibration is performed as part of the FOV reconstruction using the fixed-Gaussian fit on individual maps per KID, which are projected from *beammap* scans. We test the stability of the KID response across the FoV by considering both flat fields toward point sources (a.k.a. main beam flat fields) and flat fields of the atmosphere (a.k.a. forward beam flat fields). Section 6.5 deals with the well-known effect of the telescope heating during the afternoon. This induces a widening of the beam, which comes along with a drop of the measured flux densities. We use calibration observations to determine the most impacted UT hours of the day. The baseline calibration, as presented in Sect. 6.6, is drawn from scans acquired between 22:00 and 9:00 UT and between 10:00 and 15:00 UT hours, whereas the Sun-rising and afternoon scans are discarded. However, in Sect. 6.7, we also tested a calibration method which resorts to a photometric correction to retrieve robust flux density estimates while the beam experiences instabilities. This method, which is based on a monitoring of the beam size throughout an observation campaign, demands dedicated scans to be made on an hour basis to reach science-grade level of accuracy and robustness. We present a test case based on a beam monitoring using the pointing scans, which yields promising results but a mild lack of robustness. Thus, we choose to base the sensitivity assessment on the baseline calibration only.

The accuracy and stability of the photometry are treaded in Chapter 7. We define two calibration performance criteria: first we measure the ratio between the measured flux density and the expectations for MWC349, a secondary calibrator which is monitored at Plateau de Bure, and secondly we estimate the rms errors with respect to the median flux density using a series of bright point-like sources. This latter criterion provides us with an estimate of the statistical uncertainties of the calibration, whiwh includes errors sourced by the dispersion in the observing conditions (atmosphere, elevation, source brightness, integration time, etc.) and in the data analysis.

In Chapter 8, we characterise NIKA2 sensitivity by estimating the Noise Equivalent Flux

Density (NEFD). We developed three complementary methods that differ in the measurement of the flux density variance but rely on the same estimate of the on-source integration time. The first method is based on fitting the variance decrease with the integration time, the second utilizes statistically equivalent data splits to produce a noise map estimate and the third method resorts to measuring the noise far from the source. Regarding the integration time, we ensure the robustness of the estimate by cross-checking the results of two approaches: integration times directly derived from the sample counts are compared to integration time estimates with the array footprint that best account for the scan strategy.

Results

All the designed KIDs detect the signal at least in some observation scans. We conservatively retain only the most stable KIDs, which are immune to the cross-talking effect and yield good signal-to-noise measurement. We defined 'valid' KIDs as the detectors that have been retained in at least two independent KID selections, as discussed in Sect. 4.1. We report valid KID fractions of 84% for the 1 mm channel arrays and 90% for Array 2. The other KIDs, which do not meet the validity criterion, are randomly distributed across the FoV, so that the whole 6.6 arcmin FoV is covered. Considering the designed KID grid as discussed in Sect. 4.2, the distance between neighbour KIDs is 9.8'', 9.7'' and 13.3'' for Array 1, 3 and 2 respectively, which defined an occupation surface per KID.

The area covered by all KIDs is in turn associated to a measured total FoV of 6.6 arcmin. diameter for each array.

While the full beam pattern presents a complex structure as discussed in Sect. 5.1, the main beam is well described with a 2D Gaussian of FWHM of 11'' for the 1 mm channel arrays and 17.6'' for Array 2, with uncertainties of 0.2'' for the combination of Array 1&3 and for Array 2, as presented in Sect. 5.2.3. Comparing the main beam fit to the measured full beam, we derive the main beam efficiency up to a radius of 180''. We find beam efficiencies of $55 \pm 3\%$ at 1 mm and $77 \pm 2\%$ at 2 mm. These meet the expectations for an instrument that does not resort to feed horns. The chosen 180'' cutting radius ensures an accurate measure of the beam patterning using a single *beammap* scan. However, dedicated studies based on the Lunar edge observations showed that a sizable fraction of the full beam stems from beyond this radius. This fraction is about 35% at 1 mm and about 20% at 2 mm (using Kramer et al 2013). Using individual map per KID, we evaluate the rms dispersion of the main beam FWHM across the FoV, as discussed in Sect. 5.2.4. We measured rms dispersions of about 0.6'' at both wavelengths using N2R9 data. These constitute a conservative estimate since the rms dispersion has been further improved by optimizing the telescope focus settings from N2R12 on.

We evaluated the statistical calibration uncertainties using 264 scans of N2R9, N2R12 and N2R14, toward sources above one Jy and selected on the observing UT hour basis, as discussed in Sect. 7.3. We find rms calibration uncertainties of about 6% at 1 mm and about 3% at 2 mm, which are state-of-the-art performance for instrument operated at these wavelengths.

The noise well integrates as the square root of the integration time for series of scans acquired in similar observing conditions as discussed in Sect. 8.2.1. The NEFD estimates reported in Table 9.1 are based on more than one thousand scans acquired during N2R9, N2R12 and N2R14, and thus constitute conservative estimates that encompass a large range of observing conditions, as addressed in Sect. 8.2.3. However, better NEFD have been found using homogeneous series of about one hundred scans of e.g. HLSJ0918+5142 as reported in Table 8.1. The conservative

NEFD estimate reaches the goal value at 2 mm. However, it is measured as slightly above the specifications at 1 mm.

We have identified several areas of improvement that will make NIKA2 more sensitive at 1 mm: 1) change the dichroic element (one of the 1 mm polarization components (A1) is absorbed more than the other (A3) with the present dichroic), 2) improve the data processing and in particular the noise decorrelation methods, 3) upgrade the 1 mm arrays, 4) increase the bandwidth of the 1 mm arrays, and 5) upgrade the surface of the telescope.

NIKA2 mapping capabilities are better estimated by evaluating the mapping speed, which is defined as the sky area that is covered in one hour of observation to a noise level of 1 mJy. NIKA2 mapping speed is an order of magnitude better than the previous generation of the IRAM 30 mm resident instruments.

The main measured parameters that define the measured NIKA2 performance are gathered in Table 9.1.

	Array 1	Array 3	Array 1&3	Array 2	Reference
Reference Wavelength [mm]	1.15	1.15	1.15	2.00	
Reference Frequency [GHz]	260	260	260	150	Sect. 6.1
Central Frequency [GHz]	255.5	257.8		151.6	Sect. 2.1.2
Bandwidth [GHz]	47.8	45.7		42.1	
Number of designed detectors	1140	1140		616	Sect. 2.1.4
Number of valid detectors	952	961		553	Sect. 4.1
Fraction of valid detectors [%]	84	84		90	
Pixel size in beam sampling unit ^a [$F\lambda$]	1.11	1.10		0.87	
FWHM ^b [arcsec]	11.1 ± 0.2	11.0 ± 0.2	11.1 ± 0.1	17.6 ± 0.1	Sect. 5.2.3
Beam efficiency ^c [%]	55 ± 3	56 ± 3	55 ± 3	77 ± 2	Sect. 5.3
rms of the FWHM on the FOV [%]	6	6	6	3	Sect. 5.2.4
rms pointing error [arcsec]	< 3				Sect. 2.3.4
Absolute calibration uncertainty [%]	5				Sect. 6.3
rms calibration error [%]	5.5	6.0	5.7	3.0	Sect. 7.3
α noise integration in time ^c	0.5	0.5	0.5	0.5	Sect. 8.2.1
NEFD ^e [mJy \cdot s $^{1/2}$ /beam]	47 ± 4	38 ± 3	30 ± 3	9 ± 1	Sect. 8.2
NEFD ^f [mJy \cdot s $^{1/2}$ /beam]	57 ± 5	46 ± 4	36 ± 3	10 ± 1	
Mapping speed ^g [arcmin 2 /h/mJy 2]	45	70	111	1388	
Mapping speed ^h [arcmin 2 /h/mJy 2]	31	48	77	1119	

(a) Calculated from real array pixel size [2.75 mm / 2.0 mm] and unvignetted pupil diameter [27m]

(b) Full-width at half-maximum of the main beam using the combined results of the three methods

(c) Ratio between the main beam power and the total beam power up to a radius of 180 arcsec

(d) Effective power law of noise reduction with integration time

(e) NEFD extrapolated at zero opacity

(f) NEFD in typical IRAM good sky opacity condition: 2mm pwv, 60° elevation

(g) Mapping speed at zero opacity

(h) Mapping speed in typical IRAM good sky opacity condition: 2mm pwv, 60° elevation

Table 9.1: Summary of the main characteristics describing the measured performances of NIKA2.

The main characteristics, as defined in the MOU, are listed in Table 9.2, along with a reminder

of the *specifications* that are the requirements to be met by the instrument, and the *goals* that are the values targeted by the collaboration.

Table 9.2: Summary of the main characteristics describing the measured performances of NIKA2, as listed in MoU

			Array 1	Array 3	Array 1&3	Array 2
FOV diameter [arcmin]	Goal	6.5	6.5	6.5	6.5	6.5
	Specs	5	5	5	5	5
	Measure	6.6	6.6	6.6	6.6	6.6
Pixel size in beam sampling unit ^b [F λ]	Goal	0.6	0.6			0.6
	Specs	0.9	0.9			0.9
	Measure	1.09	1.09			0.93
Fraction of valid detectors [%]	Goal	90	90			90
	Specs	50	50			50
	Measure	84	84			90
NEFD ^a [mJy · s ^{1/2} /beam] goal on 90% of the KIDs					15	10
NEFD ^a [mJy · s ^{1/2} /beam] specification on 50% of the KIDs					30	20
Measured NEFD ^a on all valid KIDs [mJy · s ^{1/2} /beam]		57	46		36	10

^(a) NEFD in typical IRAM good sky opacity condition: 2mm pwv, 60° elevation

^(b) Calculated from real array pixel size [2.75 mm / 2.0 mm] and unvignetted pupil diameter [27m]

Appendix A

APPENDIX

A.1 Synchronization with the telescope

NIKA2 synchronization scheme NIKA2 reference clock is the *pulse per second* (pps) [TO BE DEVELOPED A BIT]

Synchronization between instrument and scan information A list of network specifications has been provided to IRAM by the NIKA2 consortium. A thorough characterization of the delay in receiving the telescope messages will be led by Francesco P.

Synchronization between instrument and telescope coordinates Albrecht S. to lead the characterization.

A final characterization of the accuracy of the dating of each sample will be undergone using zigzag scans acquired in excellent weather conditions.

A.2 Reference to technical documentation

This paragraph reviews the status of the technical documentation that should be delivered to the collaboration by the NIKA2 consortium and the IRAM, as defined in the MOU.

A.2.1 Consortium-lead documentation

- Plan of the cryostat: 3D model (e.g. STEP, Solid Works, etc.) and plans as built (e.g. PDF)
- List of hardware components (per module)
- Optics filtering components. [Consortium].
- Cryogenics system characteristics with basic and standard operating procedures (see section 6.3).
- Cryogenics monitoring and diagnostic tools plus procedure to contact a cryogenist from the consortium who is mandated to help IRAM in case of problem with the cryostat.
- Electronics cards characteristics, implantation plans, and operating procedures.
- Programmable electronics.

- Network needs (architecture, data rates, speed, memory, synchronization accuracy, internet access, storage, backup, archiving, etc).
- Software for instrument control and data acquisition (Camadria), aimed at general users.

A.2.2 IRAM-lead documentation

- Optics imaging system characteristics and calculations
- Observers interface: PaKo functions specific to NIKA2, plus useful scripts
- Automated on line data processing tools. [IRAM lead, consortium input].
- Off line data processing software. [IRAM lead, consortium input].
- Cook book (for external users: including a short description of NIKA2 setup, check list and procedure to use the instrument at the telescope). Can be provided at the end of instrument commissioning. [IRAM, consortium input].

A.3 Photometric system definitions

The definitions and the assumptions that have been used to derive the NIKA2 photometric system discussed in Sect. ?? are thoroughly reported here.

A.3.1 Response of a detector to astronomical source

Let us consider a source observed at airmass x under mm_{H_2O} of precipitable water, with specific intensity I_ν (in units of $\text{W}/\text{m}^2/\text{sr}/\text{Hz}$) in the direction θ, ϕ , where θ is the off-axis distance and ϕ the position angle, illuminating a KID of the NIKA2 array.

A KID response located at position θ, ϕ on the focal plane to this signal will be:

$$R(\theta, \phi, x, mm_{H_2O}) = G_k \int_0^{+\infty} I(\nu) \frac{T'(\nu)}{\left(\frac{\nu}{\nu_0}\right)^2} e^{-x\tau(\nu, mm_{H_2O})} A\Omega(\nu) d\nu \quad (\text{A.1})$$

where the different factors in the integral are:

- $\frac{T'(\nu)}{\left(\frac{\nu}{\nu_0}\right)^2}$: the system transmission. $T'(\nu)$ is the transmission as measured in section 2.1.2 with a Rayleigh-Jeans source. It is divided by $\left(\frac{\nu}{\nu_0}\right)^2$ to correct for the incident spectrum.
- $e^{-x\tau(\nu, mm_{H_2O})}$: the atmospheric transmission at airmass x for an amount of precipitable water vapor mm_{H_2O} generating an opacity $\tau(\nu)$.
- $A\Omega(\nu)$: the KID etendue, *i. e.* the product of its light collecting area by the solid angle it intercepts on the sky. While the step between pixels is well known and is measured (see Sect. ??), the actual solid angle is not known precisely and is *probably* a function of the frequency because the pixels sizes are close to the wavelength of operation (2.75 mm at 2 mm for example). The collecting A area is the projection of the IRAM primary on the cold pupil and is also not known very accurately.

The integral in eq A.1 gives the total power (units of W) falling on a KID. The factor G_k (units of W^{-1}) converts this power to Hertz.

By virtue of the conservation of specific intensity in a telescope, equation A.1 can be rewritten as:

$$R(\theta, \phi, x, mm_{H_2O}) = G_k A_p \Omega_s \int_0^{+\infty} I(\nu) \frac{T'(\nu)}{\left(\frac{\nu}{\nu_0}\right)^2} e^{(-x \cdot \tau(\nu, mm_{H_2O}))} \Omega_b(\theta, \phi, \nu) d\nu \quad (\text{A.2})$$

where:

- A_p is the area of the entrance pupil (*i.e.* the dish collecting area).
- Ω_s is the solid angle of the source seen from the entrance pupil.
- $\Omega_b(\theta, \phi, \nu)$ is the fraction of source signal illuminating the KID. It is thus normalized so that:

$$\int \int_{4\pi} \Omega_b(\theta, \phi, \nu) \sin \theta d\theta d\phi = 1 \quad (\text{A.3})$$

Equation A.2 describes the response of a KID, and is quite complex. We will in the following simplify it by making a few assumptions. Let us first turn ourselves toward the effect of the atmosphere.

A.3.2 Effect of the atmosphere

The effects of the atmosphere have been discussed in Sect. 2.1.2, in which we have defined an effective frequency ν_{eff} , as given in Eq. 2.1.

As seen in Fig. 2.2, typical variations of ν_{eff} with the spectral shape of the source range between 1% and 3%, and are relatively stable between good ($\tau_{225\text{GHz}} \simeq 0.1$) and poor ($\tau_{225\text{GHz}} \simeq 1.0$) atmospheric conditions for both the 1mm and 2mm bands. Let us now examine the effect of elevation. Under good atmospheric conditions ($\tau_{225\text{GHz}} \simeq 0.1$), ν_{eff} changes by less than 0.3% between zenith and 20 degree elevation. Under poor conditions ($\tau_{225\text{GHz}} \simeq 1.0$), this rises to almost 3% for a Rayleigh-Jeans spectrum in the 2 mm band, *i.e.* larger than the variations due to the spectral shape of the source.

Nevertheless, to a first approximation, we consider the shape of the atmospheric transmission independent of the elevation and water content, so that an effective zenith opacity τ_{eff} used. Equation A.2 becomes under this assumption:

$$R(\theta, \phi, x, mm_{H_2O}) \simeq G_k A_p \Omega_s e^{(-x \cdot \tau_{\text{eff}}(mm_{H_2O}))} \int_0^{+\infty} I(\nu) \frac{T'(\nu)}{\left(\frac{\nu}{\nu_0}\right)^2} T_{\text{atm}}(\nu) \Omega_b(\theta, \phi, \nu) d\nu \quad (\text{A.4})$$

where $T_{\text{atm}}(\nu)$ is the transmission of the atmosphere at zenith, and is a function of the frequency only. From the computations made to plot figure ??, we derive that this approximation is valid below the percent level for $\tau_{225\text{GHz}} < 0.35$

The dependance on elevation and opacity can be corrected as shown in Sect. 3, so that a response outside of atmosphere (in terms of airmass, but not in terms of transmission) can be derived:

$$R(\theta, \phi) \simeq G_k A_p \Omega_s \int_0^{+\infty} I(\nu) \frac{T'(\nu)}{\left(\frac{\nu}{\nu_0}\right)^2} T_{\text{atm}}(\nu) \Omega_b(\theta, \phi, \nu) d\nu \quad (\text{A.5})$$

Equation A.5 is the main photometric equation.

Because both A_p and Ω_b are not known with good accuracy, it is not possible to compute all the terms of eq. A.5 from first principles, and a practical way of calibrating the system must be used: it is done by observing a primary calibrator.

A.3.3 Beammap of a calibrator

A primary calibrator is a source whose spectral irradiance is known. For NIKA2, we use two planets as primary calibrators, Uranus and Neptune.

The specific intensity $I_c(\nu)$ of the calibrator is:

$$I_c(\nu) = \frac{S_c(\nu)}{\Omega_s} = \frac{S_c(\nu_0)}{\Omega_S} f\left(\frac{\nu}{\nu_0}\right) \quad (\text{A.6})$$

Where $S_c(\nu)$ is the spectral irradiance of the calibrator (units of $\text{W/m}^2/\text{Hz}$) or Jy. We parametrize the source spectral irradiance as a function of a reference frequency ν_0 that we choose arbitrarily to be: $\nu_0 = 150$ GHz for the 2mm array and $\nu_0 = 260$ GHz for both 1mm arrays.

Equation A.5 becomes:

$$R(\theta, \phi) \simeq G_k A_p S_c(\nu_0) \int_0^{+\infty} f\left(\frac{\nu}{\nu_0}\right) \frac{T'(\nu)}{\left(\frac{\nu}{\nu_0}\right)^2} T_{atm}(\nu) \Omega_b(\theta, \phi, \nu) d\nu \quad (\text{A.7})$$

Let further parametrize the beam as a function of the effective frequency as defined in eq ??, considering that its frequency dependency is only due to the diffraction law, hence a variation as $1/\nu$.

With this in hand, we can write the equation of a beammap using a single KID with eq A.4. At each position (θ, ϕ) on the beam map we have:

$$R_c(\theta, \phi) = G_k A_p S_c(\nu_0) \int_0^{+\infty} f\left(\frac{\nu}{\nu_0}\right) \Omega_b(\nu_0, \theta, \phi) \times \frac{\nu}{\nu_0} \frac{T'(\nu)}{\left(\frac{\nu}{\nu_0}\right)^2} T_{atm}(\nu) d\nu \quad (\text{A.8})$$

A.3.4 Calibration in FWHM_0 beam

This map is fitted with a gaussian of fixed width: FWHM_0 (we recall that $2\sqrt{2\ln 2}\sigma_0 = \text{FWHM}_0$).

$$R_c(\theta, \phi) = \frac{A_c}{2\pi\sigma_0^2} e^{-\frac{\theta^2}{2\sigma_0^2}} + \epsilon(\theta, \phi) \quad (\text{A.9})$$

where $\epsilon(\theta, \phi)$ are the residuals of the fit.

Assuming that the fit is not biased, we have:

$$\int \int R_c(\theta, \phi) \sin \theta d\theta d\phi = A_c \quad (\text{A.10})$$

because errors average out so that:

$$\int \int \epsilon(\theta, \phi) \sin \theta d\theta d\phi = 0 \quad (\text{A.11})$$

But we also know that integral of the beammap should give the power emitted by the source. Therefore, we form the map:

$$M_c(\theta, \phi) = R_c(\theta, \phi) S_c(\nu_0) / A_c \quad (\text{A.12})$$

where $S_c(\nu_0)$ is the spectral irradiance of the calibrator at a reference frequency ν_0 given in table 6.1. This map has units of $\text{W/m}^2/\text{Hz}$. Note that the choice of the reference frequency is arbitrary, it is a convention. By construction, integrating over the map we have:

$$\int \int M_c(\theta, \phi) \sin \theta d\theta d\phi = S_c(\nu_0) \quad (\text{A.13})$$

Similarly, a point source with spectral irradiance $S_s(\nu)$ will generate a response at position (θ, ϕ)

$$R_s(\theta, \phi) = G_k A_p \int_0^{+\infty} S_s(\nu) \Omega_b(\nu_0, \theta \times \frac{\nu}{\nu_0}, \phi) \frac{T'(\nu)}{\left(\frac{\nu}{\nu_0}\right)^2} T_{atm}(\nu) d\nu \quad (\text{A.14})$$

Note here that the effective frequency for the beam is not necessarily the same as the one for the primary calibrator, as it depends on the source spectrum.

This beammap will be fitted with a gaussian of fixed width:

$$R_s(\theta, \phi) = \frac{A_s}{2\pi\sigma_o^2} e^{-\frac{\theta^2}{2\sigma_o^2}} + \epsilon(\theta, \phi) \quad (\text{A.15})$$

The quoted flux for the source is then:

$$S_q(\nu_0) = S_c(\nu_0) \times \frac{A_s}{A_c} \quad (\text{A.16})$$

In other words, the quoted flux is the flux that should have the calibrator in order to generate a response that would be fitted with a gaussian of fixed width and the same amplitude as the source. Let us form the map:

$$M_s(\theta, \phi) = R_s(\theta, \phi) S_c(\nu_0) / A_c \quad (\text{A.17})$$

The map $M_{\theta, \phi}$ is said to be calibrated in Jy / FWHM₀ beam.

If we have a single point source in M, we have when we fit a gaussian of fixed width:

$$\int \int M_s(\theta, \phi) \sin \theta d\theta d\phi = A_s S_c(\nu_0) / A_c = S_q(\nu_0) \quad (\text{A.18})$$

Note that the quoted flux is not the flux of the source at the reference frequency. In order to find the flux of the source at the reference frequency, a color correction has to be applied

$$S_s(\nu_0) = S_q(\nu_0) C_s \quad (\text{A.19})$$

A.3.5 Color correction for point sources measured with fixed gaussian fit

When a source is measured

$$C_s = S_s(\nu_0) / S_q(\nu_0) = S_s(\nu_0) / S_c(\nu_0) \times \frac{A_c}{A_s} \quad (\text{A.20})$$

$$C_s = S_s(\nu_0) / S_c(\nu_0) \times \frac{\int \int R_c(\theta, \phi) \sin \theta d\theta d\phi}{\int \int R_s(\theta, \phi) \sin \theta d\theta d\phi} \quad (\text{A.21})$$

$$C_s = S_s(\nu_0) / S_c(\nu_0) \times \frac{\int \int G_k A_p S_c(\nu_0) \int_0^{+\infty} f\left(\frac{\nu}{\nu_0}\right) \Omega_b(\nu_0, \theta \times \frac{\nu}{\nu_0}, \phi) \frac{T'(\nu)}{\left(\frac{\nu}{\nu_0}\right)^2} T_{atm}(\nu) d\nu \sin \theta d\theta d\phi}{\int \int G_k A_p \int_0^{+\infty} S_s(\nu) \Omega_b(\nu_0, \theta \times \frac{\nu}{\nu_0}, \phi) \frac{T'(\nu)}{\left(\frac{\nu}{\nu_0}\right)^2} T_{atm}(\nu) d\nu \sin \theta d\theta d\phi} \quad (\text{A.22})$$

which simplifies into:

$$C_s = S_s(\nu_0) \times \frac{\int_0^{+\infty} f\left(\frac{\nu}{\nu_0}\right) \int \int \Omega_b(\nu_0, \theta \times \frac{\nu}{\nu_0}, \phi) \sin \theta d\theta d\phi \frac{T'(\nu)}{\left(\frac{\nu}{\nu_0}\right)^2} T_{atm}(\nu) d\nu}{\int_0^{+\infty} S_s(\nu) \int \int \Omega_b(\nu_0, \theta \times \frac{\nu}{\nu_0}, \phi) \sin \theta d\theta d\phi \frac{T'(\nu)}{\left(\frac{\nu}{\nu_0}\right)^2} T_{atm}(\nu) d\nu} \quad (\text{A.23})$$

We have:

$$\int \int \Omega_b(\nu_0, \theta \times \frac{\nu}{\nu_0}, \phi) \sin \theta d\theta d\phi = 1 \quad (\text{A.24})$$

So that:

$$C_s = S_s(\nu_0) \times \frac{\int_0^{+\infty} f\left(\frac{\nu}{\nu_0}\right) \frac{T'(\nu)}{\left(\frac{\nu}{\nu_0}\right)^2} T_{atm}(\nu) d\nu}{\int_0^{+\infty} S_s(\nu) \frac{T'(\nu)}{\left(\frac{\nu}{\nu_0}\right)^2} T_{atm}(\nu) d\nu} \quad (\text{A.25})$$

A.3.6 Photometric correction

The effect of the telescope-driven beam size variations, as discussed in Sect. 6.5, is mitigated by correcting the measured flux densities using a beam-size dependent function, referred to as the photometric correction.

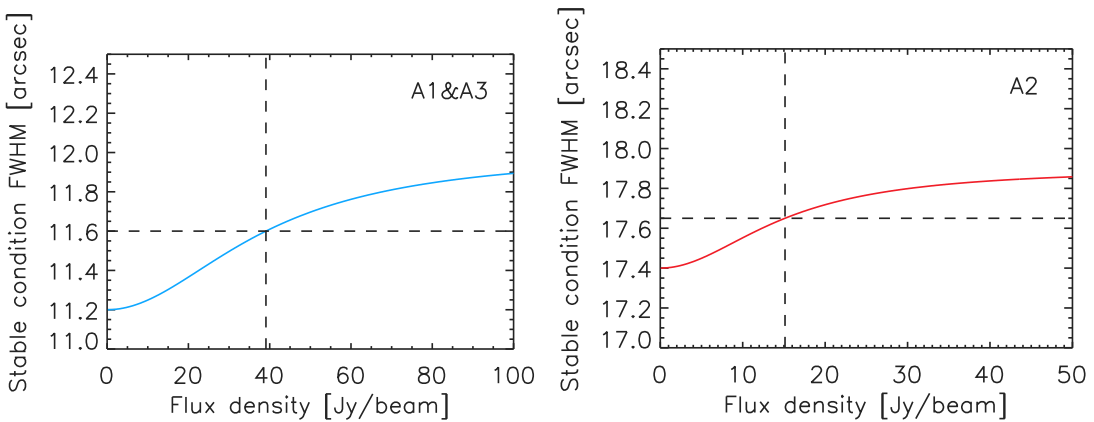


Figure A.1: Flux-dependency of the photometric correction pivot Gaussian size σ_* . This is measured as the 2D Gaussian fit of the map observed in stable conditions

In our reference photometric system, as presented in Sect. 6.2.2 and Sect. A.3.4, the flux density is estimated by fitting an amplitude of a fixed-width Gaussian beam:

$$\hat{S} = 2 \int \int M(\theta, \phi) e^{-\frac{\theta^2}{2\sigma_0^2}} \sin \theta d\theta d\phi. \quad (\text{A.26})$$

The beam width σ_0 corresponds to the reference FWHM, which we recall, is $12.5''$ for the 1mm arrays and $18.5''$ for the 2mm array, as defined in Table 6.1.

First of all, in stable observing conditions (no beam broadening effect), the map can be modeled by a single Gaussian of width σ_* corresponding basically to the main beam size:

$$M(\theta, \phi) = \frac{A}{2\pi\sigma_*^2} e^{-\frac{\theta^2}{2\sigma_*^2}}. \quad (\text{A.27})$$

Ingesting Eq. A.29 in Eq. A.26, we find that the flux density estimator depends on the beam size as

$$\hat{S} = A \frac{2\sigma_0^2}{(\sigma_*^2 + \sigma_0^2)}. \quad (\text{A.28})$$

However, the map is calibrated in $FWHM_0$ beam, as described in Sect. 6.2.2. The absolute calibration factor, which is evaluating as $S_c(\nu_0)/\hat{S}_c$, has a beam dependency that compensates the one of the flux density for the source.

On the other hand, if the beam size varies so that the Gaussian part has a size given by σ' , the map model rewrites

$$M(\theta, \phi) = \frac{A}{2\pi\sigma'^2} e^{-\frac{\theta^2}{2\sigma'^2}}, \quad (\text{A.29})$$

where the amplitude is the same as in the stable condition case because the flux density is conserved when integrating over the map. The flux density measured using the fixed-width amplitude estimator

$$\hat{S}' = A \frac{2\sigma_0^2}{(\sigma'^2 + \sigma_0^2)} \quad (\text{A.30})$$

presents a beam-dependency which differs from the one of the primary calibrator, and which is no longer compensated when performing the absolute calibration.

To retrieve an unbiased flux density estimate \hat{S}_{pc} , the flux density estimate \hat{S}' has to be corrected as

$$\hat{S}_{pc} = f(\sigma') \hat{S}', \quad (\text{A.31})$$

where the photometric correction is

$$f(\sigma') = \frac{(\sigma'^2 + \sigma_0^2)}{(\sigma_*^2 + \sigma_0^2)}, \quad (\text{A.32})$$

so that $f(\sigma') = 1$ if $\sigma' = \sigma_*$.

The pivot Gaussian size σ_* corresponds to the nominal size of the 2D Gaussian fit of the beam that is measured in stable observing conditions. We find it slightly varies with the source flux density. Whereas it basically corresponds to the main beam size for faint to moderately bright point source, it is slightly larger for sources bright enough for the error beams to be well above the noise level. In Fig. A.1, we give an empirical model for the flux dependency of σ_* : it smoothly goes from $11.2''$ at 1-mm and $17.4''$ at 2-mm for moderately bright sources to $11.6''$ at 1-mm and $17.65''$ at 2-mm at the flux density of Uranus, then slightly continues increasing for sources brighter than Uranus.

A.4 Focus surface stability checks

We test the stability of the NIKA2 focus surfaces, as obtained in Sect. 4.3, against observation dates and atmospheric conditions. We compare the focus surface obtained from the five individual focus sequences used in Sect. 4.3.

In Figs. A.2-A.3, we compare the defocus along two perpendicular diameters across the FOV. Although any direction would have been equivalent for this test, we choose to position the diameters along-with and perpendicular-to the KID geometrical grid to avoid the scatter due to KID non-alignment in any other direction. The scatter is further mitigated by considering four-detector-wide diameters as shown in upper the left corner of Figs. A.2-A.3.

The individual focus surfaces are in agreement with each other within statistical errors. No systematics are observed depending on the observation dates nor the atmospheric conditions. This indicates the robustness of the focus surface estimates reported in Sect. ??.

Draft

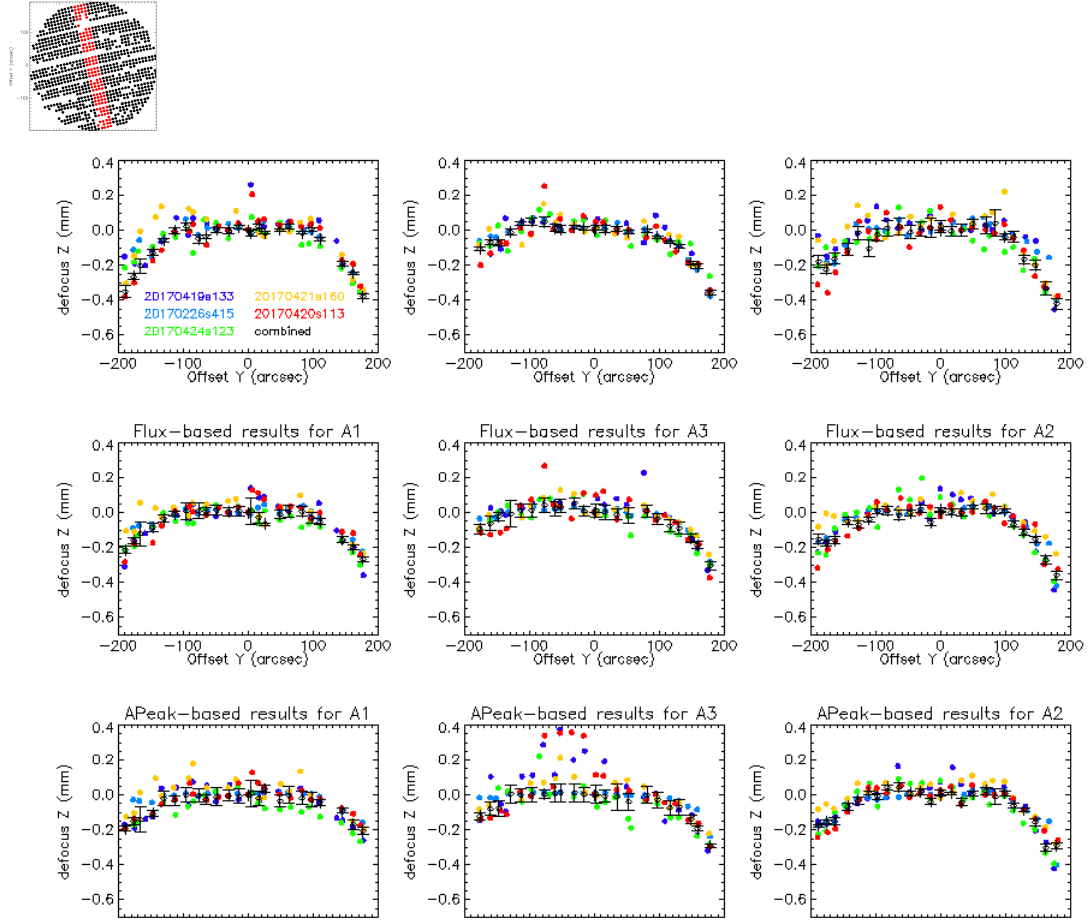


Figure A.2: This series of plot show the relative focus with respect to the center (defocus) along the ‘vertical diameter’, that is a band of four-detector width across the FOV, which is vertical with respect to the detector geometrical grid, as illustrated by the plot in the upper left corner. The datapoints show the defocus along the ‘vertical diameter’ estimated from the five focus sequences, namely 20170226s415–419 (sky blue), 20170419s133–137 (dark blue), 20170420s113–117 (red), 20170421s160–164 (yellow) and 20170424s123–127 (green), using the $z^{(a)}|_{\text{fwhm}}$, $z^{(a)}|_{\text{flux}}$ and $z^{(a)}|_{\text{peak}}$ estimators from top to bottom, and for A1, A3 and A2 arrays from left to right. The black datapoints are the five-sequence combined defocus, as presented in Fig. 4.3, taken along the ‘vertical diameter’, and the errorbars, the five-sequence combined defocus errors along the ‘vertical diameter’.

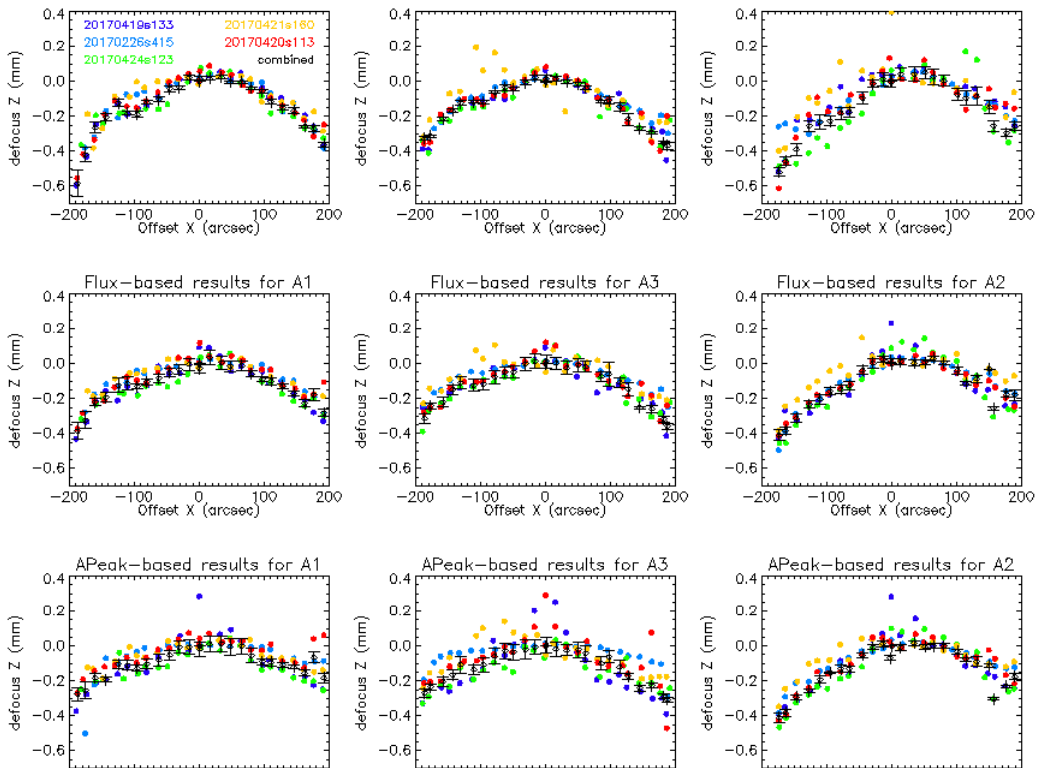


Figure A.3: Same legend as in Fig. A.2, but for the detectors located in an ‘horizontal diameter’, i.e. a band of four-detector width across the FOV, which is horizontal with respect to the detector geometrical grid, as illustrated by the plot in the upper left corner.

A.5 Calibration reference software

The reference software used for NIKA2 calibration are available under SVN in the directory Processing/Scr/Reference/, referred to as the calibration directory. Once a first beam map scan is reduced, the subsequent steps of the calibration are implemented using the main script in the calibration directory:

`Calibration/baseline_calibration.pro.`

This script, which must be edited to perform the calibration of each campaign, calls the following daughter scripts:

FOV geometry and relative calibration

In the calibration directory:

`Geometry/reduce_beammap.pro`

Opacity

In the Calibration directory:

`Opacity/reduce_skydips_reference.pro.`

This reference script calls the routine `all_skydips.pro`, which relies on the fitting routine available in:

`Processing/Realtime/nk_test_allskd4.pro`

Absolute calibration

In the calibration directory:

`Photometry/calibration_uranus_reference.pro.`

The photometric correction is implemented in:

`Photometry/photometric_correction.pro`

Photometric checks

Once all these steps are done, the calibration can be checked using the script:

`Photometry/validate_calibration_reference.pro.`

Bibliography

- [1] R. Adam *et al.*, arXiv:1707.00908
- [2] Petit J., Bardeau S., Reynier E., "Comparison of ATM versions: Impact on the calibration of IRAM instruments", IRAM memo 2009-5, <http://www.iram-institute.org/EN/content-page-161-7-66-161-0-0.html>
- [3] Combes, F., Rex, M., Rawle, T. D., et al, 2012, A&A, Vol. 538, L4
- [4] Pardo, J. R., Cernicharo, J. & Serabyn, E., 2002, IEEE Transactions on Antennas and Propagation 49, 1683
- [5] Dempsey *et al.* 2013
- [6] Knapp *et al.* 1994
- [7] Tafoya *et al.* 2004
- [8] <http://www.lesia.obspm.fr/perso/emmanuel-lellouch/mars/index.php>
- [9] https://github.com/haussel/photometry/blob/master/notebooks/planet_fluxes.ipynb
- [10] (Planck intermediate results LII, Planck Collaboration in press)
- [11] <https://github.com/haussel/photometry>.
- [12] <https://ssd.jpl.nasa.gov/horizons.cgi>
- [13] <https://www.cosmos.esa.int/web/herschel/calibrator-models>
- [14] M. Krips, talk at the 8th IRAM Millimeter Interferometry School, Grenoble (France), October 2012, and private communication.
<http://www.iram.fr/IRAMFR/IS/IS2012/presentations/krips-fluxcalibration.pdf>
- [15] Gordon, M. A., Astrophysical Journal, vol. 421, no. 1, p. 314-317
- [16] M.G. Hoare, et al., 1992, MNRAS, 258, 257
- [17] Durand's PhD Thesis at Université Grenoble Alpes, 2008
- [18] M. Calvo *et al.*, Journal of Low Temperature Physics 184 (2016) 816-823
- [19] A. Monfardini *et al.*, The Astrophysical Journal Supplement 194 (2011) 24
- [20] O. Bourrion *et al.*, JINST 11 (2016) P11001
- [21] M. Calvo *et al.*, Astron. Astrophys. 551 (2013) L12
- [22] A. Monfardini *et al.*, JLTP 176 (2014) 787
- [23] A. Catalano *et al.*, Astron. Astrophys. 569 (2014) A9.

Draft

- [24] Combes F. et al., A&A 538, 4, 2012
- [25] A. Ritacco *et al.*, Astron. Astrophys. **599** (2017) A34
- [26] A. Bracco *et al.*, Astron. Astrophys. **604** (2017) A52
- [27] R. Adam *et al.*, Astron. Astrophys. **569** (2014) A66
- [28] R. Adam *et al.*, Astron. Astrophys. **576** (2015) A12
- [29] R. Adam *et al.*, Astron. Astrophys. **586** (2016) A122
- [30] R. Adam *et al.*, Astron. Astrophys. **598** (2017) A115
- [31] F. Ruppin *et al.*, Astron. Astrophys. **597** (2017) A110
- [32] R. Adam *et al.*, arXiv:1706.10230 [astro-ph.CO].
- [33] C. Romero *et al.*, arXiv:1707.06113 [astro-ph.CO].
- [34] B. Comis *et al.*, arXiv:1605.09549 [astro-ph.CO].